

26 **Abstract**

27 Nitrogen oxides ($\text{NO}_x = \text{NO} + \text{NO}_2$) play a crucial role in the formation of ozone and secondary inorganic and
28 organic aerosols, thus affecting human health, global radiation budget, and climate. The diurnal and spatial
29 variations of NO_2 are functions of emissions, advection, deposition, vertical mixing, and chemistry. Their
30 observations, therefore, provide useful constraints in our understanding of these factors. We employ a Regional
31 chemical and transport model (REAM) to analyze the observed temporal (diurnal cycles) and spatial
32 distributions of NO_2 concentrations and tropospheric vertical column densities (TVCDs) using aircraft in situ
33 measurements, surface EPA Air Quality System (AQS) observations, as well as the measurements of TVCDs by
34 satellite instruments (OMI: the Ozone Monitoring Instrument; and GOME-2A: Global Ozone Monitoring
35 Experiment – 2A), ground-based Pandora, and the Airborne Compact Atmospheric Mapper (ACAM) instrument,
36 in July 2011 during the DISCOVER-AQ campaign over the Baltimore-Washington region. The model
37 simulations at 36- and 4-km resolutions are in reasonably good agreement with the regional mean temporospatial
38 NO_2 observations in the daytime. However, nighttime mixing in the model needs to be enhanced to reproduce the
39 observed NO_2 diurnal cycle in the model. Another discrepancy is that Pandora measured NO_2 TVCDs show much
40 less variation in the late afternoon than simulated in the model. The higher resolution 4-km~~Relative to the 36-km~~
41 ~~model~~ simulations tend to, the 4 km model results show larger biases compared to the observations due largely to
42 the larger spatial variations of NO_2/NO_x emissions in the model when the model spatial resolution is increased
43 from 36 to 4 km,~~although the biases are often comparable to the ranges of the observations.~~ OMI, GOME-2A,
44 and ~~t~~The high-resolution aircraft ACAM observations show a more dispersed distribution of NO_2 vertical column
45 densities (VCDs) and lower VCDs in urban regions than corresponding 36- and 4-km model simulations,
46 reflecting likely the spatial distribution bias of NO_x emissions in the National Emissions Inventory (NEI) 2011-~~at~~
47 high resolution.

48 **1 Introduction**

49 Nitrogen oxides ($\text{NO}_x = \text{NO} + \text{NO}_2$) are among the most important trace gases in the atmosphere due to their
50 crucial role in the formation of ozone (O_3), secondary aerosols, and their role in the chemical transformation of
51 other atmospheric species, such as carbon monoxide (CO) and volatile organic compounds (VOCs) (Cheng et al.,
52 2017; Cheng et al., 2018; Fisher et al., 2016; Li et al., 2019; Liu et al., 2012; Ng et al., 2017; Peng et al., 2016;
53 Zhang and Wang, 2016). NO_x is emitted by both anthropogenic activities and natural sources. Anthropogenic
54 sources account for about 77% of the global NO_x emissions, and fossil fuel combustion and industrial processes
55 are the primary anthropogenic sources, which contribute to about 75% of the anthropogenic emissions (Seinfeld
56 and Pandis, 2016). Other important anthropogenic sources include agriculture and biomass and biofuel burning.
57 Soils and lightning are two major natural sources. Most NO_x is emitted as NO , which is then oxidized to NO_2 by
58 oxidants, such as O_3 , the hydroperoxyl radical (HO_2), and organic peroxy radicals (RO_2).

59 The diurnal variations of NO_2 controlled by physical and chemical processes reflect the temporal patterns of
60 these underlying controlling factors, such as NO_x emissions, chemistry, deposition, advection, diffusion, and
61 convection. Therefore, the observations of NO_2 diurnal cycles can be used to evaluate our understanding of NO_x
62 related emission, chemistry, and physical processes (Frey et al., 2013; Jones et al., 2000; Judd et al., 2018). For
63 example, Brown et al. (2004) analyzed the diurnal patterns of surface NO , NO_2 , NO_3 , N_2O_5 , HNO_3 , OH , and O_3
64 concentrations along the East Coast of the United States (U.S.) during the New England Air Quality Study
65 (NEAQS) campaign in the summer of 2002 and found that the predominant nighttime sink of NO_x through the
66 hydrolysis of N_2O_5 had an efficiency on par with daytime photochemical loss over the ocean surface off the New
67 England coast. Van Stratum et al. (2012) investigated the contribution of boundary layer dynamics to chemistry
68 evolution during the DOMINO (Diel Oxidant Mechanisms in relation to Nitrogen Oxides) campaign in 2008 in
69 Spain and found that entrainment and boundary layer growth in daytime influenced mixed-layer NO and NO_2

70 diurnal cycles on the same order of chemical transformations. David and Nair (2011) found that the diurnal
71 patterns of surface NO, NO₂, and O₃ concentrations at a tropical coastal station in India from November 2007 to
72 May 2009 were closely associated with sea breeze and land breeze which affected the availability of NO_x through
73 transport. They also thought that monsoon-associated synoptic wind patterns could strongly influence the
74 magnitudes of NO, NO₂, and O₃ diurnal cycles. The monsoon effect on surface NO, NO₂, and O₃ diurnal cycles
75 was also observed in China by Tu et al. (2007) on the basis of continuous measurements of NO, NO₂, and O₃ at
76 an urban site in Nanjing from January 2000 – February 2003.

77 In addition to surface NO₂ diurnal cycles, the daily variations of NO₂ vertical column densities (VCDs) were
78 also investigated in previous studies. For example, Boersma et al. (2008) compared NO₂ tropospheric VCDs
79 (TVCDs) retrieved from OMI (the Ozone Monitoring Instrument) and SCIAMACHY (SCanning Imaging
80 Absorption SpectroMeter for Atmospheric CHartography) in August 2006 around the world. They found that the
81 diurnal patterns of different types of NO_x emissions could strongly affect the NO₂ TVCD variations between
82 OMI and SCIAMACHY and that intense afternoon fire activity resulted in an increase of NO₂ TVCDs from
83 10:00 LT (local time) to 13:30 LT over tropical biomass burning regions. Boersma et al. (2009) further
84 investigated the NO₂ TVCD change from SCIAMACHY to OMI in different seasons of 2006 in Israeli cities and
85 found that there was a slight increase of NO₂ TVCDs from SCIAMACHY to OMI in winter due to increased NO_x
86 emissions from 10:00 LT to 13:30 LT and a sufficiently weak photochemical sink and that the TVCDs from OMI
87 were lower than SCIAMACHY in summer due to a strong photochemical sink of NO_x.

88 All these above researches, however, exploited only NO₂ surface or satellite VCD measurements. Due to the
89 availability of ground-based NO₂ VCD observations, some recent studies tried to investigate the diurnal
90 relationships between NO₂ surface concentrations and NO₂ VCDs (Kollonige et al., 2018; Thompson et al.,
91 2019). For example, Zhao et al. (2019) converted Pandora direct-sun and zenith-sky NO₂ VCDs to NO₂ surface

92 concentrations using concentration-to-partial-column ratios and found that the derived concentrations well
93 captured the observed NO₂ surface diurnal and seasonal variations. Knepp et al. (2015) related the daytime
94 variations of NO₂ TVCD measurements by ground-based Pandora instruments to the variations of coincident NO₂
95 surface concentrations using a planetary boundary layer height (PBLH) factor over the periods July 2011 –
96 October 2011 at the NASA Langley Research Center in Hampton, Virginia and July 2011 at Padonia and
97 Edgewood sites in Maryland for the DISCOVER-AQ experiment, showing the importance of boundary-layer
98 vertical mixing on NO₂ vertical distributions and the ability of NO₂ VCD measurements to infer hourly
99 boundary-layer NO₂ variations. DISCOVER-AQ, the Deriving Information on Surface conditions from Column
100 and Vertically Resolved Observations Relevant to Air Quality experiment (<https://discover-aq.larc.nasa.gov/>, last
101 access: April 6, 2019), was designed to better understand the relationship between boundary-layer pollutants and
102 satellite observations (Flynn et al., 2014; Reed et al., 2015). Figure S1 shows the sampling locations of the
103 summer DISCOVER-AQ 2011 campaign in the Baltimore-Washington metropolitan region. In this campaign, the
104 NASA P-3B aircraft flew spirals over six air quality monitoring sites (Aldino - rural/suburban, Edgewood -
105 coastal/urban, Beltsville - suburban, Essex - coastal/urban, Fairhill - rural, and Padonia - suburban) (Table S1)
106 and the Chesapeake Bay (Cheng et al., 2017; Lamsal et al., 2014), and measured 2454 NO₂ profiles in 14 flight
107 days in July (Zhang et al., 2016). During the same period, the NASA UC-12 aircraft flew across the Baltimore-
108 Washington region at an altitude about 8 km above sea level (ASL), using the Airborne Compact Atmospheric
109 Mapper (ACAM) to map the distributions of NO₂ VCDs below the aircraft (Lamsal et al., 2017). Furthermore,
110 ground-based instruments were deployed to measure NO₂ surface concentrations, NO₂ VCDs, and other physical
111 properties of the atmosphere (Anderson et al., 2014; Reed et al., 2015; Sawamura et al., 2014). Satellite OMI and
112 GOME-2A (Global Ozone Monitoring Experiment – 2A) instruments provided NO₂ TVCD measurements over
113 the campaign region at 13:30 and 9:30 LT, respectively. These concurrent measurements of NO₂ VCDs, surface
114 NO₂, and vertically resolved distributions of NO₂ during the DISCOVER-AQ 2011 campaign, therefore, provide

115 a comprehensive dataset to evaluate NO₂ diurnal and spatial variabilities and processes affecting NO₂
116 concentrations.

117 Section 2 describes the measurement datasets in detail. The Regional chEmistry and trAnsport Model
118 (REAM), also described in section 2, is applied to simulate the NO₂ observations during the DISCOVER-AQ
119 campaign in July 2011. The evaluations of the simulated diurnal cycles of surface NO₂ concentrations, NO₂
120 vertical profiles, and NO₂ TVCDs are discussed in section 3 through comparisons with observations. In section 3,
121 we also investigate the differences between NO₂ diurnal cycles on weekdays and weekends and their implications
122 for NO_x emission characteristics. To corroborate our evaluation of NO_x emissions based on NO₂ diurnal cycles,
123 we further compare observed NO_y (reactive nitrogen compounds) concentrations with REAM simulation results
124 in section 3. Moreover, we assess the resolution dependence of REAM simulation results in light of the
125 observations and discuss the potential distribution biases of NO_x emissions ~~at high resolution~~ by comparing the
126 36- and 4-km REAM simulation results with OMI, GOME-2A, and high-resolution ACAM NO₂ VCDs. Finally,
127 we summarize the study in section 4.

128 **2 Datasets and model description**

129 2.1 REAM

130 REAM has been widely applied in many studies (Cheng et al., 2017; Choi et al., 2008; Li et al., 2019; Zhang
131 et al., 2018; Zhang et al., 2016; Zhao et al., 2009). The model has a horizontal resolution of 36 km and 30 vertical
132 layers in the troposphere. Meteorology fields are from a Weather Research and Forecasting (WRF, version 3.6)
133 model simulation with a horizontal resolution of 36 km. We summarize the physics parameterization schemes of
134 the WRF simulation in Table S2. The WRF simulation is initialized and constrained by the NCEP coupled
135 forecast system model version 2 (CFSv2) products (<http://rda.ucar.edu/datasets/ds094.0/>, last access: March 10,

136 [2015](#)) (Saha et al., 2011). The chemistry mechanism in REAM is based on GEOS-Chem v11.01 with updated
137 aerosol uptake of isoprene nitrates (Fisher et al., 2016) and revised treatment of wet scavenging processes (Luo et
138 al., 2019). A $2^\circ \times 2.5^\circ$ GEOS-Chem simulation provides the chemical boundary and initial conditions.

139 Biogenic VOC emissions in REAM are from MEGAN v2.10 (Guenther et al., 2012). Anthropogenic
140 emissions on weekdays are from the National Emission Inventory 2011 (NEI2011) (EPA, 2014) from the Pacific
141 Northwest National Laboratory (PNNL), which has an initial resolution of 4 km and is re-gridded to REAM 36-
142 km grid cells (Figure [S2](#)). Weekday emission diurnal profiles are from NEI2011. The weekday to weekend
143 emission ratios and weekend emission diurnal profiles are based on previous studies (Beirle et al., 2003; Boersma
144 et al., 2009; Choi et al., 2012; de Foy, 2018; DenBleyker et al., 2012; Herman et al., 2009; Judd et al., 2018;
145 Kaynak et al., 2009; Kim et al., 2016). These studies suggested that weekend NO_x emissions were 20% - 50%
146 lower than weekday emissions, and the weekend NO_x emission diurnal cycles were different from weekdays;
147 therefore, we specify a weekend to weekday NO_x emission ratio of 2/3 in this study. The resulting diurnal
148 variations of weekday and weekend NO_x emissions over the DISCOVER-AQ 2011 region are shown in Figure
149 [43](#). The diurnal emission variation is lower on weekends than on weekdays.

150 To understand the effects of model resolutions on the temporospatial distributions of NO_2 , we also conduct a
151 REAM simulation with a horizontal resolution of 4 km during the DISCOVER-AQ campaign. A 36-km REAM
152 simulation (discussed in section [3.42](#)) provides the chemical initial and hourly boundary conditions. Meteorology
153 fields are from a nested WRF simulation (36 km, 12 km, 4 km) with cumulus parameterization turned off in the
154 4-km domain (Table S2). Figure [S1](#) shows a comparison of the 4-km and 36-km REAM grid cells with
155 DISCOVER-AQ observations, and Figure [S2](#) shows a comparison of NO_x emission distributions between the 4-
156 km and 36-km REAM simulations. The comparison of NO_x emission diurnal variations over the DISCOVER-AQ
157 2011 region between the 4-km and 36-km REAM is shown in Figure [43](#).

158 We evaluate the performances of the 36-km and nested 4-km WRF simulations by comparing temperature
159 and wind from the P-3B spirals (Figure S1) and precipitation from the NCEP (National Centers for
160 Environmental Prediction) Stage IV precipitation dataset with those coincident WRF simulation results in July
161 2011. Generally, P-3B spirals range from ~400 m to ~3.63 km in height above the ground level (AGL). As shown
162 in Figure S3, both the 36-km and nested 4-km WRF simulations predict temperature well with $R^2 = 0.94$ and $R^2 =$
163 0.98 , respectively. Both WRF simulations show good agreement with P-3B measurements in U-wind (36-km: $R^2 =$
164 0.62 ; 4-km: $R^2 = 0.71$), V-wind (36-km: $R^2 = 0.75$; 4-km: $R^2 = 0.74$), wind speed (36-km: $R^2 = 0.52$; 4-km: $R^2 =$
165 0.64), and wind direction (36-km: $R^2 = 0.40$; 4-km: $R^2 = 0.50$) (Figures S3 and S4). The evaluations above
166 suggest that WRF-simulated wind fields are good and comparable at 4-km and 36-km resolutions; they are not the
167 reasons for the differences of the 4-km and 36-km simulations of trace gases by REAM, which is driven by WRF
168 meteorological fields.

169 The NCEP Stage IV precipitation dataset provides hourly precipitation across the contiguous United States
170 (CONUS) with a resolution of ~4 km based on the merging of rain-gauge data and radar observations (Lin and
171 Mitchell, 2005; Nelson et al., 2016). The Stage IV dataset is useful for evaluating model simulations, satellite
172 precipitation estimates, and radar precipitation estimates (Davis et al., 2006; Gourley et al., 2011; Kalinga and
173 Gan, 2010; Lopez, 2011; Yuan et al., 2008). We obtain the Stage IV precipitation data in July 2011 from the
174 NCAR/UCAR Research Data Archive (<https://rda.ucar.edu/datasets/ds507.5/>). As shown in Figures S5 and S6,
175 generally, both the 36-km and nested 4-km WRF simulations predict much less precipitation (in precipitation
176 amount and duration) compared to Stage IV in July 2011 around the DISCOVER-AQ campaign region,
177 especially for the nested 4-km WRF simulation. We find that large-scale precipitation amounts are much less
178 compared to convective precipitation in most regions in the 36-km WRF simulation (Figure S7) during the
179 simulation period, which is contradictory to Li et al. (2020) showing non-convective precipitation accounting for
180 25%–40% of the total precipitation. At 4-km resolution, convective and non-convective precipitations are not

181 ~~separated because convection is explicitly resolved. The model low bias is large (Figure S6). The underestimation~~
182 ~~of precipitation in our WRF simulations may lead to high biases of soluble species in REAM, such as HNO₃, due~~
183 ~~to underestimated wet scavenging.~~

184 2.2 NO₂ TVCD measurements by OMI and GOME-2A

185 The OMI instrument onboard the sun-synchronous NASA EOS Aura satellite with an equator-crossing time
186 of around 13:30 LT was developed by the Finnish Meteorological Institute and the Netherlands Agency for
187 Aerospace Programs to measure solar backscattering radiation in the visible and ultraviolet bands (Levelt et al.,
188 2006; Russell et al., 2012). The radiance measurements are used to derive trace gas concentrations in the
189 atmosphere, such as O₃, NO₂, HCHO, and SO₂ (Levelt et al., 2006). OMI has a nadir resolution of 13 km × 24 km
190 and provides daily global coverage (Levelt et al., 2006).

191 Two widely-used archives of OMI NO₂ VCD products are available, NASA OMNO2 (v4.0)
192 (https://disc.gsfc.nasa.gov/datasets/OMNO2_003/summary, last access: September 26, 2020) and KNMI
193 DOMINO (v2.0) (<http://www.temis.nl/airpollution/no2.html>, last access: January 14, 2015). Although both use
194 Differential Optical Absorption Spectroscopy (DOAS) algorithms to derive NO₂ slant column densities, they
195 have differences in spectral fitting, stratospheric and tropospheric NO₂ slant column density (SCD) separation, a
196 priori NO₂ vertical profiles, and air mass factor (AMF) calculation, etc. (Boersma et al., 2011; Bucselá et al.,
197 2013; Chance, 2002; Krotkov et al., 2017; Lamsal et al., 2020; Marchenko et al., 2015; Oetjen et al., 2013; van
198 der A et al., 2010; Van Geffen et al., 2015). Both OMNO2 and DOMINO have been extensively evaluated with
199 field measurements and models (Boersma et al., 2009; Boersma et al., 2011; Choi et al., 2020; Hains et al., 2010;
200 Huijnen et al., 2010; Ionov et al., 2008; Irie et al., 2008; Lamsal et al., 2014; Lamsal et al., 2020; Oetjen et al.,
201 2013). The estimated uncertainty of DOMINO TVCD product ~~includes an absolute component of~~ 1.0×10^{15}
202 molecules cm⁻² ~~and a relative AMF component of~~ +25% (Boersma et al., 2011), while the uncertainty of OMNO2

203 TVCD product ranges from ~30% under clear-sky conditions to ~60% under cloudy conditions (Lamsal et al.,
204 2014; Oetjen et al., 2013; Tong et al., 2015). In order to reduce uncertainties in this study, we only use TVCD
205 data with effective cloud fractions < 0.2 , solar zenith angle (SZA) $< 80^\circ$, and albedo ≤ 0.3 . Both positive and
206 negative TVCDs are considered in the calculation. The data affected by row anomaly are excluded (Boersma et
207 al., 2018; Zhang et al., 2018).

208 For AMF calculation, DOMINO used daily TM4 model results with a resolution of $3^\circ \times 2^\circ$ as a priori NO_2
209 vertical profiles (Boersma et al., 2007; Boersma et al., 2011), while OMNO2 v4.0 used monthly mean values
210 from the Global Modeling Initiative (GMI) model with a resolution of $1^\circ \times 1.25^\circ$. The relatively coarse horizontal
211 resolution of the a priori NO_2 profiles in the retrievals can introduce uncertainties in the spatial and temporal
212 characteristics of NO_2 TVCDs at satellite pixel scales. For comparison purposes, we also use 36-km REAM
213 simulation results as the a priori NO_2 profiles to compute the AMFs and NO_2 TVCDs with the DOMINO
214 algorithm. The 36-km REAM NO_2 data are first regridded to OMI pixels to calculate the corresponding
215 tropospheric AMFs, which are then applied to compute OMI NO_2 TVCDs by dividing the tropospheric SCDs
216 from the DOMINO product by our updated AMFs.

217 The GOME-2 instrument onboard the polar-orbiting MetOp-A satellite (now referred to as GOME-2A) is an
218 improved version of GOME-1 launched in 1995 and has an overpass time of 9:30 LT and a spatial resolution of
219 $80 \times 40 \text{ km}^2$ (Munro et al., 2006; Peters et al., 2012). GOME-2A measures backscattered solar radiation in the
220 range from 240 nm to 790 nm, which is used for VCD retrievals of trace gases, such as O_3 , NO_2 , BrO, and SO_2
221 (Munro et al., 2006). We use the KNMI TM4NO2A v2.3 GOME-2A NO_2 VCD product archived on
222 http://www.temis.nl/airpollution/no2col/no2colgome2_v2.php (last access: January 22, 2015) (Boersma et al.,
223 2007; Boersma et al., 2011). GOME-2A derived NO_2 VCDs have been validated with SCIAMACHY and MAX-
224 DOAS measurements (Irie et al., 2012; Peters et al., 2012; Richter et al., 2011). As in the case of OMI, we use the

225 ~~same criteria to filter the NO₂ TVCD data~~ also and recalculate the tropospheric AMF values and GOME-2A
226 TVCDs using the daily 36-km REAM NO₂ profiles (9:00 LT – 10:00 LT).

227 2.3 Pandora ground-based NO₂ VCD measurements

228 Pandora is a small direct sun spectrometer, which measures sun and sky radiance from 270 to 530 nm with a
229 0.5 nm resolution and a 1.6° field of view (FOV) for the retrieval of the total VCDs of NO₂ with a precision of
230 about ~~2.75.4~~ $\times 10^{14}$ molecules/cm² (2.7×10^{14} molecules/cm² for NO₂ SCD) and a nominal accuracy of 2.7×10^{15}
231 molecules cm⁻² under clear-sky conditions (Herman et al., 2009; Lamsal et al., 2014; Zhao et al., 2020). There
232 were 12 Pandora sites operating in the DISCOVER-AQ campaign (Figure S1). Six of them are the same as the P-
233 3B aircraft spiral locations (Aldino, Edgewood, Beltsville, Essex, Fairhill, and Padonia) (Table S1 and Figure
234 S1). The other six sites are Naval Academy (Annapolis Maryland) (USNA – ocean), University of Maryland
235 College Park (UMCP – urban), University of Maryland Baltimore County (UMBC – urban), Smithsonian
236 Environmental Research Center (SERC – rural/coastal), Oldtown in Baltimore (Oldtown – urban), and Goddard
237 Space Flight Center (GSFC – urban/suburban) (Table S1 and Figure S1). In this study, we exclude the USNA site
238 as its measurements were conducted on a ship (“Pandora(w)” in Figure S1), and there were no other surface
239 observations in the corresponding REAM grid cell. Including the data from the USNA site has a negligible effect
240 on the comparisons of observed and simulated NO₂ TVCDs. In our analysis, we ignore Pandora measurements
241 with ~~solar zenith angles~~ (SZA) > 80° (Figure S18) and exclude the data when fewer than three valid
242 measurements are available within an hour to reduce the uncertainties of the hourly averages due to the
243 significant variations of Pandora observations (Figure S29).

244 Since Pandora measures total NO₂ VCDs, we need to subtract stratosphere NO₂ VCDs from the total VCDs
245 to compute TVCDs. As shown in Figure S310, stratosphere NO₂ VCDs show a clear diurnal cycle with an
246 increase during daytime due in part to the photolysis of reactive nitrogen reservoirs such as N₂O₅ and HNO₃

247 (Brohede et al., 2007; Dirksen et al., 2011; Peters et al., 2012; Sen et al., 1998; Spinei et al., 2014), which is
248 consistent with the significant increase of stratospheric NO₂ VCDs from GOME-2A to OMI. In this study, we use
249 the GMI model simulated stratospheric NO₂ VCDs in Figure S310 to calculate the Pandora NO₂ TVCDs. The
250 small discrepancies between the GMI stratospheric NO₂ VCDs and satellite products do not change the pattern of
251 Pandora NO₂ TVCD diurnal variations or affect the conclusions in this study.

252 2.4 ACAM NO₂ VCD measurements

253 The ACAM instrument onboard the UC-12 aircraft consists of two thermally spectrometers in the
254 ultraviolet/visible/near-infrared range. The spectrometer in the ultraviolet/visible band (304 nm – 520 nm) with a
255 resolution of 0.8 nm and a sampling of 0.105 nm can be used to detect NO₂ in the atmosphere. The native ground
256 resolution of UC-12 ACAM NO₂ measurements is 0.5 km × 0.75 km at a flight altitude of about 8 km ASL and a
257 nominal ground speed of 100 m s⁻¹ during the DISCOVER-AQ 2011 campaign (Lamsal et al., 2017), thus
258 providing high-resolution NO₂ VCDs below the aircraft.

259 In this study, we mainly use the ACAM NO₂ VCD product described by Lamsal et al. (2017), which applied
260 a pair-average co-adding scheme to produce NO₂ VCDs at a ground resolution of about 1.5 km (cross-track) ×
261 1.1 km (along-track) to reduce noise impacts. In their retrieval of ACAM NO₂ VCDs, they first used the DOAS
262 fitting method to generate differential NO₂ SCDs relative to the SCDs at an unpolluted reference location. Then
263 they computed above/below-aircraft AMFs at both sampling and reference locations based on the vector
264 linearized discrete ordinate radiative transfer code (VLIDORT) (Spurr, 2008). In the computation of AMFs, the a
265 priori NO₂ vertical profiles were from a combination of a high-resolution (4-km) CMAQ (the Community
266 Multiscale Air Quality Modeling System) model outputs in the boundary layer and a GMI simulation (2° × 2.5°)
267 results elsewhere in the atmosphere. Finally, the below-aircraft NO₂ VCDs at the sampling locations were
268 generated by dividing below-aircraft NO₂ SCDs at the sampling locations by the corresponding below-aircraft

269 AMFs. The below-aircraft NO₂ SCDs were the differences between the total and above-aircraft NO₂ SCDs. The
270 total NO₂ SCDs were the sum of DOAS fitting generated differential NO₂ SCDs and NO₂ SCDs at the reference
271 location, and the above-aircraft NO₂ SCDs were derived based on above-aircraft AMFs, GMI NO₂ profiles, and
272 OMNO₂ stratospheric NO₂ VCDs (Lamsal et al., 2017). The ACAM NO₂ VCD product had been evaluated via
273 comparisons with other independent observations during the DISCOVER-AQ 2011 campaign, such as P-3B
274 aircraft, Pandora, and OMNO₂, and the uncertainty of individual below-aircraft NO₂ VCD is about 30% (Lamsal
275 et al., 2017). To keep the consistency of ACAM NO₂ VCDs, we exclude NO₂ VCDs measured at altitudes < 8 km
276 ASL, which accounts for about 6.8% of the total available ACAM NO₂ VCD data. We regrid the 1.5 km × 1.1
277 km ACAM NO₂ VCDs to the 4-km REAM grid cells (Figure S1), which are then used to evaluate the distribution
278 of NO₂ VCDs in the 4-km REAM simulation. As a supplement in section 3.76, we also assess the 4-km REAM
279 simulation by using the UC-12 ACAM NO₂ VCDs produced by the Smithsonian Astrophysical Observatory
280 (SAO) algorithms, archived on [https://www-air.larc.nasa.gov/cgi-bin/ArcView/discover-aq.dc-](https://www-air.larc.nasa.gov/cgi-bin/ArcView/discover-aq.dc-2011?UC12=1#LIU.XIONG/)
281 [2011?UC12=1#LIU.XIONG/](https://www-air.larc.nasa.gov/cgi-bin/ArcView/discover-aq.dc-2011?UC12=1#LIU.XIONG/) (last access: December 31, 2019) (Liu et al., 2015a; Liu et al., 2015b). This product
282 is an early version of the SAO algorithm used to produce the Geostationary Trace gas and Aerosol Sensor
283 Optimization (GeoTASO) and the GEOstationary Coastal and Air Pollution Events (GEO-CAPE) Airborne
284 Simulator (GCAS) airborne observations in later airborne campaigns (Nowlan et al., 2016; Nowlan et al., 2018).

285 2.5 Surface NO₂ and O₃ measurements

286 The measurement of NO_x is based on the chemiluminescence of electronically excited NO₂^{*}, produced from
287 the reaction of NO with O₃, and the strength of the chemiluminescence from the decay of NO₂^{*} to NO₂ is
288 proportional to the number of NO molecules present (Reed et al., 2016). NO₂ concentrations can be measured
289 with this method by converting NO₂ to NO first through catalytic reactions (typically on the surface of heated
290 molybdenum oxide (MoO_x) substrate) or photolytic processes (Lamsal et al., 2015; Reed et al., 2016). However,
291 for the catalytic method, reactive nitrogen compounds other than NO_x (NO_z), such as HNO₃, peroxyacetyl nitrate

292 (PAN), and other organic nitrates, can also be reduced to NO on the heated surface, thus causing an
293 overestimation of NO₂. The magnitude of the overestimation depends on the concentrations and the reduction
294 efficiencies of interference species, both of which are uncertain. The photolytic approach, which employs
295 broadband photolysis of ambient NO₂, offers more accurate NO₂ measurements (Lamsal et al., 2015).

296 There were 11 NO_x monitoring sites operating in the DISCOVER-AQ region during the campaign (Figure
297 S1), including those from the EPA Air Quality System (AQS) monitoring network and those deployed for the
298 DISCOVER-AQ campaign. Nine of them measured NO₂ concentrations by a catalytic converter. The other two
299 sites (Edgewood and Padonia) had NO₂ measurements from both catalytic and photolytic methods. Different
300 stationary catalytic instruments were used during the campaign: Thermo Electron 42C-Y NO_y analyzer, Thermo
301 Model 42C NO_x analyzer, Thermo Model 42I-Y NO_y analyzer, and Ecotech Model 9843/9841 T-NO_y analyzers.
302 In addition, a mobile platform — NATIVE (Nittany Atmospheric Trailer and Integrated Validation Experiment)
303 with a Thermo Electron 42C-Y NO_y analyzer installed, was also deployed in the Edgewood site. The photolytic
304 measurements of NO₂ in Edgewood and Padonia were from Teledyne API model 200eup photolytic NO_x
305 analyzers. We scale catalytic NO₂ measurements using the diurnal ratios of NO₂ photolytic measurements to NO₂
306 from the corresponding catalytic analyzers (Figure 24). Figure 2-4 shows the lowest photolytic/catalytic ratios in
307 the afternoon, which reflects the production of nitrates and other reactive nitrogen compounds from NO_x in the
308 daytime. When photolytic measurements are available, we only use the photolytic observations in this study;
309 otherwise, we use the scaled catalytic measurements.

310 Nineteen surface O₃ monitoring sites were operating in the DISCOVER-AQ region during the campaign
311 (Figure S1). They measured O₃ concentrations by using a Federal Equivalent Method (FEM) based on the UV
312 absorption of O₃ (<https://www.arb.ca.gov/aaqm/qa/qa-manual/vol4/chapter6o3.pdf>, last access: April 6, 2019)
313 with an uncertainty of 5 ppb.

314 2.6 Aircraft measurements of NO₂ vertical profiles

315 In this study, we mainly use the NO₂ concentrations measured by the National Center for Atmospheric
316 Research (NCAR) 4-channel chemiluminescence instrument (P-CL) onboard the P-3B aircraft for the evaluation
317 of REAM simulated NO₂ vertical profiles. The instrument has a NO₂ measurement uncertainty of 10% – 15% and
318 a 1-second, 1-sigma detection limit of 30 pptv.

319 NO₂ measurements from aircraft spirals provide us with NO₂ vertical profiles. Figure S1 shows the locations
320 of the aircraft spirals during the DISCOVER-AQ campaign, except for the Chesapeake Bay spirals over the
321 ocean. There were only six spirals available over the Chesapeake Bay, which have ignorable impacts on the
322 following analyses. Therefore, we do not use them in this study. The rest 2398 spirals in the daytime for July
323 2011 are used to compute the average profiles of NO₂ for the six inland sites (Figure S1).

324 The aircraft measurements were generally sampled from about a height of 3400 m AGL in the boundary
325 layer to 3.63 km AGL in the free troposphere. We bin these measurements to REAM vertical levels. In order to
326 make up the missing observations between the surface and 3400 m, we apply quadratic polynomial regressions
327 by using aircraft data below 1 km and coincident NO₂ surface measurements.

328 In addition to using NO₂ concentrations from the NCAR 4-channel instrument to evaluate REAM simulated
329 NO₂ vertical profiles, we also use P-3B NO, NO₂, and NO_y concentrations measured by the NCAR 4-channel
330 instrument and NO₂, total peroxyacyl nitrates (Σ PNs), total alkyl nitrates (Σ ANs) (include alkyl nitrates and
331 hydroxyalkyl nitrates), and HNO₃ concentrations measured by the thermal dissociation-laser induced
332 fluorescence (TD-LIF) technique (Day et al., 2002; Thornton et al., 2000; Wooldridge et al., 2010) to evaluate the
333 concentrations of NO_y from REAM (Table 1). All these P-3B measurements are vertically binned to REAM grid
334 cells for comparisons with REAM results. In addition, below the P-3B spirals, four NO_y observation sites at

335 Padonia, Edgewood, Beltsville, and Aldino were operating to provide continuous hourly NO_y surface
336 concentrations during the campaign, which we also use to evaluate REAM simulated NO_y surface concentrations
337 in this study. We summarize the information of available observations at the 11 inland Pandora sites in Table S1.

338 **3 Results and discussion**

339 3.1 Evaluation of WRF simulated meteorological fields

340 We evaluate the performances of the 36-km and nested 4-km WRF simulations using temperature, potential
341 temperature, relative humidity (RH), and wind measurements from the P-3B spirals (Figure 1) and precipitation
342 data from the NCEP (National Centers for Environmental Prediction) Stage IV precipitation dataset. Generally,
343 P-3B spirals range from ~300 m to ~3.63 km in height above the ground level (AGL). As shown in Figure S4,
344 both the 36-km and nested 4-km WRF simulations simulate temperature well with $R^2 = 0.98$. Both WRF
345 simulations show good agreement with P-3B measurements in U-wind (36-km: $R^2 = 0.77$; 4-km: $R^2 = 0.76$), V-
346 wind (36-km: $R^2 = 0.79$; 4-km: $R^2 = 0.78$), wind speed (36-km: $R^2 = 0.67$; 4-km: $R^2 = 0.67$), and wind direction
347 (36-km: $R^2 = 0.46$; 4-km: $R^2 = 0.52$) (Figures S4 and S5). We further compare the temporal evolutions of vertical
348 profiles for temperature, potential temperature, RH, U-wind, and V-wind below 3 km from the P-3B observations
349 with those from the 36-km and nested 4-km WRF simulations in Figure S6. Both WRF simulations well capture
350 the temporospatial variations of P-3B observed vertical profiles except that RH below 1.5 km is significantly
351 underestimated during 9:00 – 17:00 LT in both WRF simulations. The evaluations above suggest that WRF
352 simulated wind fields are good and comparable at 4-km and 36-km resolutions, but potential dry biases exist in
353 both WRF simulations.

354 The NCEP Stage IV precipitation dataset provides hourly precipitation across the contiguous United States
355 (CONUS) with a resolution of ~4 km based on the merging of rain gauge data and radar observations (Lin and

356 [Mitchell, 2005; Nelson et al., 2016](#)). The Stage IV dataset is useful for evaluating model simulations, satellite
357 [precipitation estimates, and radar precipitation estimates \(Davis et al., 2006; Gourley et al., 2011; Kalinga and](#)
358 [Gan, 2010; Lopez, 2011; Yuan et al., 2008\)](#). We obtain the Stage IV precipitation data for July 2011 from the
359 [NCAR/UCAR Research Data Archive \(https://rda.ucar.edu/datasets/ds507.5/](https://rda.ucar.edu/datasets/ds507.5/), last access: December 28, 2019).
360 [As shown in Figures S7 and S8, generally, both the 36-km and nested 4-km WRF simulations generally predict](#)
361 [much less precipitation \(in precipitation amount and duration\) compared to the Stage-IV data in July 2011 around](#)
362 [the DISCOVER-AQ campaign region, especially for the nested 4-km WRF simulation, consistent with the](#)
363 [aforementioned underestimated RH and dry bias in WRF simulations. The precipitation biases in the WRF model](#)
364 [will affect REAM simulations of trace gases, leading to high biases of soluble species due to underestimated wet](#)
365 [scavenging. Clouds interfere with satellite observations. Therefore, the precipitation bias does not affect model](#)
366 [evaluations with satellite measurements of NO₂. Aircraft measurements were also taken in non-precipitating days.](#)

367 3.2.4 Effect of boundary layer vertical mixing on the diurnal variations of surface NO₂ concentrations

368 3.2.4.1 36-km model simulation in comparison to the surface observations

369 Figures [53a](#) and [53b](#) show the observed and 36-km REAM simulated diurnal cycles of surface NO₂ and O₃
370 concentrations on weekdays in July 2011 in the DISCOVER-AQ region. REAM with WRF-[YSU](#) simulated
371 vertical diffusion coefficient (k_{zz}) values significantly overestimates NO₂ concentrations and underestimates O₃
372 concentrations at night, although it captures the patterns of the diurnal cycles of surface NO₂ and O₃: an O₃ peak
373 and a NO₂ minimum around noontime. [Here, YSU denotes the Yonsei University planetary boundary layer \(PBL\)](#)
374 [scheme \(Shin and Hong, 2011\) used by our WRF simulations \(Table S2\)](#). At night, the reaction of O₃ + NO → O₂
375 + NO₂ produces NO₂ but removes O₃. Since most NO_x emissions are in the form of NO, the model biases of low
376 O₃ and high NO₂ occur at the same time. Since there are no significant chemical sources of O₃ at night, mixing of
377 O₃ rich air above the surface is the main source of O₃ supply near the surface. Therefore, the nighttime model

378 biases with WRF-YSU simulated k_{zz} data in Figure 53 indicate that vertical mixing may be underestimated at
379 night.

380 During the DISCOVER-AQ campaign, WRF simulated vertical wind velocities are very low at night and
381 have little impact on vertical mixing (Figure S911a). The nighttime vertical mixing is mainly attributed to
382 turbulent mixing. In ~~the YSU scheme the Yonsei University (YSU) planetary boundary layer (PBL) scheme (Shin~~
383 ~~and Hong, 2011) used by our WRF simulations (Table S2)~~, boundary layer k_{zz} is correlated to PBLH. However,
384 Breuer et al. (2014) and Hu et al. (2012) found that the YSU scheme underestimated nighttime PBLHs in WRF,
385 which is consistent with Figure 64 showing that WRF-YSU k_{zz} -determined PBLHs are significantly lower than
386 lidar observations in the late afternoon and at night at the UMBC site during the DISCOVER-AQ campaign.
387 Here, the k_{zz} -determined PBLH refers to the mixing height derived by comparing k_{zz} to its background values
388 (Hong et al., 2006) but not the PBLH outputs from WRF. The lidar mixing depth data were derived from the
389 Elastic Lidar Facility (ELF) attenuated backscatter signals by using the covariance wavelet transform method and
390 had been validated against radiosonde measurements, Radar wind profiler observations, and Sigma Space mini-
391 micropulse lidar data (Compton et al., 2013). To improve nighttime PBLHs and vertical mixing in REAM, we
392 increase REAM- k_{zz} below 500 m during 18:00 – 5:00 LT to 5 m s^{-2} if the WRF-YSU computed $k_{zz} < 5 \text{ m s}^{-2}$,
393 which significantly increases the k_{zz} -determined PBLHs at night (Figure 64), leading to the decreases of simulated
394 surface NO_2 and the increases of surface O_3 concentrations at night (Figure 53). The assigned value of 5 m s^{-2} is
395 arbitrary. Changing this value to 2 or 10 m s^{-2} can also alleviate the biases of model simulated nighttime surface
396 NO_2 and O_3 concentrations (Figure S10). An alternative solution to correct the model nighttime simulation biases
397 is to reduce NO_x emissions by 50-67%, but we cannot find good reasons to justify this level of NO_x emission
398 reduction only at night.

399 The updated REAM simulation of surface NO₂ diurnal pattern in Figure 53a is in good agreement with
400 previous studies (Anderson et al., 2014; David and Nair, 2011; Gaur et al., 2014; Reddy et al., 2012; [Zhao et al.,](#)
401 [2019](#)). Daytime surface NO₂ concentrations are much lower compared to nighttime, and NO₂ concentrations
402 reach a minimum around noontime. As shown in Figure S112, under the influence of vertical turbulent mixing,
403 the surface-layer NO_x emission diurnal pattern is similar to the surface NO₂ diurnal cycle in Figure 53a,
404 emphasizing the importance of turbulent mixing on modulating surface NO₂ diurnal variations. The highest
405 boundary layer (Figure 64) due to solar radiation leads to the lowest surface-layer NO_x emissions (Figure S112)
406 and, therefore, the smallest surface NO₂ concentrations occur around noontime (Figure 53a). Transport, which is
407 mainly attributed to advection and turbulent mixing, is another critical factor affecting surface NO₂ diurnal
408 variations (Figure S112). The magnitudes of transport fluxes (Figure S112) are proportional to horizontal and
409 vertical gradients of NO_x concentrations and are therefore generally positively correlated to surface NO₂
410 concentrations. However, some exceptions exist, reflecting different strengths of advection (U, V, and W) and
411 turbulent mixing (k_{zz}) at different times. For example, in the early morning, NO₂ surface concentrations peak at
412 5:00 – 6:00 LT (Figure 53a), while transport fluxes peak at 7:00 – 8:00 LT (Figure S112). The delay of the peak
413 is mainly due to lower turbulent mixing at 5:00 – 6:00 LT than other daytime hours in the model (Figure 64).
414 Chemistry also contributes to surface NO₂ diurnal variations mainly through photochemical sinks in the daytime
415 and N₂O₅ hydrolysis at nighttime. Chemistry fluxes in Figure S112 are not only correlated to the strength of
416 photochemical reactions and N₂O₅ hydrolysis (chemistry fluxes per unit NO_x) but are also proportional to NO_x
417 surface concentrations. Therefore, chemistry fluxes in Figure S112 cannot directly reflect the impact of solar
418 radiation on photochemical reactions. It can, however, still be identified by comparing afternoon chemistry
419 contributions: from 13:00 to 15:00 LT, surface-layer NO_x emissions and NO₂ concentrations are increasing
420 (Figures S112 and 53a); however, chemistry losses are decreasing as a result of the reduction of photochemical
421 sinks with weakening solar radiation. The contributions of vertical mixing and photochemical sinks to NO₂

422 concentrations can be further corroborated by daytime variations of NO₂ vertical profiles (~~Figure 6~~) and TVCDs
423 (~~Figure S13~~) discussed in sections 3.32 and 3.43.

424 Figure 53c shows the diurnal variation on weekends is also simulated well in the improved 36-km model.
425 The diurnal variation of surface NO₂ concentrations (REAM: 1.5 – 10.24 ppb; observations: 2.1 – 9.8 ppb) is
426 lower than on weekdays (REAM: 2.45 – 12.25 ppb; observations: 3.3 – 14.5 ppb), reflecting lower magnitude
427 and variation of NO_x emissions on weekends (Figure 34). Figure 53d also shows an improved simulation of
428 surface O₃ concentrations at nighttime due to the improved PBLH simulation (Figure 64).

429 3.21.2 4-km model simulation in comparison to the surface observations

430 The results of 4-km REAM simulations with original WRF-YSU k_{zz} (not shown) are very similar to Figure
431 53 since WRF simulated nocturnal vertical mixing is insensitive to the model horizontal resolution. Applying the
432 modified nocturnal mixing in the previous section also greatly reduced the nighttime NO₂ overestimate and O₃
433 underestimate in the 4-km REAM simulations. All the following analyses are based on REAM simulations with
434 improved nocturnal mixing. Figure 75 shows that mean surface NO₂ concentrations simulated in the 4-km model
435 are higher than the 36-km results over Padonia, Oldtown, Essex, Edgewood, Beltsville, and Aldino (Table S1),
436 leading to generally higher biases compared to the observations at night in the daytime. A major cause is that the
437 observation sites are located in regions of high NO_x emissions (Figures S1 and S2). At a higher resolution of 4
438 km, the high emissions around the surface sites are apparent compared to rural regions. At the coarser 36-km
439 resolution, spatial averaging greatly reduces the emissions around the surface sites. On average, NO_x emissions
440 (molecules km⁻² s⁻¹) around the six surface NO₂ observations sites are 67% higher in the 4-km than the 36-km
441 REAM simulations (Table S1). The resolution dependence of model results will be further discussed in the model
442 evaluations using the other in situ and remote sensing measurements.

3.32 Diurnal variations of NO₂ vertical profiles

Figures 86a and 86c show the temporal variations of P-3B observed and 36-km REAM simulated NO₂ vertical profiles in the daytime on weekdays during the DISCOVER-AQ campaign. 36-km REAM reproduces well the observed characteristics of NO₂ vertical profiles in the daytime ($R^2 = 0.8994$), which are strongly affected by vertical mixing and photochemistry (Zhang et al., 2016). When vertical mixing is weak in the early morning (6:00 – 8:00 LT), NO₂, released mainly from surface NO_x sources, is concentrated in the surface layer, and the vertical gradient is large. As vertical mixing becomes stronger after 8:00 LT, NO₂ concentrations below 500 m decrease significantly, while those over 500 m increase from 6:00 – 8:00 LT to 12:00 – 14:00 LT. It is noteworthy that PBLHs and NO_x emissions are comparable between 12:00 – 14:00 LT and 15:00 – 17:00 LT (Figures 34 and 64); however, NO₂ concentrations at 15:00 – 17:00 LT are significantly higher than at 12:00 – 14:00 LT in the whole boundary layer, reflecting the impact of the decreased photochemical loss of NO_x in the late afternoon. In fact, photochemical losses affect all the daytime NO₂ vertical profiles, which can be easily identified by NO₂ TVCD process diagnostics discussed in section 3.43 (Figure S139).

Figures 86b and 86d also show the observed and 36-km REAM simulated vertical profiles on weekends. Similar to Figures 53 and 75, observed and simulated concentrations of NO₂ are lower on weekends than on weekdays. Some of the variations from weekend profiles are due to a lower number of observations (47 spirals) on weekends. The overall agreement between the observed vertical profiles and 36-km model results is good on weekends ($R^2 = 0.874$). At 15:00 – 17:00 LT, the model simulates a larger gradient than what the combination of aircraft and surface measurements indicates. It may be related to the somewhat underestimated PBLHs in the late afternoon in the model (Figure 64).

On weekdays, most simulated vertical profiles at the 4-km resolution (Figure 86e) are similar to 36-km results in part because the average NO_x emissions over the six P-3B spiral sites are about the same, 4% lower in

465 the 4-km than the 36-km REAM simulations (Table S1). A clear exception is the 4-km REAM simulated vertical
466 profile at 15:00 – 17:00 LT when the model greatly overestimates boundary layer NO_x mixing and
467 concentrations. The main reason is that WRF simulated vertical velocities (w) in the late afternoon are much
468 larger in the 4-km simulation than the 36-km simulation (Figure S944), which can explain the simulated fully
469 mixed boundary layer at 15:00 – 17:00 LT. Since it is not designed to run at the 4-km resolution and it is
470 commonly assumed that convection can be resolved explicitly at high resolutions, the [Kain-Fritsch \(new Eta\)](#)
471 convection scheme is not used in the nested 4-km WRF simulation (Table S2); it may be related to the large
472 vertical velocities in the late afternoon when thermal instability is the strongest. Appropriate convection
473 parameterization is likely still necessary for 4-km simulations (Zheng et al., 2016), which may also help alleviate
474 the underestimation of precipitation in the nested 4-km WRF simulation as discussed in section 3.2.1.

475 The same rapid boundary-layer mixing due to vertical transport is present in the 4-km REAM simulated
476 weekend vertical profile (Figure 86f), although the mixing height is lower. Fewer spirals (47) and distinct
477 transport effect due to different NO₂ horizontal gradients between the 4-km and 36-km REAM simulations
478 (discussed in detail in Section 3.65) may cause the overestimation of weekend profiles in the 4-km REAM
479 simulation.

480 3.43 Daytime variation of NO₂ TVCDs

481 We compare satellite, P-3B aircraft, and model-simulated TVCDs with Pandora measurements, which
482 provide continuous daytime observations. The locations of Pandora sites are shown in Table S1 and Figure S1.
483 Among the Pandora sites, four sites are located significantly above the ground level: UMCP (~20 m), UMBC
484 (~30 m), SERC (~40 m), and GSFC (~30 m). The other sites are 1.5 m AGL. To properly compare Pandora to
485 other measurements and model simulations, we calculate the missing TVCDs between the Pandora site heights
486 and ground surface by multiplying the Pandora TVCDs with model-simulated TVCD fractions of the

487 corresponding columns. The resulting correction is 2-210% ($\frac{1}{1-\text{missing TVCD percentage}}$) for the four sites
488 significantly above the ground surface, but the effect on the averaged daytime TVCD variation of all Pandora
489 sites is small (Figure S124). In the following analysis, we use the updated Pandora TVCD data.

490 The weekday diurnal variations of NO₂ TVCDs from satellites, Pandora, 4- and 36-km REAM, and the P-3B
491 aircraft are shown in Figure 107a. We calculate aircraft derived TVCDs by using equation (1):

$$492 \text{TVCD}_{\text{aircraft}}(t) = \frac{\sum c_{\text{aircraft}}(t) \times \rho_{\text{REAM}}(t) \times V_{\text{REAM}}(t)}{A_{\text{REAM}}} \quad (1),$$

493 where t is time; c_{aircraft} (v/v) denotes aircraft NO₂ concentrations (mixing ratios) at each level at time t ; ρ_{REAM}
494 ($\text{molecules} / \text{cm}^3$) is the density of air from 36-km REAM at the corresponding level; V_{REAM} (cm^3) is the volume of
495 the corresponding 36-km REAM grid cell; A_{REAM} (cm^2) is the surface area ($36 \times 36 \text{ km}^2$). In the calculation, we
496 only use NO₂ concentrations below 3.63 km AGL because few aircraft measurements were available above this
497 height in the campaign. Missing tropospheric NO₂ above 3.63 km AGL in the aircraft TVCD calculation has little
498 impact on our analyses, as 36-km REAM model simulation shows that $85\% \pm 742\%$ of tropospheric NO₂ are
499 located below 3.63 km AGL during 6:00 – 17:00 LT in the DISCOVER-AQ region, which is roughly consistent
500 with the GMI model results with 85% - 90% tropospheric NO₂ concentrated below 5 km (Lamsal et al., 2014). It
501 should be noted that only six P-3B spirals are available during the campaign, less than the samplings of 11 inland
502 Pandora sites.

503 The 4-km REAM simulated NO₂ TVCDs are mostly higher than the 36-km results and the observations in
504 daytime on weekdays (Figure 107a). However, since the standard deviations of the data are much larger than the
505 model difference, the 4- and 36-km model results ~~show generally~~ generally show similar characteristics relative
506 to the observations. REAM simulation results are in reasonable agreement with Pandora, P-3B aircraft, and
507 satellite daytime NO₂ TVCDs, except that NASA-derived OMI (OMNO2) TVCDs are somewhat lower than

508 other datasets, which may be partly due to biased a priori vertical profiles from the GMI model in the NASA
509 retrieval in the campaign (Lamsal et al., 2014; Lamsal et al., 2020). TVCDs derived by using the DOMINO
510 algorithm and 36-km REAM NO₂ vertical profiles are in agreement with those from KNMI, which indicates that
511 the TM4 model from KNMI provides reasonable estimates of a priori NO₂ vertical profiles on weekdays in the
512 DISCOVER-AQ region in summer.

513 We find evident decreases of NO₂ TVCDs from GOME-2A to OMI in Figure 107a, which is consistent with
514 Pandora, REAM results, and previous studies that showed decreasing NO₂ TVCDs from SCIAMACHY to OMI
515 due to photochemical losses in summer (Boersma et al., 2008; Boersma et al., 2009). P-3B aircraft TVCDs also
516 show this decrease feature but have large variations due in part to the limited aircraft sampling data.

517 Pandora NO₂ TVCD data have different characteristics from REAM simulated and P-3B aircraft measured
518 TVCDs at 5:00 – 7:00 LT and 14:00 – 18:00 LT (Figure 107a). At 5:00 – 7:00 LT, Pandora data show a
519 significant increase of NO₂ TVCDs, but REAM and aircraft TVCDs generally decrease except for 4-km REAM
520 TVCDs with a slight increase from 6:00 – 7:00 LT on weekdays. At 14:00 LT – 18:00 LT, Pandora TVCDs have
521 little variations, but REAM and aircraft TVCDs increase significantly. The relatively flat Pandora TVCDs in the
522 late afternoon compared to REAM and P-3B aircraft measurements are consistent with Lamsal et al. (2017),
523 which found the significant underestimation (26% – 30%) of Pandora VCDs compared to UC-12 ACAM
524 measurements from 16:00 LT to 18:00 LT during the DISCOVER-AQ campaign. We show the simulated effects
525 of emission, chemistry, transport, and dry deposition on NO_x TVCDs in Figure S139. The simulated early
526 morning slight decrease of NO₂ TVCDs is mainly due to the chemical transformation between NO₂ and NO
527 favoring the accumulation of NO under low-O₃ and low-HO₂/RO₂ conditions, thus NO TVCDs increase
528 significantly but NO₂ TVCDs continue decreasing slowly during the period. The increase in the late afternoon is
529 primarily due to the decrease of photochemistry-related sinks. The reasons for the discrepancies of NO₂ TVCDs

530 between Pandora and REAM results during the above two periods are unclear. Large SZAs in the early morning
531 and the late afternoon (Figure S18) lead to the higher uncertainties of Pandora measurements (Herman et al.,
532 2009), although we have excluded Pandora measurements with $SZA > 80^\circ$. In addition, Pandora is a sun-tracking
533 instrument with a small effective FOV and is sensitive to local conditions within a narrow spatial range which
534 may differ significantly from the average properties of 36- and 4-km grid cells depending upon the time of the
535 day (Figure S139) (Herman et al., 2009; Herman et al., 2018; Herman et al., 2019; Judd et al., 2018; Judd et al.,
536 2019; Judd et al., 2020; Lamsal et al., 2017; Reed et al., 2015). As we mentioned above, ~85% tropospheric NO₂
537 are located below 3.63 km in the DISCOVER-AQ 2011 region based on the 36-km REAM simulation results.
538 The Pandora FOV of 1.6° is approximately equivalent to a nadir horizontal extension of only 0.1 km
539 ($2 \times 3.63 \text{ km} \times \tan \frac{1.6}{2} = 0.1 \text{ km}$) at 3.63 km AGL and 30 m at 1.0 km AGL. Therefore, Pandora measures
540 different air columns of NO₂ at different times of the day, especially in the morning and afternoon when SZA is
541 large, as shown in Figure S13. Considering the potential spatial heterogeneity of boundary-layer NO₂, it is
542 possible that the morning (east), noontime (nadir), afternoon (west) NO₂ VCDs are significantly different from
543 each other. Unlike Pandora, satellites and aircraft are far from the ground surface and cover large areas; therefore,
544 the impact of SZA on their NO₂ VCD measurements is insignificant compared to Pandora measurements.
545 Another possible reason is that Pandora instruments had few observations in the early morning, and the resulting
546 average may not be representative (Figure S29).

547 To further understand the daytime variation of NO₂ TVCDs, we examine P-3B aircraft data derived and
548 REAM simulated NO₂ VCD variations for different height bins (Figure 118). NO₂ VCDs below 3.63 km AGL
549 display a “U”-shaped pattern from 5:00 LT to 17:00 LT. In the morning, as vertical mixing becomes stronger
550 after sunrise, high-NO_x air in the lower layer is mixed with low-NO_x air in the upper layer. The increase of NO_x
551 vertical mixing above 3400 m is sufficient to counter the increase of photochemical loss in the morning.

552 Conversely, the NO₂ VCDs below 3400 m decrease remarkably from sunrise (about 6:00 LT) to around noontime
553 due to both vertical mixing and the increase of photochemical strength. From 13:00 LT to 16:00 LT, NO₂ VCDs
554 increase slowly, reflecting a relative balance among emissions, transport, chemistry, and dry depositions. The
555 sharp jump of the VCDs from 16:00 LT to 17:00 LT is mainly due to dramatically reduced chemical loss. And 4-
556 km REAM simulated NO₂ VCDs at 0.340-3.63 km at 16:00-17:00 LT are much higher than 36-km results partly
557 because of the rapid vertical mixing in the 4-km REAM simulation (Figures 86 and S914).

558 Similar to NO₂ surface concentrations and vertical profiles in Figures 75 and 86, the NO₂ TVCD variation is
559 also smaller on weekends than on weekdays, but the day-night pattern is similar (Figure 107). Although the 4-km
560 REAM NO₂ TVCDs are generally higher than the 36-km results and observations in the daytime, considering
561 their large standard deviations, NO₂ TVCDs from both simulations are comparable to satellite products, Pandora,
562 and P-3B aircraft observations most of the time on weekends. The exception is that Pandora TVCDs have much
563 lessdifferent variation patterns in the early morning and late afternoon than from REAM simulations, similar to
564 those found on weekdays and aircraft datasets. ~~Another anomaly is that KNMI GOME 2A TVCDs at 9:30 LT are~~
565 ~~much larger than the other datasets, while the GOME 2A TVCDs retrieved using 36 km REAM profiles shows~~
566 ~~comparable TVCDs to Pandora, REAM, and aircraft datasets, reflecting possible biased NO₂ a priori profiles~~
567 ~~from the TM4 model on weekends used in the KNMI GOME 2A retrieval.~~

568 3.54 Model comparisons with NO_y measurements

569 NO_y is longer-lived than NO_x, and NO_y concentrations are not affected by chemistry as much as NO_x. We
570 obtain two types of NO_y concentrations from the P-3B aircraft in the DISCOVER-AQ campaign: one is NO_y
571 concentrations directly measured by the NCAR 4-channel instrument, corresponding to the sum of NO, NO₂,
572 ΣPNs, ΣANs, HNO₃, N₂O₅, HNO₄, HONO, and the other reactive nitrogenic species in REAM (all the other
573 species are described in Table 1); the other one, which we name as “derived-NO_y”, is the sum of NO from the

574 NCAR 4-channel instrument and NO₂ (NO₂_LIF), ΣPNs, ΣANs, and HNO₃ measured by the TD-LIF technique,
575 corresponding to NO, NO₂, ΣPNs, ΣANs, and HNO₃ in REAM (Table 1). On average, P-3B derived-NO_y
576 concentrations (2.88 ± 2.24 ppb) are 17% higher than coincident P-3B NO_y concentrations (2.46 ± 2.06 ppb) with
577 R² = 0.75, generally reflecting consistency between these two types of measurements. As shown in Table 1, on
578 weekdays, the 36-km REAM NO_y concentrations are 45% larger than P-3B with R² = 0.33, and the 36-km
579 REAM derived-NO_y concentrations are 8% larger than P-3B with R² = 0.41. 4-km REAM show similar results,
580 suggesting that REAM simulations generally reproduce the observed NO_y and derived-NO_y concentrations within
581 the uncertainties, although the average values from REAM are somewhat larger than the observations due in part
582 to the underestimate of precipitation in the WRF model simulations resulting in underestimated wet scavenging
583 of HNO₃ in REAM. The concentrations of weekday NO, NO₂, and ΣPNs from REAM simulations are also
584 comparable to the observations. However, weekday ΣANs concentrations are 68% lower in the 36-km REAM
585 than observations, suggesting that the chemistry mechanism in REAM may need further improvement to better
586 represent isoprene nitrates. It is noteworthy that, since ΣANs only account for a small fraction (~11%) in
587 observed derived-NO_y, the absolute difference between REAM simulated and P-3B observed ΣANs
588 concentrations is still small compared to HNO₃. Weekday HNO₃ concentrations are significantly higher in
589 REAM simulations (36-km: 57%, 0.65 ppb; 4-km: ~~740%~~, 0.8~~62~~ ppb) than P-3B observations, which is the main
590 reason for the somewhat larger NO_y and derived-NO_y concentrations in REAM compared to P-3B observations.
591 The higher HNO₃ concentrations in REAM may be related to the underestimation of precipitation in the
592 corresponding WRF simulations, as discussed in section 32.1 (Figures S75 and S8), leading to the underestimated
593 wet scavenging of HNO₃, especially for the 4-km REAM simulation.

594 We also examine the weekday diurnal variations of derived-NO_y vertical profiles from P-3B and REAM
595 simulations in Figure S145. Generally, both 36- and 4-km REAM simulations capture the variation characteristics
596 of observed vertical profiles, which are similar to those for NO₂ in Figure 86. REAM derived-NO_y concentrations

597 are comparable to P-3B observations at most vertical levels on weekdays. Some larger derived-NO_y
598 concentrations in the model results can be partially explained by larger HNO₃ concentrations in REAM, such as
599 those below 1 km at 9:00 – 11:00 LT for the 36-km REAM and those below 2.0 km at 12:00 – 17:00 LT for the
600 4-km REAM (Figure S156).

601 Figure 129 shows the comparison of the diurnal cycles of surface NO_y concentrations observed at Padonia,
602 Edgewood, Beltsville, and Aldino during the DISCOVER-AQ campaign with those from the REAM simulations.
603 Generally, the REAM simulations reproduce the observed surface NO_y diurnal cycles except for the spikes
604 around 17:00 – 20:00 LT due to still underestimated PBLHs (Figure 64). 4-km simulation results have a higher
605 bias than 36-km results relative to the observations in the daytime, similar to the comparisons of NO₂ surface
606 concentrations and TVCDs in Figures 75 and 107 due to higher emissions around the observation sites in 4- than
607 36-km simulations (Table S1 and Figure S2).

608 3.65 Resolution dependence of NO_x emission distribution

609 We show previously that the 4-km REAM simulated NO₂ and NO_y surface concentrations and NO₂ TVCDs
610 are higher than observations at-in the daytime in comparison to the corresponding 36-km REAM results (Figures
611 7, 10, and 12). An examination of monthly mean NO₂ surface concentrations and TVCDs for July 2011 also
612 shows that 4-km simulation results are significantly higher than the 36-km results over the 11 inland Pandora
613 sites in the daytime (Figure 13S17). The process-level diagnostics in Figure 9S13 indicate that the mean
614 contribution of NO_x emissions to NO_x ΔTVCDs in the 4-km simulation is 1.32×10^{15} molecules cm⁻² h⁻¹ larger
615 than that in the 36-km simulation between 9:00 LT and 16:00 LT, while the absolute mean contributions of
616 chemistry and transport (they are negative in Figure S139, so we use absolute values here) in the 4-km simulation
617 are 0.262×10^{15} and 0.8799×10^{15} molecules cm⁻² h⁻¹ larger than the 36-km simulation, respectively. The
618 contributions of dry deposition to NO_x ΔTVCDs are negligible compared to other factors in both simulations

619 (Figure [S139](#)). Therefore, the 34% higher NO_x emissions over the 11 inland Pandora sites (Table S1 and Figure
620 [34](#)) is the main reason for the larger daytime NO₂ surface concentrations and TVCDs in the 4-km than the 36-km
621 REAM simulations (Figure [S1713](#)). The significantly different contribution changes between NO_x emissions
622 (1.32×10^{15} molecules cm⁻² h⁻¹ or about one third) and chemistry (0.262×10^{15} molecules cm⁻² h⁻¹ or about [87%](#))
623 reflect potential chemical nonlinearity (Li et al., 2019; Silvern et al., 2019; Valin et al., 2011) and transport effect.
624 Different transport contributions between the 4-km and the 36-km REAM are mainly caused by their different
625 NO_x horizontal gradients (Figures [S2](#) and [14](#), and [150](#)), while the impact of wind fields is small since we do not
626 find significant differences in horizontal wind components between the two simulations except for some lower
627 wind speeds below 1000 m for the 36-km WRF simulation compared to the nested 4-km WRF simulation (Figure
628 [S168](#)). Our sensitivity tests with the WRF Single-Moment 3-class (WSM3) simple ice scheme (not shown) can
629 improve the wind speed comparison below 1000 m between the 36-km and nested 4-km WRF simulations but
630 still produce similar NO_x simulation results as WSM6 shown here. Therefore, the somewhat lower wind speeds
631 below 1000 m in the 36-km WRF simulation are not the reason for the difference between the 4-km and 36-km
632 REAM simulations. The impact of transport on the two REAM simulations can be further verified by the
633 comparison of NO₂ TVCDs over the six P-3B spiral sites between the two simulations (Figure [S179](#)). Mean NO_x
634 emissions over the six P-3B spiral sites are close (relative difference < 4%) between the two simulations (Table
635 S1 and Figure [S179](#)). From 9:00 to 12:00 LT, the contributions of NO_x emissions to NO_x ΔTVCDs are $2.50 \times$
636 10^{15} and 2.49×10^{15} molecules cm⁻² h⁻¹ for the 36-km and 4-km REAM simulations, respectively, and the
637 contributions of chemistry are also close between the two simulations (36-km: -2.6462×10^{15} molecules cm⁻² h⁻¹;
638 4-km: -2.698×10^{15} molecules cm⁻² h⁻¹). However, the contributions of transport are -0.3239×10^{15} and 0.0403
639 $\times 10^{15}$ molecules cm⁻² h⁻¹ for the 36-km and 4-km REAM simulations, respectively, leading to larger NO₂ TVCDs
640 in the 4-km REAM simulation than the 36-km REAM from 9:00 – 12:00 LT (Figure [S179c](#)). Since horizontal
641 wind fields over the six P-3B spiral sites are comparable between two simulations (Figures [S43](#), [S45](#), [S6](#), and

642 S168) and larger NO_x horizontal gradients are found near the P-3B spiral sites for the 4-km REAM (Figure S2),
643 we attribute the different transport contributions between the two simulations to a much larger NO_x emission
644 gradient around the measurement locations in 4-km than 36-km emission distributions.

645 We re-grid the 4-km REAM results into the grid cells of the 36-km REAM, which can significantly reduce
646 the impact of different NO_x emission distributions and associated transport on the two simulations. Compared to
647 the original 4-km REAM results, the re-gridded surface NO₂ concentrations and TVCDs over the 11 inland
648 Pandora sites are much closer to the 36-km REAM results (Figure S1713). After re-gridding the 4-km REAM
649 results into 36-km REAM grid cells, we also find more comparable NO_y surface concentrations between the re-
650 gridded 4-km results and the 36-km REAM results (Figure S1829). The remaining discrepancies between the re-
651 gridded results and the 36-km REAM results may be due to chemical nonlinearity and other meteorological
652 effects, such as larger vertical wind in the 4-km REAM (Figure S944) and their different k_{zz} values in the PBL.
653 Although other factors, such as chemical nonlinearity and vertical diffusion, may affect the 36-km and 4-km
654 REAM simulations differently, the difference between 4- and 36-km simulations of reactive nitrogen is largely
655 due to that of NO_x emissions.

656 The 4- and 36-km simulation difference depends on the location of the observations. In some regions, the
657 NO_x emission difference between 4- and 36-km simulations is small. The comparison of NO_y measurements from
658 P-3B spirals with coincident REAM results in Table 1 suggests that the 4-km and 36-km REAM simulations
659 produce similar NO_y (relative difference ~24%) and derived-NO_y (relative difference ~64%) concentrations on
660 weekdays, and both simulation results are comparable to the observations. The NO_y similarity over the P-3B
661 spiral sites between the 36-km and 4-km REAM simulations is consistent with the comparable NO_x emissions
662 over (relative difference < 4%) the six P-3B spiral sites between the two simulations (Table S1). The differences
663 between the 4-km model simulation results and P3-B observations are larger on weekends than on weekdays

664 (Table 1) due to the limited weekend sampling since model simulated monthly mean values show similar
665 differences between the 4-km and 36-km REAM simulations on weekends as on weekdays (not shown).

666 3.76 Evaluation of 36- and 4-km NO_x distribution with OMI, GOME-2A, and ACAM measurements

667 The evaluation of model simulations of surface, aircraft, and satellite observations tends to point out a high
668 bias in 4- than 36-km model simulations. We note that this comparison is based on the averages of multiple sites.
669 NO_x emissions at individual sites are not always higher in the 4-km than 36-km REAM, such as SERC, Fairhill,
670 and Essex, with much higher 36-km NO_x emissions than 4-km NO_x emissions (Table S1). We conduct
671 individual-site comparisons of surface NO₂ concentrations, surface NO_y concentrations, NO₂ vertical profiles,
672 derived-NO_y vertical profiles, and NO₂ TVCDs of the 36-km REAM and the 4-km REAM results relative to the
673 corresponding observations in Figures S19 – S23. The 36-km simulation results can be larger, smaller, or
674 comparable to the 4-km simulation results, and both simulations can produce higher, lower, or similar results as
675 the observations for different variables at different sites. The varying model biases depending on the observation
676 site reflect the different spatial distributions of NO_x emissions between the 36- and 4-km REAM simulations
677 (Figure 2) and suggest potential distribution biases of NO_x emissions in both simulations. However, we note that
678 the uncertainties of the observations and model data are often comparable or larger than the model differences.

679 Here we examine the 4-km model simulated NO₂ VCDs with high-resolution ACAM measurements onboard
680 the UC-12 aircraft in Figures ~~140~~ and S241, respectively. The spatial distributions of ACAM and 4-km REAM
681 NO₂ VCDs are generally consistent with $R^2 = 0.357$ on weekdays and $R^2 = 0.50$ on weekends. The domain
682 averages of ACAM and 4-km REAM NO₂ VCDs are 4.7 ± 2.0 and $4.65 \pm 3.2 \times 10^{15}$ molecules cm⁻² on weekdays
683 and 3.0 ± 1.7 and $3.3 \pm 2.78 \times 10^{15}$ molecules cm⁻² on weekends, respectively. The spatial distributions of ACAM
684 and 4-km REAM NO₂ VCDs are highly correlated with the spatial distribution of 4-km NEI2011 NO_x emissions.
685 All three distributions capture two strong peaks around Baltimore and Washington, D.C. urban regions and

686 another weak peak in the northeast corner of the domain (Wilmington city in Delaware) (Figures 140 and S244).
687 However, Figures 140 and S244 clearly show that NO₂ VCDs from the 4-km REAM simulation are more
688 concentrated in Baltimore and Washington, D.C. urban regions than ACAM, which are also reflected by the
689 higher NO₂ VCD standard deviations of the 4-km REAM results than ACAM. Several Pandora sites are in the
690 highest NO₂ VCD regions where the 4-km REAM generally produces larger NO₂ VCDs than ACAM, which
691 explains why the NO₂ TVCDs over the 11 Pandora sites from the 4-km REAM simulation are higher than the
692 observations (Figure 107) and the 36-km REAM results (Figure 13S17) around noontime. Horizontal transport
693 cannot explain the NO₂ VCD distribution biases in the 4-km REAM simulation due to the following reasons.
694 Firstly, horizontal wind fields are simulated as well by the nested 4-km WRF simulation as the 36-km WRF
695 compared to P-3B measurements, as discussed in section 32.1. Secondly, the prevailing northwest wind in the
696 daytime (Figure S54) should move NO_x eastward, but we find no significant eastward shift of NO₂ VCDs
697 compared to NO_x emissions in both ACAM and 4-km REAM distributions (Figure 140). Lastly, we find a local
698 minimum of NO₂ VCDs in the middle of the Baltimore urban region (the purple circle in Figure 10b14b) in the
699 ACAM distribution, which cannot be explained by horizontal transport or chemical nonlinearity due to the
700 surrounding high NO_x emissions in the 4-km REAM simulation. Therefore, we attribute the distribution
701 inconsistency between ACAM and the 4-km REAM to the distribution biases of NEI2011 NO_x emissions at the
702 4-km resolution since the average below-aircraft NO₂ VCDs between ACAM and the 4-km REAM are about the
703 same.

704 It is noteworthy that about 91% ACAM NO₂ VCD data are measured from 8:00 – 16:00 LT, and only using
705 ACAM NO₂ VCDs between 8:00 and 16:00 LT for the above comparison does not affect our results shown here.
706 Moreover, to minimize the effect of overestimated afternoon vertical mixing (Figure 86) on the 4-km REAM
707 simulation results, we also examine the comparison between ACAM NO₂ VCDs from 9:00 – 14:00 LT with
708 coincident 4-km REAM results, which produces similar results as shown here.

709 We also evaluate the NO₂ VCD distributions from the 4-km REAM simulation on weekdays and weekends
710 with ACAM NO₂ VCDs below the U-12 aircraft obtained from [https://www-air.larc.nasa.gov/cgi-](https://www-air.larc.nasa.gov/cgi-bin/ArcView/discover-aq.dc-2011?UC12=1#LIU.XIONG/)
711 [bin/ArcView/discover-aq.dc-2011?UC12=1#LIU.XIONG/](https://www-air.larc.nasa.gov/cgi-bin/ArcView/discover-aq.dc-2011?UC12=1#LIU.XIONG/) in Figures S252 and S263. Although the domain mean
712 ACAM NO₂ VCDs in Figures S252 and S263 are higher than coincident 4-km REAM results due to the different
713 retrieval method from Lamsal et al. (2017), such as different above-aircraft NO₂ VCDs and different a priori NO₂
714 vertical profiles, we can still find clear distribution inconsistencies between the 4-km REAM and ACAM NO₂
715 VCDs. The 4-km REAM NO₂ VCDs are more concentrated in the Baltimore and Washington, D.C. urban regions
716 than this set of ACAM data, which is consistent with the conclusions derived from the ACAM dataset retrieved
717 by Lamsal et al. (2017).

718 The potential distribution bias of the NEI2011 NO_x emissions at 36-km resolution is analyzed by comparing
719 the 36-km REAM simulated NO₂ TVCDs with those retrieved by OMI and GOME-2A, as shown in Figures 15
720 (OMI, 13:00 LT) and S27 (GOME-2A, 9:30 LT). Both KNMI and our retrievals based on the 36-km REAM NO₂
721 vertical profiles show that OMI and GOME-2A NO₂ TVCDs have lower spatial variations than the corresponding
722 36-km REAM simulation results. OMI and GOME-2A retrievals have lower NO₂ TVCDs around the Baltimore
723 and Washington, D.C. urban regions and higher values in relatively rural regions than the 36-km REAM. The
724 distribution bias of the 36-km REAM NO₂ TVCDs is also identified on weekends through their comparison with
725 OMI and GOME-2A retrievals (not shown). The good agreement between simulated and observed wind suggests
726 that the model horizontal transport error cannot explain such an urban-rural contrast between satellite
727 observations and 36-km REAM simulation results. However, two caveats deserve attention. Firstly, the 36-km
728 REAM cannot resolve urban areas as detailed as the 4-km REAM (Figure 14), and urban and rural regions may
729 coexist in one 36-km grid cell. Secondly, the OMI and GOME-2A pixels can be much larger than 36-km REAM
730 grid cells, possibly leading to more spatially homogenous distributions of satellite NO₂ TVCD data.

731 3.87 Implications for NO_x emissions

732 The analysis of section 3.76 indicates that the NEI2011 NO_x emission distributions ~~at the 36- and~~ 4-km
733 resolutions ~~is-are~~ likely biased for the Baltimore-Washington region. The distribution bias of ~~the high-resolution~~
734 NO_x emission inventories is corroborated by the comparison of the NO_x emission inventory derived from the
735 CONSolidated Community Emissions Processor Tool, Motor Vehicle (CONCEPT MV) v2.1 with that estimated
736 by the Sparse Matrix Operator Kernel Emissions (SMOKE) v3.0 model with the Motor Vehicle Emissions
737 Simulator (MOVES) v2010a (DenBleyker et al., 2012). CONCEPT with finer vehicle activity information as
738 input produced a wider-spread but less-concentrated running exhaust NO_x emissions compared to MOVES in the
739 Denver urban area for July 2008 (DenBleyker et al., 2012). In addition, Canty et al. (2015) found that CMAQ
740 4.7.1, with on-road emissions from MOVES and off-road emissions from the National Mobile Inventory Model
741 (NMIM), overestimated NO₂ TVCD over urban regions and underestimated NO₂ TVCDs over rural areas in the
742 northeastern U.S. for July and August 2011 compared to the OMNO2 product. The urban-rural contrast was also
743 found in Texas during the 2013 DISCOVER-AQ campaign in the studies of Souri et al. (2016) and Souri et al.
744 (2018), implying distribution uncertainties in NO_x emissions, although these studies and Canty et al. (2015)
745 focused more on polluted regions with overestimated NO_x emissions in their conclusions. The emission
746 distribution bias may also explain why Anderson et al. (2014) have different results from our simulated
747 concentrations in Table 1. In their study, they compared in-situ observations with a nested CMAQ simulation
748 with a resolution of 1.33 km. It is difficult to build up a reliable emission inventory for the whole U.S. at very
749 high resolutions with currently available datasets due to the significant inhomogeneity of NO_x emissions (Marr et
750 al., 2013), but we can still expect significant improvements of the temporal-spatial distributions of NO_x
751 emissions in the near future as GPS-based information start to be used in the NEI estimates (DenBleyker et al.,
752 2017).

753 Although the NEI2011 NO_x emission distribution is likely biased at 4 km resolution, the similar average
754 below aircraft NO₂ VCDs between ACAM and the 4 km REAM (Figure 10), as well as the good performance of
755 the 36 km REAM compared to NO₂ and NO_y observations (Figures 3 and 5-9 and Table 1), suggest that NEI2011
756 may provide reliable estimates of NO_x emissions over the Baltimore-Washington region at coarser resolutions. It
757 should be noted that although the good performance of the 36 km REAM in reproducing P-3B, Pandora, and
758 surface observations may be limited by representative errors due to the relatively coarse resolution of 36 km
759 REAM, ACAM and satellite NO₂ VCDs are all observations covering large areas, alleviating the problem caused
760 by observations limited to small areas. Our conclusion on the potential reliability of NEI2011 is consistent with
761 Salmon et al. (2018), who found NEI2011 and NEI2014 were in agreement with aircraft observation-derived NO_x
762 emissions during the Wintertime INvestigation of Transport, Emissions, and Reactivity (WINTER) campaign in
763 February—March 2015 around the Washington, D.C. Baltimore area. The agreement was further confirmed
764 through the investigation of observed and NEI NO_x/CO₂, CO/NO_x, and CO/CO₂ ratios (Salmon et al., 2018).
765 However, our evaluation of NEI NO_x emissions is different from Travis et al. (2016) and Anderson et al. (2014).
766 Travis et al. (2016) compared the GEOS-Chem simulation results with the observations of NO_x and its oxidation
767 products from the SEAC⁴RS campaign in the Southeast US, nitrate wet deposition fluxes from the National Acid
768 Deposition Program (NADP) network, and NO₂ TVCDs from OMI, and suggested that NEI2011 overestimated
769 mobile and industrial NO_x emissions by 30%—60%. The GEOS-Chem chemical mechanism from Travis et al.
770 (2016) is almost the same as what we use in REAM, and their model simulation has a horizontal resolution of
771 0.25° × 0.3125°, which is also close to REAM (36 km × 36 km). We attribute the discrepancies between Travis et
772 al. (2016) and our study to the regional discrepancies. Travis et al. (2016) derived their conclusions based on the
773 averages of large domains (the whole CONUS or the Southeast U.S.), while our study focuses on the much
774 smaller Baltimore-Washington region. If limited to the Baltimore-Washington region, Figures 3 and 5 in Travis
775 et al. (2016) shown that nitrate wet deposition fluxes from NADP and TVCDs from the Berkeley High-

776 ~~Resolution (BEHR) retrieval and NASA (OMNO2) were significantly higher than their simulations with NEI~~
777 ~~non-power plant NO_x emissions reduced by 60%, implying their conclusions about the overestimation of NEI~~
778 ~~NO_x emissions at least not applicable to the Baltimore–Washington region. Anderson et al. (2014) evaluated~~
779 ~~NEI2011 emissions with the observed concentration ratios of CO to NO_y and CO to NO_x from the same~~
780 ~~DISCOVER AQ campaign. They concluded that NEI overestimated NO_x emissions by 51%–70% in Maryland~~
781 ~~in the summer of 2011. However, the uncertainties of scaling the emission ratios of CO/NO_x to the concentrations~~
782 ~~ratios of CO/NO_y or CO/NO_x can be large due in part to the large contribution of biogenic isoprene oxidation to~~
783 ~~the variation of CO (Cheng et al., 2017). Furthermore, base CMAQ simulated ΣPNs (1.4 ppbv) and ΣANs (0.96~~
784 ~~ppbv) concentrations by Anderson et al. (2014) are 0.79 and 0.64 ppbv higher than the corresponding P-3B~~
785 ~~observations, respectively, leading to the overestimation of NO_y in their model; these biases are much larger than~~
786 ~~those (–0.2 ppbv) from our 36-km REAM simulation as shown in Table 1, possibly due to different chemical~~
787 ~~mechanisms used by CMAQ and REAM. Another possible reason, as mentioned above, is that the base CMAQ~~
788 ~~used by Anderson et al. (2014) has a horizontal resolution of 1.33 km, much higher than our REAM simulations;~~
789 ~~NO_x emission distribution may be a potential issue causing the overestimation of the base CMAQ results.~~

790 Here, we emphasize that our study is not necessarily contradictory to recent studies concerning the
791 overestimation of NEI NO_x emissions (Anderson et al., 2014; Canty et al., 2015; McDonald et al., 2018; Souri et
792 al., 2016; Souri et al., 2018; Travis et al., 2016). Different types of observations in different periods and locations
793 are analyzed for various purposes. This study focuses more on the spatial distribution of NO_x emissions in
794 NEI2011 ~~at the 4 km resolution~~, while previous studies are concerned more about the NO_x emission magnitudes
795 in highly polluted sites, although the spatial distribution issue was also mentioned in some of the studies. If we
796 limit our analyses to those observations in Figures [75](#), [107](#), and [129](#) and the 4-km REAM, we would also
797 conclude an overestimation of NEI NO_x emissions. ~~In this study, through comprehensive evaluations of NO₂ and~~
798 ~~NO_y measurements at 36- and 4-km resolutions, we provide another possible explanation for the overestimation~~

799 ~~of high-resolution model results at polluted sites. Although our assessment of NEI2011 NO_x emissions at 36-km~~
800 ~~resolution is contingent upon potential representative errors, the further comparisons of below-aircraft NO₂ TVCDs~~
801 ~~between the 4-km REAM and ACAM from Lamsal et al. (2017) suggest that total NO_x emissions seem accurate~~
802 ~~but the emission distribution seems biased in the 4-km NEI2011 in our defined domain (Figure 10).~~ Considering
803 the significant heterogeneity of NO_x emissions, ~~different conclusions on NO_x emission biases may be made in~~
804 ~~other regions, but~~ the spatial distribution of NO_x emissions is a critical factor in evaluating NO_x emissions and
805 improving emission estimation and air quality models, which deserves more attention in future studies, especially
806 when chemical and transport models are moving to higher and higher resolutions.

807 4 Conclusions

808 We investigate the diurnal cycles of surface NO₂ concentrations, NO₂ vertical profiles, and NO₂ TVCDs
809 using REAM model simulations on the basis of the observations from air quality monitoring sites, aircraft,
810 Pandora, OMI, and GOME-2A during the DISCOVER-AQ 2011 campaign. We find that WRF simulated
811 nighttime k_{zz}-determined PBLHs are significantly lower than ELF lidar measurements. Increasing nighttime
812 mixing from 18:00 – 5:00 LT in the REAM simulations, we significantly improve REAM simulations of
813 nighttime surface NO₂ and O₃ concentrations.

814 The REAM simulation reproduces well the observed regional mean diurnal cycles of surface NO₂ and NO_y
815 concentrations, NO₂ vertical profiles, and NO₂ TVCDs on weekdays. Observed NO₂ concentrations in the
816 boundary layer and TVCDs on weekends are significantly lower than on weekdays. By specifying a weekend to
817 weekday NO_x emission ratio of 2:3 and applying a less variable NO_x emission diurnal profile on weekends than
818 weekdays, REAM can simulate well the weekend observations. A few Two issues are also noted. First, Pandora
819 TVCDs show different variations from aircraft-derived and REAM-simulated TVCDs in the early morning and
820 late afternoon, which may be due to the uncertainties of Pandora measurements at large SZAs and the small

821 effective FOV of Pandora. Second, the weekday OMI NO₂ TVCDs derived by NASA are somewhat lower than
822 the KNMI OMI product, P-3B aircraft-derived TVCDs, Pandora, and REAM results; the difference may be
823 caused by the a priori vertical profiles used in the NASA retrieval. ~~Lastly, the weekend OMI NO₂ TVCDs
824 derived by KNMI are larger than those from Pandora, P-3B aircraft, REAM, and the OMI retrieval with REAM
825 NO₂ vertical profiles, indicating a possible bias of the TM4 simulated a priori NO₂ vertical profiles in the
826 weekend mornings during DISCOVER-AQ 2011.~~

827 While a higher-resolution simulation is assumed to be superior a priori, the large observation dataset
828 during DISCOVER-AQ 2011 offers the opportunity of a detailed comparison of 4-km and 36-km model
829 simulations. ~~In general, the 4-km simulation results tend to have a high bias relative to the 36-km results in light of
830 the observations. Through the comparison, w~~We find two areas that have not been widely recognized ~~for high-
831 resolution model simulations.~~ The first is not using convection parameterization in high-resolution WRF
832 simulations since convection can be resolved explicitly and most convection parameterizations are not designed
833 for high-resolution simulations. We find that 4-km WRF tends to overestimate boundary-layer mixing and
834 vertical transport in the late afternoon, leading to a high model bias in simulated NO₂ vertical profiles compared
835 to P-3B aircraft observations. The reasons for this late-afternoon bias in 4-km WRF simulations and model
836 modifications to mitigate this bias need further studies.

837 A second issue is related to the spatial distribution of NO_x emissions in NEI2011. In general, the 4-km
838 simulation results tend to have a high bias relative to the 36-km results on the regional mean observations.
839 However, for individual sites, relative to the 36-km model simulations, the 4-km model results can show larger,
840 smaller, or similar biases compared to the observations depending upon observation location. Based on process
841 diagnostics and analyses, we find that the bias discrepancies between the 36-km and 4-km REAM simulations are
842 mainly attributed to their different NO_x emissions and their spatial gradients at different sites. At 4 km, the grid

843 ~~cells over the 11 inland Pandora sites have 34% higher NO_x emissions than the 36 km grid cells. Consequently,~~
844 ~~4 km REAM overestimates NO₂ concentrations and TVCDs than the observations. The 4 km grid cells over four~~
845 ~~surface NO_y measurement sites have about a factor of 2 higher NO_x emissions than the corresponding 36 km grid~~
846 ~~cells, leading to significantly overestimated NO_y concentrations in the 4 km REAM simulation compared to the~~
847 ~~observations. After we re-grid the 4 km NO₂ and NO_y results to the 36 km grid cells, the results of 4 km~~
848 ~~simulations are similar to the original 36 km simulations.~~ The comparison of 4-km ACAM NO₂ VCD
849 measurements from the UC-12 aircraft with coincident 4-km REAM results shows that 4-km REAM NO₂ VCDs
850 are more concentrated in urban regions than the ACAM observations. OMI and GOME-2A data also show less
851 spatially varying NO₂ TVCD distributions with lower NO₂ TVCDs around the Baltimore-Washington urban
852 regions and higher TVCDs in surrounding rural areas than corresponding 36-km REAM simulation results.
853 Further model analysis indicates that the 36- and 4-km VCD discrepancies are due primarily to the distribution
854 bias of 4-km-NEI2011 NO_x emissions at 36- and 4-km resolutions. At high resolutions, potential biases in the
855 emission inventories are accentuated when model results are evaluated with the observations. Our results
856 highlight the research need to improve the methodologies and datasets used to improve the spatial distributions in
857 emission estimates at high resolutions.

858 **Data availability**

859 The DISCOVER-AQ 2011 campaign datasets are archived on [https://www-air.larc.nasa.gov/cgi-](https://www-air.larc.nasa.gov/cgi-bin/ArcView/discover-aq.dc-2011)
860 [bin/ArcView/discover-aq.dc-2011](https://www-air.larc.nasa.gov/cgi-bin/ArcView/discover-aq.dc-2011) (last access: March 146, 20210). EPA air quality monitoring datasets are from
861 <https://www3.epa.gov/airdata/> (last access: June 23, 2015). The NASA OMI NO₂ product is from
862 https://disc.gsfc.nasa.gov/datasets/OMNO2_003/summary (last access: September 26, 2020). The KNMI OMI
863 NO₂ product is from <http://www.temis.nl/airpollution/no2.html> (last access: January 14, 2015). We obtain the
864 KNMI GOME-2A NO₂ VCD archives from http://www.temis.nl/airpollution/no2col/no2colgome2_v2.php (last
865 access: January 22, 2015). The GMI MERRA-2 simulation results are from

866 <https://portal.nccs.nasa.gov/datashare/dirac/gmidata2/users/mrdamon/Hindcast->
867 [Family/HindcastMR2/2011/stations/](#) (last access: May 14, 2019). We obtain the UC-12 ACAM NO₂ VCD
868 product by X. Liu from <https://www-air.larc.nasa.gov/cgi-bin/ArcView/discover-aq.dc->
869 [2011?UC12=1#LIU.XIONG/](#) (last access: December 31, 2019). The Stage IV precipitation data is downloaded
870 from <https://rda.ucar.edu/datasets/ds507.5/> (last access: December 28, 2019). The NCEP CFSv2 6-hourly product
871 is available at <http://rda.ucar.edu/datasets/ds094.0/> (last access: March 10, 2015). REAM simulation results for
872 this study and the UC-12 ACAM NO₂ VCD product by Lamsal et al. (2017) are available upon request.

873 **Author contribution**

874 JL and YW designed the study. JL, RZ, and CS updated the REAM model. JL conducted model simulations.
875 KFB developed the DOMINO algorithm, CS applied the algorithm to REAM vertical profiles, and JL updated the
876 retrieval algorithm and did the retrieval by using REAM NO₂ vertical profiles. AW, JH, EAC, RWL, JJS, RD,
877 AMT, TNK, LNL, SJJ, MGK, XL, CRN made various measurements in the DISCOVER-AQ 2011 campaign. JL
878 conducted the analyses with discussions with YW, RZ, CS, AW, JH, KFB, EAC, RWL, JJS, RD, AMT, TNK,
879 LNL, SJJ, MGK, XL, and CRN. JL and YW led the writing of the manuscript with inputs from all other
880 coauthors. All coauthors reviewed the manuscript.

881 **Competing interests**

882 The authors declare that they have no conflict of interest.

883 **Acknowledgments**

884 This work was supported by the NASA ACMAP Program. We thank Chun Zhao for providing us the PNNL
885 NEI2011 emission inventory. We thank Yuzhong Zhang and Jenny Fisher for providing the updated GEOS-
886 Chem chemistry mechanism files and thank Yuzhong Zhang, Yongjia Song, Hang Qu, Ye Cheng, Aoxing Zhang,

887 Yufei Zou and Ziming Ke for discussion with J. Li. We thank Susan Strahan for providing the GMI outputs
888 download link.

889 **References**

- 890 Anderson, D. C., Loughner, C. P., Diskin, G., Weinheimer, A., Canty, T. P., Salawitch, R. J., Worden, H. M.,
891 Fried, A., Mikoviny, T., and Wisthaler, A.: Measured and modeled CO and NO_y in DISCOVER-AQ: An
892 evaluation of emissions and chemistry over the eastern US, *Atmos. Environ.*, 96, 78-87,
893 <https://doi.org/10.1016/j.atmosenv.2014.07.004>, 2014.
- 894 Beirle, S., Platt, U., Wenig, M., and Wagner, T.: Weekly cycle of NO₂ by GOME measurements: A signature of
895 anthropogenic sources, *Atmos. Chem. Phys.*, 3, 2225-2232, <https://doi.org/10.5194/acp-3-2225-2003>, 2003.
- 896 Boersma, K. F., Eskes, H. J., Veeffkind, J. P., Brinksma, E. J., Van Der A, R. J., Sneep, M., Van Den Oord, G. H.
897 J., Levelt, P. F., Stammes, P., and Gleason, J. F.: Near-real time retrieval of tropospheric NO₂ from OMI, *Atmos.*
898 *Chem. Phys.*, 7, 2103-2118, <https://doi.org/10.5194/acp-7-2103-2007>, 2007.
- 899 Boersma, K. F., Jacob, D. J., Eskes, H. J., Pinder, R. W., Wang, J., and Van Der A, R. J.: Intercomparison of
900 SCIAMACHY and OMI tropospheric NO₂ columns: Observing the diurnal evolution of chemistry and emissions
901 from space, *J. Geophys. Res.-Atmos.*, 113, <https://doi.org/10.1029/2007JD008816>, 2008.
- 902 Boersma, K. F., Jacob, D. J., Trainic, M., Rudich, Y., De Smedt, I., Dirksen, R., and Eskes, H. J.: Validation of
903 urban NO₂ concentrations and their diurnal and seasonal variations observed from the SCIAMACHY and OMI
904 sensors using in situ surface measurements in Israeli cities, *Atmos. Chem. Phys.*, 9, 3867-3879,
905 <https://doi.org/10.5194/acp-9-3867-2009>, 2009.
- 906 Boersma, K. F., Eskes, H. J., Dirksen, R. J., Veeffkind, J. P., Stammes, P., Huijnen, V., Kleipool, Q. L., Sneep,
907 M., Claas, J., and Leitão, J.: An improved tropospheric NO₂ column retrieval algorithm for the Ozone Monitoring
908 Instrument, *Atmos. Meas. Tech.*, 4, 1905-1928, <https://doi.org/10.5194/amt-4-1905-2011>, 2011.
- 909 Boersma, K. F., Eskes, H. J., Richter, A., De Smedt, I., Lorente, A., Beirle, S., van Geffen, J. H., Zara, M., Peters,
910 E., and Roozendaal, M. V.: Improving algorithms and uncertainty estimates for satellite NO₂ retrievals: results
911 from the quality assurance for the essential climate variables (QA4ECV) project, *Atmos. Meas. Tech.*, 11, 6651-
912 6678, <https://doi.org/10.5194/amt-11-6651-2018>, 2018.
- 913 Breuer, H., Ács, F., Horváth, Á., Németh, P., and Rajkai, K.: Diurnal course analysis of the WRF-simulated and
914 observation-based planetary boundary layer height, *Advances in Science and Research*, 11, 83-88,
915 <https://doi.org/10.5194/asr-11-83-2014>, 2014.
- 916 Brohede, S., McLinden, C. A., Berthet, G., Haley, C. S., Murtagh, D., and Sioris, C. E.: A stratospheric NO₂
917 climatology from Odin/OSIRIS limb-scatter measurements, *Can. J. Phys.*, 85, 1253-1274,
918 <https://doi.org/10.1139/p07-141>, 2007.

- 919 Brown, S. S., Dibb, J. E., Stark, H., Aldener, M., Vozella, M., Whitlow, S., Williams, E. J., Lerner, B. M.,
920 Jakoubek, R., and Middlebrook, A. M.: Nighttime removal of NO_x in the summer marine boundary layer,
921 *Geophys. Res. Lett.*, 31, <https://doi.org/10.1029/2004GL019412>, 2004.
- 922 Bucselá, E. J., Krotkov, N. A., Celarier, E. A., Lamsal, L. N., Swartz, W. H., Bhartia, P. K., Boersma, K. F.,
923 Veefkind, J. P., Gleason, J. F., and Pickering, K. E.: A new stratospheric and tropospheric NO₂ retrieval
924 algorithm for nadir-viewing satellite instruments: applications to OMI, *Atmos. Meas. Tech.*, 6, 2607-2626,
925 <https://doi.org/10.5194/amt-6-2607-2013>, 2013.
- 926 Canty, T., Hemberck, L., Vinciguerra, T., Goldberg, D., Carpenter, S., Allen, D., Loughner, C., Salawitch, R., and
927 Dickerson, R.: Ozone and NO_x chemistry in the eastern US: evaluation of CMAQ/CB05 with satellite (OMI)
928 data, *Atmos. Chem. Phys.*, 15, 10965, <https://doi.org/10.5194/acp-15-10965-2015>, 2015.
- 929 Chance, K.: OMI Algorithm Theoretical Basis Document: OMI Trace Gas Algorithms, available at
930 <https://ozoneaq.gsfc.nasa.gov/media/docs/ATBD-OMI-04.pdf>, Smithsonian Astrophysical Observatory,
931 Cambridge, MA, USA2.0, 78, 2002.
- 932 Cheng, Y., Wang, Y., Zhang, Y., Chen, G., Crawford, J. H., Kleb, M. M., Diskin, G. S., and Weinheimer, A. J.:
933 Large biogenic contribution to boundary layer O₃-CO regression slope in summer, *Geophys. Res. Lett.*, 44, 7061-
934 7068, <https://doi.org/10.1002/2017GL074405>, 2017.
- 935 Cheng, Y., Wang, Y., Zhang, Y., Crawford, J. H., Diskin, G. S., Weinheimer, A. J., and Fried, A.: Estimator of
936 surface ozone using formaldehyde and carbon monoxide concentrations over the eastern United States in
937 summer, *J. Geophys. Res.-Atmos.*, 123, 7642-7655, <https://doi.org/10.1029/2018JD028452>, 2018.
- 938 Choi, S., Lamsal, L. N., Follette-Cook, M., Joiner, J., Krotkov, N. A., Swartz, W. H., Pickering, K. E., Loughner,
939 C. P., Appel, W., Pfister, G., Saide, P. E., Cohen, R. C., Weinheimer, A. J., and Herman, J. R.: Assessment of
940 NO₂ observations during DISCOVER-AQ and KORUS-AQ field campaigns, *Atmos. Meas. Tech.*, 13, 2523-
941 2546, <https://doi.org/10.5194/amt-13-2523-2020>, 2020.
- 942 Choi, Y., Wang, Y., Zeng, T., Cunnold, D., Yang, E. S., Martin, R., Chance, K., Thouret, V., and Edgerton, E.:
943 Springtime transitions of NO₂, CO, and O₃ over North America: Model evaluation and analysis, *J. Geophys.*
944 *Res.-Atmos.*, 113, <https://doi.org/10.1029/2007JD009632>, 2008.
- 945 Choi, Y., Kim, H., Tong, D., and Lee, P.: Summertime weekly cycles of observed and modeled NO_x and O₃
946 concentrations as a function of satellite-derived ozone production sensitivity and land use types over the
947 Continental United States, *Atmos. Chem. Phys.*, 12, 6291-6307, <https://doi.org/10.5194/acp-12-6291-2012>, 2012.
- 948 Compton, J. C., Delgado, R., Berkoff, T. A., and Hoff, R. M.: Determination of planetary boundary layer height
949 on short spatial and temporal scales: A demonstration of the covariance wavelet transform in ground-based wind
950 profiler and lidar measurements, *Journal of Atmospheric and Oceanic Technology*, 30, 1566-1575,
951 <https://doi.org/10.1175/JTECH-D-12-00116.1>, 2013.

952 David, L. M., and Nair, P. R.: Diurnal and seasonal variability of surface ozone and NO_x at a tropical coastal site:
953 Association with mesoscale and synoptic meteorological conditions, *J. Geophys. Res.-Atmos.*, 116,
954 <https://doi.org/10.1029/2010JD015076>, 2011.

955 Davis, C., Brown, B., and Bullock, R.: Object-based verification of precipitation forecasts. Part I: Methodology
956 and application to mesoscale rain areas, *Monthly Weather Review*, 134, 1772-1784,
957 <https://doi.org/10.1175/MWR3145.1>, 2006.

958 Day, D. A., Wooldridge, P. J., Dillon, M. B., Thornton, J. A., and Cohen, R. C.: A thermal dissociation laser -
959 induced fluorescence instrument for in situ detection of NO₂, peroxy nitrates, alkyl nitrates, and HNO₃, *J.*
960 *Geophys. Res.-Atmos.*, 107, ACH 4-1-ACH 4-14, <https://doi.org/10.1029/2001JD000779>, 2002.

961 de Foy, B.: City-level variations in NO_x emissions derived from hourly monitoring data in Chicago, *Atmos.*
962 *Environ.*, 176, 128-139, <https://doi.org/10.1016/j.atmosenv.2017.12.028>, 2018.

963 DenBleyker, A., Morris, R. E., Lindhjem, C. E., Parker, L. K., Shah, T., Koo, B., Loomis, C., and Dilly, J.:
964 Temporal and Spatial Detail in Mobile Source Emission Inventories for Regional Air Quality Modeling, 2012
965 International Emission Inventory Conference, Florida, U.S., August 13 - 16, 2012, 2012.

966 DenBleyker, A., Koupal, J., DeFries, T., and Palacios, C.: Improvement of Default Inputs for MOVES and
967 SMOKE-MOVES: CRC Project A-100, available at [https://crcao.org/reports/recentstudies2017/A-](https://crcao.org/reports/recentstudies2017/A-100/ERG_FinalReport_CRCA100_28Feb2017.pdf)
968 [100/ERG_FinalReport_CRCA100_28Feb2017.pdf](https://crcao.org/reports/recentstudies2017/A-100/ERG_FinalReport_CRCA100_28Feb2017.pdf), Eastern Research Group, Inc., Austin, TX, 86, 2017.

969 Dirksen, R. J., Boersma, K. F., Eskes, H. J., Ionov, D. V., Bucsele, E. J., Levelt, P. F., and Kelder, H. M.:
970 Evaluation of stratospheric NO₂ retrieved from the Ozone Monitoring Instrument: Intercomparison, diurnal cycle,
971 and trending, *J. Geophys. Res.-Atmos.*, 116, <https://doi.org/10.1029/2010JD014943>, 2011.

972 EPA: Profile of the 2011 National Air Emissions Inventory, available at
973 https://www.epa.gov/sites/production/files/2015-08/documents/lite_finalversion_ver10.pdf, U.S. Environmental
974 Protection Agency, 2014.

975 Fisher, J. A., Jacob, D. J., Travis, K. R., Kim, P. S., Marais, E. A., Chan Miller, C., Yu, K., Zhu, L., Yantosca, R.
976 M., and Sulprizio, M. P.: Organic nitrate chemistry and its implications for nitrogen budgets in an isoprene-and
977 monoterpene-rich atmosphere: constraints from aircraft (SEAC⁴RS) and ground-based (SOAS) observations in
978 the Southeast US, *Atmos. Chem. Phys.*, 16, 5969-5991, <https://doi.org/10.5194/acp-16-5969-2016>, 2016.

979 Flynn, C. M., Pickering, K. E., Crawford, J. H., Lamsal, L., Krotkov, N., Herman, J., Weinheimer, A., Chen, G.,
980 Liu, X., and Szykman, J.: Relationship between column-density and surface mixing ratio: Statistical analysis of
981 O₃ and NO₂ data from the July 2011 Maryland DISCOVER-AQ mission, *Atmos. Environ.*, 92, 429-441,
982 <https://doi.org/10.1016/j.atmosenv.2014.04.041>, 2014.

983 Frey, M. M., Brough, N., France, J. L., Anderson, P. S., Traulle, O., King, M. D., Jones, A. E., Wolff, E. W., and
984 Savarino, J.: The diurnal variability of atmospheric nitrogen oxides (NO and NO₂) above the Antarctic Plateau
985 driven by atmospheric stability and snow emissions, *Atmos. Chem. Phys.*, 13, 3045-3062,
986 <https://doi.org/10.5194/acp-13-3045-2013>, 2013.

- 987 Gaur, A., Tripathi, S. N., Kanawade, V. P., Tare, V., and Shukla, S. P.: Four-year measurements of trace gases
988 (SO₂, NO_x, CO, and O₃) at an urban location, Kanpur, in Northern India, *Journal of Atmospheric Chemistry*, 71,
989 283-301, <https://doi.org/10.1007/s10874-014-9295-8>, 2014.
- 990 Gourley, J. J., Hong, Y., Flamig, Z. L., Wang, J., Vergara, H., and Anagnostou, E. N.: Hydrologic evaluation of
991 rainfall estimates from radar, satellite, gauge, and combinations on Ft. Cobb basin, Oklahoma, *Journal of*
992 *Hydrometeorology*, 12, 973-988, <https://doi.org/10.1175/2011JHM1287.1>, 2011.
- 993 Guenther, A. B., Jiang, X., Heald, C. L., Sakulyanontvittaya, T., Duhl, T., Emmons, L. K., and Wang, X.: The
994 Model of Emissions of Gases and Aerosols from Nature version 2.1 (MEGAN2.1): an extended and updated
995 framework for modeling biogenic emissions, *Geosci. Model Dev.*, 5, 1471-1492, [https://doi.org/10.5194/gmd-5-](https://doi.org/10.5194/gmd-5-1471-2012)
996 1471-2012, 2012.
- 997 Hains, J. C., Boersma, K. F., Kroon, M., Dirksen, R. J., Cohen, R. C., Perring, A. E., Bucsele, E., Volten, H.,
998 Swart, D. P. J., and Richter, A.: Testing and improving OMI DOMINO tropospheric NO₂ using observations
999 from the DANDELIONS and INTEX - B validation campaigns, *J. Geophys. Res.-Atmos.*, 115,
1000 <https://doi.org/10.1029/2009JD012399>, 2010.
- 1001 Herman, J., Cede, A., Spinei, E., Mount, G., Tzortziou, M., and Abuhassan, N.: NO₂ column amounts from
1002 ground-based Pandora and MFDOAS spectrometers using the direct-Sun DOAS technique: Intercomparisons and
1003 application to OMI validation, *J. Geophys. Res.-Atmos.*, 114, <https://doi.org/10.1029/2009JD011848>, 2009.
- 1004 Herman, J., Spinei, E., Fried, A., Kim, J., Kim, J., Kim, W., Cede, A., Abuhassan, N., and Segal-Rozenhaimer,
1005 M.: NO₂ and HCHO measurements in Korea from 2012 to 2016 from Pandora spectrometer instruments
1006 compared with OMI retrievals and with aircraft measurements during the KORUS-AQ campaign, *Atmos. Meas.*
1007 *Tech.*, 11, 4583-4603, <https://doi.org/10.5194/amt-11-4583-2018>, 2018.
- 1008 Herman, J., Abuhassan, N., Kim, J., Kim, J., Dubey, M., Raponi, M., and Tzortziou, M.: Underestimation of
1009 column NO₂ amounts from the OMI satellite compared to diurnally varying ground-based retrievals from
1010 multiple PANDORA spectrometer instruments, *Atmos. Meas. Tech.*, 12, 5593-5612, [https://doi.org/10.5194/amt-](https://doi.org/10.5194/amt-12-5593-2019)
1011 12-5593-2019, 2019.
- 1012 [Hong, S.-Y., Noh, Y., and Dudhia, J.: A new vertical diffusion package with an explicit treatment of entrainment](https://doi.org/10.1175/MWR3199.1)
1013 [processes, *Monthly weather review*, 134, 2318-2341, <https://doi.org/10.1175/MWR3199.1>, 2006.](https://doi.org/10.1175/MWR3199.1)
- 1014 Hu, X., Doughty, D. C., Sanchez, K. J., Joseph, E., and Fuentes, J. D.: Ozone variability in the atmospheric
1015 boundary layer in Maryland and its implications for vertical transport model, *Atmos. Environ.*, 46, 354-364,
1016 <https://doi.org/10.1016/j.atmosenv.2011.09.054>, 2012.
- 1017 Huijnen, V., Eskes, H. J., Poupkou, A., Elbern, H., Boersma, K. F., Foret, G., Sofiev, M., Valdebenito, A.,
1018 Flemming, J., and Stein, O.: Comparison of OMI NO₂ tropospheric columns with an ensemble of global and
1019 European regional air quality models, *Atmos. Chem. Phys.*, 10, 3273-3296, [https://doi.org/10.5194/acp-10-3273-](https://doi.org/10.5194/acp-10-3273-2010)
1020 2010, 2010.

- 1021 Ionov, D. V., Timofeyev, Y. M., Sinyakov, V. P., Semenov, V. K., Goutail, F., Pommereau, J. P., Bucsela, E. J.,
1022 Celarier, E. A., and Kroon, M.: Ground - based validation of EOS - Aura OMI NO₂ vertical column data in the
1023 midlatitude mountain ranges of Tien Shan (Kyrgyzstan) and Alps (France), *J. Geophys. Res.-Atmos.*, 113,
1024 <https://doi.org/10.1029/2007JD008659>, 2008.
- 1025 Irie, H., Kanaya, Y., Akimoto, H., Tanimoto, H., Wang, Z., Gleason, J. F., and Bucsela, E. J.: Validation of OMI
1026 tropospheric NO₂ column data using MAX-DOAS measurements deep inside the North China Plain in June
1027 2006: Mount Tai Experiment 2006, *Atmos. Chem. Phys.*, 8, 6577-6586, <https://doi.org/10.5194/acp-8-6577-2008>,
1028 2008.
- 1029 Irie, H., Boersma, K. F., Kanaya, Y., Takashima, H., Pan, X., and Wang, Z.: Quantitative bias estimates for
1030 tropospheric NO₂ columns retrieved from SCIAMACHY, OMI, and GOME-2 using a common standard for East
1031 Asia, *Atmos. Meas. Tech.*, 5, 2403-2411, <https://doi.org/10.5194/amt-5-2403-2012>, 2012.
- 1032 Jones, A. E., Weller, R., Wolff, E. W., and Jacobi, H. W.: Speciation and rate of photochemical NO and NO₂
1033 production in Antarctic snow, *Geophys. Res. Lett.*, 27, 345-348, <https://doi.org/10.1029/1999GL010885>, 2000.
- 1034 Judd, L. M., Al-Saadi, J. A., Valin, L. C., Pierce, R. B., Yang, K., Janz, S. J., Kowalewski, M. G., Szykman, J. J.,
1035 Tiefengraber, M., and Mueller, M.: The Dawn of Geostationary Air Quality Monitoring: Case Studies from Seoul
1036 and Los Angeles, *Front. Environ. Sci.*, 6, 85, <https://doi.org/10.3389/fenvs.2018.00085>, 2018.
- 1037 Judd, L. M., Al-Saadi, J. A., Janz, S. J., Kowalewski, M. G., Pierce, R. B., Szykman, J. J., Valin, L. C., Swap, R.,
1038 Cede, A., Mueller, M., Tiefengraber, M., Abuhassan, N., and Williams, D.: Evaluating the impact of spatial
1039 resolution on tropospheric NO₂ column comparisons within urban areas using high-resolution airborne data,
1040 *Atmos. Meas. Tech.*, 12, 6091-6111, <https://doi.org/10.5194/amt-12-6091-2019>, 2019.
- 1041 Judd, L. M., Al-Saadi, J. A., Szykman, J. J., Valin, L. C., Janz, S. J., Kowalewski, M. G., Eskes, H. J., Veeffkind,
1042 J. P., Cede, A., Mueller, M., Gebetsberger, M., Swap, R., Pierce, R. B., Nowlan, C. R., Abad, G. G., Nehrir, A.,
1043 and Williams, D.: Evaluating Sentinel-5P TROPOMI tropospheric NO₂ column densities with airborne and
1044 Pandora spectrometers near New York City and Long Island Sound, *Atmos. Meas. Tech. Discuss.*, 2020, 1-52,
1045 <https://doi.org/10.5194/amt-2020-151>, 2020.
- 1046 Kalinga, O. A., and Gan, T. Y.: Estimation of rainfall from infrared - microwave satellite data for basin - scale
1047 hydrologic modelling, *Hydrological processes*, 24, 2068-2086, <https://doi.org/10.1002/hyp.7626>, 2010.
- 1048 Kaynak, B., Hu, Y., Martin, R. V., Sioris, C. E., and Russell, A. G.: Comparison of weekly cycle of NO₂ satellite
1049 retrievals and NO_x emission inventories for the continental United States, *J. Geophys. Res.-Atmos.*, 114,
1050 <https://doi.org/10.1029/2008JD010714>, 2009.
- 1051 Kim, S. W., McDonald, B., Baidar, S., Brown, S., Dube, B., Ferrare, R., Frost, G., Harley, R., Holloway, J., and
1052 Lee, H. J.: Modeling the weekly cycle of NO_x and CO emissions and their impacts on O₃ in the Los Angeles-
1053 South Coast Air Basin during the CalNex 2010 field campaign, *J. Geophys. Res.-Atmos.*, 121, 1340-1360,
1054 <https://doi.org/10.1002/2015JD024292>, 2016.

- 1055 Knepp, T., Pippin, M., Crawford, J., Chen, G., Szykman, J., Long, R., Cowen, L., Cede, A., Abuhassan, N., and
1056 Herman, J.: Estimating surface NO₂ and SO₂ mixing ratios from fast-response total column observations and
1057 potential application to geostationary missions, *Journal of atmospheric chemistry*, 72, 261-286,
1058 <https://doi.org/10.1007/s10874-013-9257-6>, 2015.
- 1059 [Kollonige, D. E., Thompson, A. M., Josipovic, M., Tzortziou, M., Beukes, J. P., Burger, R., Martins, D. K., van](#)
1060 [Zyl, P. G., Vakkari, V., and Laakso, L.: OMI Satellite and Ground - Based Pandora Observations and Their](#)
1061 [Application to Surface NO₂ Estimations at Terrestrial and Marine Sites, *J. Geophys. Res.-Atmos.*, 123, 1441-](#)
1062 [1459, <https://doi.org/10.1002/2017JD026518>, 2018.](#)
- 1063 Krotkov, N. A., Lamsal, L. N., Celarier, E. A., Swartz, W. H., Marchenko, S. V., Bucsela, E. J., Chan, K. L.,
1064 Wenig, M., and Zara, M.: The version 3 OMI NO₂ standard product, *Atmos. Meas. Tech.*, 10, 3133-3149,
1065 <https://doi.org/10.5194/amt-10-3133-2017>, 2017.
- 1066 Lamsal, L. N., Krotkov, N. A., Celarier, E. A., Swartz, W. H., Pickering, K. E., Bucsela, E. J., Gleason, J. F.,
1067 Martin, R. V., Philip, S., and Irie, H.: Evaluation of OMI operational standard NO₂ column retrievals using in situ
1068 and surface-based NO₂ observations, *Atmos. Chem. Phys.*, 14, 11587-11609, [https://doi.org/10.5194/acp-14-](https://doi.org/10.5194/acp-14-11587-2014)
1069 [11587-2014](https://doi.org/10.5194/acp-14-11587-2014), 2014.
- 1070 Lamsal, L. N., Duncan, B. N., Yoshida, Y., Krotkov, N. A., Pickering, K. E., Streets, D. G., and Lu, Z.: US NO₂
1071 trends (2005–2013): EPA Air Quality System (AQS) data versus improved observations from the Ozone
1072 Monitoring Instrument (OMI), *Atmos. Environ.*, 110, 130-143, <https://doi.org/10.1016/j.atmosenv.2015.03.055>,
1073 2015.
- 1074 Lamsal, L. N., Janz, S. J., Krotkov, N. A., Pickering, K. E., Spurr, R. J. D., Kowalewski, M. G., Loughner, C. P.,
1075 Crawford, J. H., Swartz, W. H., and Herman, J.: High - resolution NO₂ observations from the Airborne Compact
1076 Atmospheric Mapper: Retrieval and validation, *J. Geophys. Res.-Atmos.*, 122, 1953-1970,
1077 <https://doi.org/10.1002/2016JD025483>, 2017.
- 1078 Lamsal, L. N., Krotkov, N. A., Vasilkov, A., Marchenko, S., Qin, W., Yang, E. S., Fasnacht, Z., Joiner, J., Choi,
1079 S., Haffner, D., Swartz, W. H., Fisher, B., and Bucsela, E.: OMI/Aura Nitrogen Dioxide Standard Product with
1080 Improved Surface and Cloud Treatments, *Atmos. Meas. Tech. Discuss.*, 2020, 1-56, [https://doi.org/10.5194/amt-](https://doi.org/10.5194/amt-2020-200)
1081 [2020-200](https://doi.org/10.5194/amt-2020-200), 2020.
- 1082 Levelt, P. F., Hilsenrath, E., Leppelmeier, G. W., van den Oord, G. H. J., Bhartia, P. K., Tamminen, J., de Haan,
1083 J. F., and Veefkind, J. P.: Science objectives of the ozone monitoring instrument, *IEEE Transactions on*
1084 *Geoscience and Remote Sensing*, 44, 1199-1208, <https://doi.org/10.1109/TGRS.2006.872336>, 2006.
- 1085 Li, J., Wang, Y., and Qu, H.: Dependence of summertime surface ozone on NO_x and VOC emissions over the
1086 United States: Peak time and value, *Geophys. Res. Lett.*, 46, 3540-3550, <https://doi.org/10.1029/2018GL081823>,
1087 2019.
- 1088 [Li, J., Feng, Z., Qian, Y., and Leung, L. R.: A high-resolution unified observational data product of mesoscale](#)
1089 [convective systems and isolated deep convection in the United States for 2004–2017, *Earth Syst. Sci. Data*](#)
1090 [*Discuss.*, 2020, 1–48, <https://doi.org/10.5194/essd-2020-151>, 2020.](#)

- 1091 Lin, Y., and Mitchell, K. E.: the NCEP stage II/IV hourly precipitation analyses: Development and applications,
1092 19th Conf. Hydrology, American Meteorological Society, San Diego, CA, USA, 2005,
- 1093 Liu, C., Liu, X., Kowalewski, M., Janz, S., González Abad, G., Pickering, K., Chance, K., and Lamsal, L.:
1094 Analysis of ACAM data for trace gas retrievals during the 2011 DISCOVER-AQ campaign, *Journal of*
1095 *Spectroscopy*, 2015, <https://doi.org/10.1155/2015/827160>, 2015a.
- 1096 Liu, C., Liu, X., Kowalewski, M. G., Janz, S. J., González Abad, G., Pickering, K. E., Chance, K., and Lamsal, L.
1097 N.: Characterization and verification of ACAM slit functions for trace-gas retrievals during the 2011
1098 DISCOVER-AQ flight campaign, *Atmos. Meas. Tech.*, 8, 751-759, <https://doi.org/10.5194/amt-8-751-2015>,
1099 2015b.
- 1100 Liu, Z., Wang, Y., Gu, D., Zhao, C., Huey, L. G., Stickel, R., Liao, J., Shao, M., Zhu, T., and Zeng, L.:
1101 Summertime photochemistry during CAREBeijing-2007: RO_x budgets and O₃ formation, *Atmos. Chem. Phys.*,
1102 12, 7737-7752, <https://doi.org/10.5194/acp-12-7737-2012>, 2012.
- 1103 Lopez, P.: Direct 4D-Var assimilation of NCEP stage IV radar and gauge precipitation data at ECMWF, *Monthly*
1104 *Weather Review*, 139, 2098-2116, <https://doi.org/10.1175/2010MWR3565.1>, 2011.
- 1105 Luo, G., Yu, F., and Schwab, J.: Revised treatment of wet scavenging processes dramatically improves GEOS-
1106 Chem 12.0.0 simulations of surface nitric acid, nitrate, and ammonium over the United States, *Geosci. Model*
1107 *Dev.*, 12, 3439-3447, <https://doi.org/10.5194/gmd-12-3439-2019>, 2019.
- 1108 Marchenko, S., Krotkov, N., Lamsal, L., Celarier, E., Swartz, W., and Bucsela, E.: Revising the slant column
1109 density retrieval of nitrogen dioxide observed by the Ozone Monitoring Instrument, *J. Geophys. Res.-Atmos.*,
1110 120, 5670-5692, <https://doi.org/10.1002/2014JD022913>, 2015.
- 1111 Marr, L. C., Moore, T. O., Klapmeyer, M. E., and Killar, M. B.: Comparison of NO_x Fluxes Measured by Eddy
1112 Covariance to Emission Inventories and Land Use, *Environ. Sci. Technol.*, 47, 1800-1808,
1113 <https://doi.org/10.1021/es303150y>, 2013.
- 1114 McDonald, B., McKeen, S., Cui, Y. Y., Ahmadov, R., Kim, S.-W., Frost, G. J., Pollack, I., Peischl, J., Ryerson,
1115 T. B., and Holloway, J.: Modeling Ozone in the Eastern US using a Fuel-Based Mobile Source Emissions
1116 Inventory, *Environ. Sci. Technol.*, <https://doi.org/10.1021/acs.est.8b00778>, 2018.
- 1117 Munro, R., Eisinger, M., Anderson, C., Callies, J., Corpaccioli, E., Lang, R., Lefebvre, A., Livschitz, Y., and
1118 Albinana, A. P.: GOME-2 on MetOp, *Proc. of The 2006 EUMETSAT Meteorological Satellite Conference*,
1119 Helsinki, Finland, 2006, 48,
- 1120 Nelson, B. R., Prat, O. P., Seo, D.-J., and Habib, E.: Assessment and implications of NCEP Stage IV quantitative
1121 precipitation estimates for product intercomparisons, *Weather and Forecasting*, 31, 371-394,
1122 <https://doi.org/10.1175/WAF-D-14-00112.1>, 2016.

- 1123 Ng, N. L., Brown, S. S., Archibald, A. T., Atlas, E., Cohen, R. C., Crowley, J. N., Day, D. A., Donahue, N. M.,
1124 Fry, J. L., and Fuchs, H.: Nitrate radicals and biogenic volatile organic compounds: oxidation, mechanisms, and
1125 organic aerosol, *Atmos. Chem. Phys.*, 17, 2103-2162, <https://doi.org/10.5194/acp-17-2103-2017>, 2017.
- 1126 Nowlan, C. R., Liu, X., Leitch, J. W., Chance, K., González Abad, G., Liu, C., Zoogman, P., Cole, J., Delker, T.,
1127 Good, W., Murcray, F., Ruppert, L., Soo, D., Follette-Cook, M. B., Janz, S. J., Kowalewski, M. G., Loughner, C.
1128 P., Pickering, K. E., Herman, J. R., Beaver, M. R., Long, R. W., Szykman, J. J., Judd, L. M., Kelley, P., Luke, W.
1129 T., Ren, X., and Al-Saadi, J. A.: Nitrogen dioxide observations from the Geostationary Trace gas and Aerosol
1130 Sensor Optimization (GeoTASO) airborne instrument: Retrieval algorithm and measurements during
1131 DISCOVER-AQ Texas 2013, *Atmos. Meas. Tech.*, 9, 2647-2668, <https://doi.org/10.5194/amt-9-2647-2016>,
1132 2016.
- 1133 Nowlan, C. R., Liu, X., Janz, S. J., Kowalewski, M. G., Chance, K., Follette-Cook, M. B., Fried, A., González
1134 Abad, G., Herman, J. R., Judd, L. M., Kwon, H. A., Loughner, C. P., Pickering, K. E., Richter, D., Spinei, E.,
1135 Walega, J., Weibring, P., and Weinheimer, A. J.: Nitrogen dioxide and formaldehyde measurements from the
1136 GEOstationary Coastal and Air Pollution Events (GEO-CAPE) Airborne Simulator over Houston, Texas, *Atmos.*
1137 *Meas. Tech.*, 11, 5941-5964, <https://doi.org/10.5194/amt-11-5941-2018>, 2018.
- 1138 Oetjen, H., Baidar, S., Krotkov, N. A., Lamsal, L. N., Lechner, M., and Volkamer, R.: Airborne MAX-DOAS
1139 measurements over California: Testing the NASA OMI tropospheric NO₂ product, *J. Geophys. Res.-Atmos.*, 118,
1140 7400-7413, <https://doi.org/10.1002/jgrd.50550>, 2013.
- 1141 Peng, J., Hu, M., Guo, S., Du, Z., Zheng, J., Shang, D., Zamora, M. L., Zeng, L., Shao, M., and Wu, Y.-S.:
1142 Markedly enhanced absorption and direct radiative forcing of black carbon under polluted urban environments,
1143 *Proc. Natl. Acad. Sci. U.S.A.*, 201602310, <https://doi.org/10.1073/pnas.1602310113>, 2016.
- 1144 Peters, E., Wittrock, F., Großmann, K., Frieß, U., Richter, A., and Burrows, J. P.: Formaldehyde and nitrogen
1145 dioxide over the remote western Pacific Ocean: SCIAMACHY and GOME-2 validation using ship-based MAX-
1146 DOAS observations, *Atmos. Chem. Phys.*, 12, 11179-11197, <https://doi.org/10.5194/acp-12-11179-2012>, 2012.
- 1147 Reddy, B. S. K., Kumar, K. R., Balakrishnaiah, G., Gopal, K. R., Reddy, R. R., Sivakumar, V., Lingaswamy, A.
1148 P., Arafath, S. M., Umadevi, K., and Kumari, S. P.: Analysis of diurnal and seasonal behavior of surface ozone
1149 and its precursors (NO_x) at a semi-arid rural site in Southern India, *Aerosol Air Qual Res*, 12, 1081-1094,
1150 <https://doi.org/10.4209/aaqr.2012.03.0055> 2012.
- 1151 Reed, A. J., Thompson, A. M., Kollonige, D. E., Martins, D. K., Tzortziou, M. A., Herman, J. R., Berkoff, T. A.,
1152 Abuhassan, N. K., and Cede, A.: Effects of local meteorology and aerosols on ozone and nitrogen dioxide
1153 retrievals from OMI and Pandora spectrometers in Maryland, USA during DISCOVER-AQ 2011, *Journal of*
1154 *atmospheric chemistry*, 72, 455-482, <https://doi.org/10.1007/s10874-013-9254-9>, 2015.
- 1155 Reed, C., Evans, M. J., Carlo, P. D., Lee, J. D., and Carpenter, L. J.: Interferences in photolytic NO₂
1156 measurements: explanation for an apparent missing oxidant?, *Atmos. Chem. Phys.*, 16, 4707-4724,
1157 <https://doi.org/10.5194/acp-16-4707-2016>, 2016.

- 1158 Richter, A., Begoin, M., Hilboll, A., and Burrows, J. P.: An improved NO₂ retrieval for the GOME-2 satellite
1159 instrument, *Atmos. Meas. Tech.*, 4, 1147-1159, <https://doi.org/10.5194/amt-4-1147-2011>, 2011.
- 1160 Russell, A. R., Valin, L. C., and Cohen, R. C.: Trends in OMI NO₂ observations over the United States: effects of
1161 emission control technology and the economic recession, *Atmos. Chem. Phys.*, 12, 12197-12209,
1162 <https://doi.org/10.5194/acp-12-12197-2012>, 2012.
- 1163 Saha, S., Moorthi, S., Wu, X., Wang, J., Nadiga, S., Tripp, P., Behringer, D., Hou, Y. T., Chuang, H.-y., and
1164 Iredell, M.: NCEP climate forecast system version 2 (CFSv2) 6-hourly products, available at
1165 <https://rda.ucar.edu/datasets/ds094.0/>, <https://doi.org/10.5065/D61C1TXF>, 2011 (last access: Mar 10, 2015).
- ~~1166 Salmon, O., Shepson, P., Ren, X., He, H., Hall, D., Dickerson, R., Stirm, B., Brown, S., Fibiger, D., and
1167 McDuffie, E.: Top - down Estimates of NO_x and CO Emissions from Washington, DC - Baltimore During the
1168 WINTER Campaign, *J. Geophys. Res.-Atmos.*, <https://doi.org/10.1029/2018JD028539>, 2018.~~
- 1169 Sawamura, P., Müller, D., Hoff, R. M., Hostetler, C. A., Ferrare, R. A., Hair, J. W., Rogers, R. R., Anderson, B.
1170 E., Ziemba, L. D., and Beyersdorf, A. J.: Aerosol optical and microphysical retrievals from a hybrid
1171 multiwavelength lidar data set–DISCOVER-AQ 2011, *Atmos. Meas. Tech.*, 7, 3095-3112,
1172 <https://doi.org/10.5194/amt-7-3095-2014>, 2014.
- 1173 Seinfeld, J. H., and Pandis, S. N.: Atmospheric chemistry and physics: from air pollution to climate change, John
1174 Wiley & Sons, Inc, Hoboken, New Jersey, 2016.
- 1175 Sen, B., Toon, G. C., Osterman, G. B., Blavier, J.-F., Margitan, J. J., Salawitch, R. J., and Yue, G. K.:
1176 Measurements of reactive nitrogen in the stratosphere, *J. Geophys. Res.-Atmos.*, 103, 3571-3585,
1177 <https://doi.org/10.1029/97JD02468>, 1998.
- 1178 Shin, H. H., and Hong, S.-Y.: Intercomparison of planetary boundary-layer parametrizations in the WRF model
1179 for a single day from CASES-99, *Boundary-Layer Meteorology*, 139, 261-281, <https://doi.org/10.1007/s10546-010-9583-z>, 2011.
- 1181 Silvern, R. F., Jacob, D. J., Mickley, L. J., Sulprizio, M. P., Travis, K. R., Marais, E. A., Cohen, R. C., Laughner,
1182 J. L., Choi, S., Joiner, J., and Lamsal, L. N.: Using satellite observations of tropospheric NO₂ columns to infer
1183 long-term trends in US NO_x emissions: the importance of accounting for the free tropospheric NO₂ background,
1184 *Atmos. Chem. Phys.*, 19, 8863-8878, <https://doi.org/10.5194/acp-19-8863-2019>, 2019.
- 1185 Souri, A. H., Choi, Y., Jeon, W., Li, X., Pan, S., Diao, L., and Westenbarger, D. A.: Constraining NO_x emissions
1186 using satellite NO₂ measurements during 2013 DISCOVER-AQ Texas campaign, *Atmos. Environ.*, 131, 371-
1187 381, <https://doi.org/10.1016/j.atmosenv.2016.02.020>, 2016.
- 1188 Souri, A. H., Choi, Y., Pan, S., Curci, G., Nowlan, C. R., Janz, S. J., Kowalewski, M. G., Liu, J., Herman, J. R.,
1189 and Weinheimer, A. J.: First top - down estimates of anthropogenic NO_x emissions using high - resolution
1190 airborne remote sensing observations, *J. Geophys. Res.-Atmos.*, 123, 3269-3284,
1191 <https://doi.org/10.1002/2017JD028009>, 2018.

- 1192 Spinei, E., Cede, A., Swartz, W. H., Herman, J., and Mount, G. H.: The use of NO₂ absorption cross section
1193 temperature sensitivity to derive NO₂ profile temperature and stratospheric–tropospheric column partitioning
1194 from visible direct-sun DOAS measurements, *Atmos. Meas. Tech.*, 7, 4299-4316, [https://doi.org/10.5194/amt-7-](https://doi.org/10.5194/amt-7-4299-2014)
1195 4299-2014, 2014.
- 1196 Spurr, R.: LIDORT and VLIDORT: Linearized pseudo-spherical scalar and vector discrete ordinate radiative
1197 transfer models for use in remote sensing retrieval problems, in: *Light Scattering Reviews 3*, Springer, 229-275,
1198 2008.
- 1199 [Thompson, A. M., Stauffer, R. M., Boyle, T. P., Kollonige, D. E., Miyazaki, K., Tzortziou, M., Herman, J. R.,](#)
1200 [Abuhassan, N., Jordan, C. E., and Lamb, B. T.: Comparison of Near - Surface NO₂ Pollution With Pandora Total](#)
1201 [Column NO₂ During the Korea - United States Ocean Color \(KORUS OC\) Campaign, *J. Geophys. Res.-Atmos.*](#)
1202 [124, 13560-13575, <https://doi.org/10.1029/2019JD030765>, 2019.](#)
- 1203 Thornton, J. A., Wooldridge, P. J., and Cohen, R. C.: Atmospheric NO₂: In situ laser-induced fluorescence
1204 detection at parts per trillion mixing ratios, *Anal. Chem.*, 72, 528-539, <https://doi.org/10.1021/ac9908905>, 2000.
- 1205 Tong, D., Lamsal, L., Pan, L., Ding, C., Kim, H., Lee, P., Chai, T., Pickering, K. E., and Stajner, I.: Long-term
1206 NO_x trends over large cities in the United States during the great recession: Comparison of satellite retrievals,
1207 ground observations, and emission inventories, *Atmos. Environ.*, 107, 70-84,
1208 <https://doi.org/10.1016/j.atmosenv.2015.01.035>, 2015.
- 1209 Travis, K. R., Jacob, D. J., Fisher, J. A., Kim, P. S., Marais, E. A., Zhu, L., Yu, K., Miller, C. C., Yantosca, R.
1210 M., and Sulprizio, M. P.: Why do models overestimate surface ozone in the Southeast United States?, *Atmos.*
1211 *Chem. Phys.*, 16, 13561-13577, <https://doi.org/10.5194/acp-16-13561-2016>, 2016.
- 1212 Tu, J., Xia, Z.-G., Wang, H., and Li, W.: Temporal variations in surface ozone and its precursors and
1213 meteorological effects at an urban site in China, *Atmospheric Research*, 85, 310-337,
1214 <https://doi.org/10.1016/j.atmosres.2007.02.003>, 2007.
- 1215 Valin, L. C., Russell, A. R., Hudman, R. C., and Cohen, R. C.: Effects of model resolution on the interpretation
1216 of satellite NO₂ observations, *Atmos. Chem. Phys.*, 11, 11647-11655, [https://doi.org/10.5194/acp-11-11647-](https://doi.org/10.5194/acp-11-11647-2011)
1217 2011, 2011.
- 1218 van der A, R. J., Eskes, H. J., Roozendael, M. V., De Smedt, I., Blond, N., Boersma, F., Weiss, A., and van Peet,
1219 J. C. A.: Algorithm Document Tropospheric NO₂, available at http://www.temis.nl/docs/AD_NO2.pdf 1.0, 23,
1220 2010.
- 1221 Van Geffen, J., Boersma, K., Van Roozendael, M., Hendrick, F., Mahieu, E., De Smedt, I., Snee, M., and
1222 Veefkind, J.: Improved spectral fitting of nitrogen dioxide from OMI in the 405–465 nm window, *Atmos. Meas.*
1223 *Tech.*, 8, 1685-1699, <https://doi.org/10.5194/amt-8-1685-2015>, 2015.
- 1224 Van Stratum, B. J. H., Vilà-Guerau de Arellano, J., Ouwersloot, H. G., Dries, K. d., Van Laar, T. W., Martinez,
1225 M., Lelieveld, J., Diesch, J.-M., Drewnick, F., and Fischer, H.: Case study of the diurnal variability of chemically

- 1226 active species with respect to boundary layer dynamics during DOMINO, *Atmos. Chem. Phys.*, 12, 5329-5341,
1227 <https://doi.org/10.5194/acp-12-5329-2012>, 2012.
- 1228 Wooldridge, P. J., Perring, A. E., Bertram, T. H., Flocke, F. M., Roberts, J. M., Singh, H. B., Huey, L. G.,
1229 Thornton, J. A., Wolfe, G. M., and Murphy, J. G.: Total Peroxy Nitrates ([Sigma] PNs) in the atmosphere: the
1230 Thermal Dissociation-Laser Induced Fluorescence (TD-LIF) technique and comparisons to speciated PAN
1231 measurements, *Atmos. Meas. Tech.*, 3, 593, <https://doi.org/10.5194/amt-3-593-2010>, 2010.
- 1232 Yuan, H., McGinley, J. A., Schultz, P. J., Anderson, C. J., and Lu, C.: Short-range precipitation forecasts from
1233 time-lagged multimodel ensembles during the HMT-West-2006 campaign, *Journal of Hydrometeorology*, 9, 477-
1234 491, <https://doi.org/10.1175/2007JHM879.1>, 2008.
- 1235 Zhang, R., Wang, Y., Smeltzer, C., Qu, H., Koshak, W., and Boersma, K. F.: Comparing OMI-based and EPA
1236 AQS in situ NO₂ trends: towards understanding surface NO_x emission changes, *Atmos. Meas. Tech.*, 11, 3955-
1237 3967, <https://doi.org/10.5194/amt-11-3955-2018>, 2018.
- 1238 Zhang, Y., and Wang, Y.: Climate-driven ground-level ozone extreme in the fall over the Southeast United
1239 States, *Proc. Natl. Acad. Sci. U.S.A.*, 113, 10025-10030, <https://doi.org/10.1073/pnas.1602563113>, 2016.
- 1240 Zhang, Y., Wang, Y., Chen, G., Smeltzer, C., Crawford, J., Olson, J., Szykman, J., Weinheimer, A. J., Knapp, D.
1241 J., and Montzka, D. D.: Large vertical gradient of reactive nitrogen oxides in the boundary layer: Modeling
1242 analysis of DISCOVER - AQ 2011 observations, *J. Geophys. Res.-Atmos.*, 121, 1922-1934,
1243 <https://doi.org/10.1002/2015JD024203>, 2016.
- 1244 Zhao, C., Wang, Y., Choi, Y., and Zeng, T.: Summertime impact of convective transport and lightning NO_x
1245 production over North America: modeling dependence on meteorological simulations, *Atmos. Chem. Phys.*, 9,
1246 4315-4327, <https://doi.org/10.5194/acp-9-4315-2009>, 2009.
- 1247 [Zhao, X., Griffin, D., Fioletov, V., McLinden, C., Davies, J., Ogyu, A., Lee, S. C., Lupu, A., Moran, M. D.,
1248 Cede, A., Tiefengraber, M., and Müller, M.: Retrieval of total column and surface NO₂ from Pandora zenith-sky
1249 measurements, *Atmos. Chem. Phys.*, 19, 10619-10642, <https://doi.org/10.5194/acp-19-10619-2019>, 2019.](https://doi.org/10.5194/acp-19-10619-2019)
- 1250 [Zhao, X., Griffin, D., Fioletov, V., McLinden, C., Cede, A., Tiefengraber, M., Müller, M., Bogner, K., Strong,
1251 K., Boersma, F., Eskes, H., Davies, J., Ogyu, A., and Lee, S. C.: Assessment of the quality of TROPOMI high-
1252 spatial-resolution NO₂ data products in the Greater Toronto Area, *Atmos. Meas. Tech.*, 13, 2131-2159,
1253 <https://doi.org/10.5194/amt-13-2131-2020>, 2020.](https://doi.org/10.5194/amt-13-2131-2020)
- 1254 Zheng, Y., Alapaty, K., Herwehe, J. A., Del Genio, A. D., and Niyogi, D.: Improving high-resolution weather
1255 forecasts using the Weather Research and Forecasting (WRF) Model with an updated Kain-Fritsch scheme,
1256 *Monthly Weather Review*, 144, 833-860, <https://doi.org/10.1175/MWR-D-15-0005.1>, 2016.

1257
1258**Table 1.** Comparison of the concentrations of NO_y and its components between REAM and P-3B aircraft measurements during the DISCOVER-AQ campaign

			NO _y / ppb ¹	NO / ppb	NO ₂ _NCAR / ppb	NO ₂ _LIF / ppb ²	∑PNs / ppb	∑ANs / ppb	HNO ₃ / ppb	Derived-NO _y / ppb ³
36-km ⁴	Weekday ⁵	P-3B	2.51 ± 2.09	0.18 ± 0.29	0.85 ± 1.13	0.68 ± 0.95	0.70 ± 0.58	0.31 ± 0.23	1.15 ± 0.73	2.86 ± 2.26
		REAM	3.64 ± 3.13 5	0.18 ± 0.30 4	0.74 ± 1.04 6	0.68 ± 0.89 90	0.54 3 ± 0.45	0.10 ± 0.09	1.80 ± 1.61 2	3.10 ± 2.70 4
		R ²	0.33	0.35 3	0.38 7	0.34 3	0.37	0.38	0.24	0.41
	Weekend	P-3B	3.00 4 ± 2.18 9	0.15 ± 0.20	0.71 ± 0.80	0.63 ± 0.72	0.91 ± 0.53	0.36 ± 0.21	1.15 ± 0.79	2.96 ± 2.15
		REAM	3.78 6 ± 2.20 4	0.15 ± 0.17	0.54 3 ± 0.59 64	0.53 ± 0.58 60	0.53 2 ± 0.29	0.09 ± 0.06	2.31 0 ± 1.38 40	3.43 4 ± 2.26 30
		R ²	0.29	0.28	0.41	0.45	0.27	0.39 8	0.50 49	0.51
4-km	Weekday	P-3B	2.51 ± 2.15	0.19 ± 0.30	0.86 5 ± 1.27 9	0.68 7 ± 0.98 6	0.70 ± 0.59	0.31 ± 0.22	1.17 ± 0.74	2.90 ± 2.27
		REAM	3.81 67 ± 3.81 63	0.19 7 ± 0.35 29	0.79 4 ± 1.31 42	0.76 2 ± 1.24 0	0.46 5 ± 0.51	0.08 ± 0.10	2.03 4 +99 ± 1.91 2	3.31 23 ± 3.28 4
		R ²	0.28 5	0.22 46	0.26 48	0.32 55	0.37	0.29 7	0.38 60	0.47 4
	Weekend	P-3B	2.96 7 ± 2.13	0.14 5 ± 0.18	0.69 ± 0.74 5	0.63 5 ± 0.71 85	0.91 0 ± 0.51	0.35 ± 0.21	1.15 ± 0.80 79	2.94 3 ± 2.09 8
		REAM	4.36 22 ± 3.66 79	0.25 4 ± 0.40 2	0.85 3 ± 1.28 40	0.81 78 ± 1.23 34	0.41 38 ± 0.29 7	0.08 7 ± 0.08	2.54 48 ± 1.99 2 -04	3.72 59 ± 3.52 9
		R ²	0.21 0	0.15 33	0.19 37	0.18 30	0.16 5	0.23 0	0.38 59	0.37 5

1259
1260
1261
1262
1263
1264
1265
1266
1267
1268
1269
1270
1271
1272
1273
1274
1275
1276

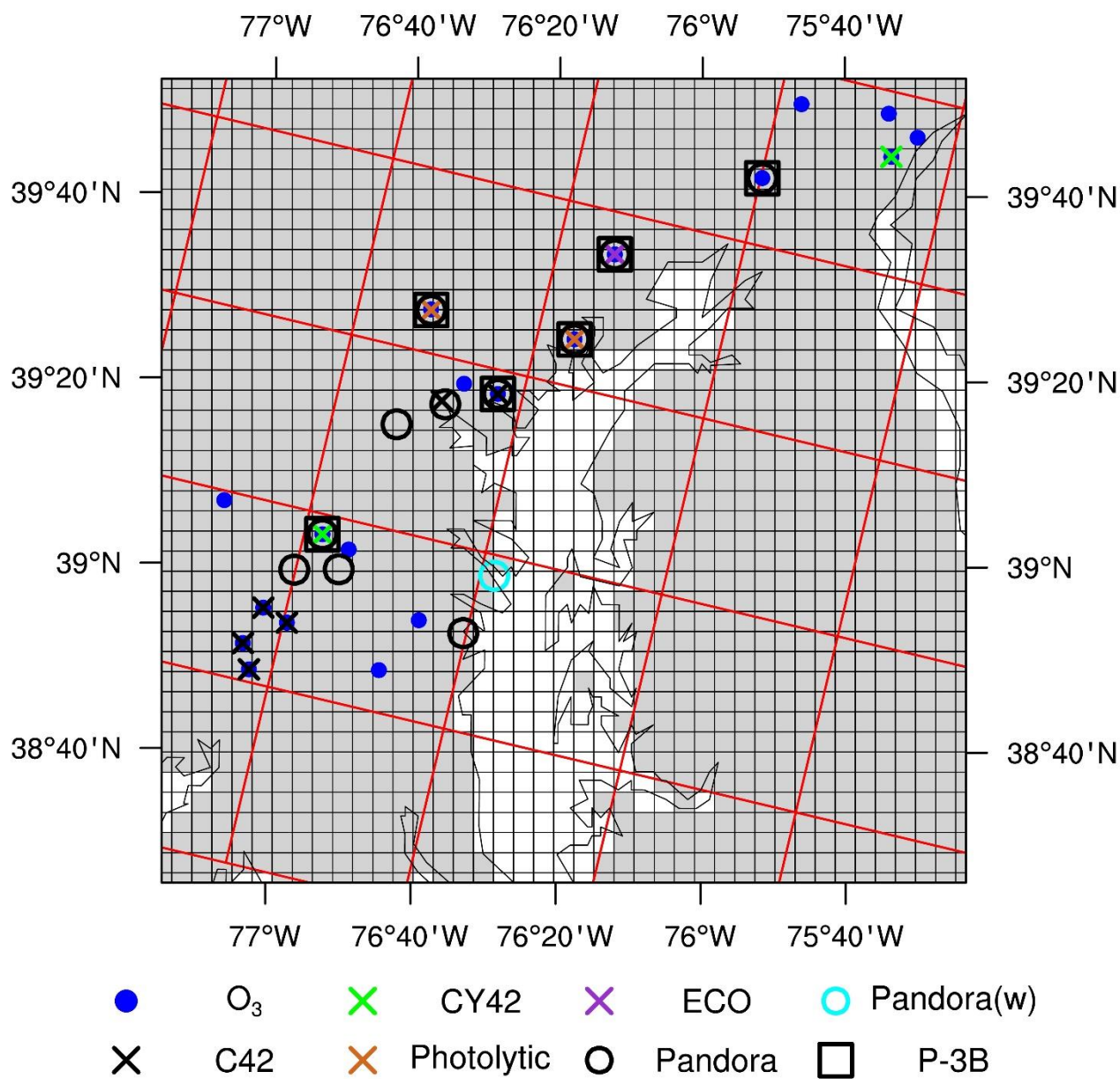
¹ For P-3B, the concentrations of NO_y, NO, and NO₂_NCAR were measured by using the NCAR 4-channel chemiluminescence instrument. The measurement uncertainties are 10%, 10 - 15%, and 10% for NO, NO₂, and NO_y, respectively. The 1-second, 1-sigma detection limits are 20 pptv, 30 pptv, and 20 pptv for NO, NO₂, and NO_y, respectively (https://discover-aq.larc.nasa.gov/pdf/2010STM/Weinheimer20101005_DISCOVERAQ_AJW.pdf). For REAM, NO_y is the sum of NO, NO₂, total peroxyacyl nitrates (∑PNs), total alkyl nitrates (∑ANs) (include alkyl nitrates and hydroxyalkyl nitrates), HNO₃, HONO, 2 × N₂O₅, HNO₄, first generation C5 carbonyl nitrate (nighttime isoprene nitrate ISN1: C₅H₈NO₄), 2 × C5 dihydroxydinitrate (DHDN: C₅H₁₀O₈N₂), methyl peroxy nitrate (MPN: CH₃O₂NO₂), propanone nitrate (PROPNN: CH₃C(=O)CH₂ONO₂), nitrate from methyl vinyl ketone (MVKN: HOCH₂CH(ONO₂)C(=O)CH₃), nitrate from methacrolein (MARN: HOCH₂C(ONO₂)(CH₃)CHO), and ethanol nitrate (ETHLN: CHOCH₂ONO₂).

² For P-3B, the concentrations of NO₂_LIF, ∑PNs, ∑ANs, and HNO₃ were measured by applying the thermal dissociation-laser induced fluorescence (TD-LIF) technique. The accuracy of TD-LIF measurements of NO₂, ∑PNs, ∑ANs, and HNO₃ is better than 15%, and the detection limit for the sum of NO₂, ∑PNs, ∑ANs, and HNO₃ is ~ 10 ppt 10 s⁻¹ (Day et al., 2002).

³ To compare NO_y concentrations from TD-LIF measurements with those from REAM, we calculate derived-NO_y as the sum of NO, NO₂_LIF, ∑PNs, ∑ANs, and HNO₃. Only when the concentrations of all the five species are available at the same hour in the same grid cell, we can calculate derived-NO_y at the given hour in the given grid cell. Therefore, in Table 1, the averaged derived-NO_y values are not exactly equal to the sum of averaged NO, NO₂_LIF, ∑PNs, ∑ANs, and HNO₃ concentrations that only depend on the availability of a single species. In addition, the measurement times and frequencies between NO_y and derived-NO_y are not the same. A comparison between these two types of data needs coincident sampling, as described in the main text.

⁴ Mean NO_x emissions over the six P-3B spiral sites are close (relative difference < 4%) between the 36-km and 4-km REAM (Table S1).

⁵ Due to different sampling times and locations between weekdays and weekends, we do not recommend a direct comparison between weekday and weekend values here.



1277 **Figure 1.** The locations of surface and P-3B aircraft observations during the DISCOVER-AQ 2011 campaign. We mark the
 1278 36-km REAM grid cells with red lines and the 4-km REAM grid cells with black lines. Gray shading denotes land surface in
 1279 the nested 4-km WRF domain, while white area denotes ocean/water surface. Blue dots denote surface O₃ observation sites.
 1280 Cross-marks denote surface NO₂ observation sites, and their colors denote different measurement instruments: green for the
 1281 Thermo Electron 42C-Y NO_y analyzer, dark orchid for the Ecotech Model 9841/9843 T-NO_y analyzers, black for the
 1282 Thermo Model 42C NO_x analyzer, and chocolate for the Teledyne API model 200eup photolytic NO_x analyzer. Circles
 1283 denote Pandora sites, and the cyan circle denotes a Pandora site (USNA) on a ship. Black squares denote the inland P-3B
 1284 aircraft spiral locations.
 1285
 1286

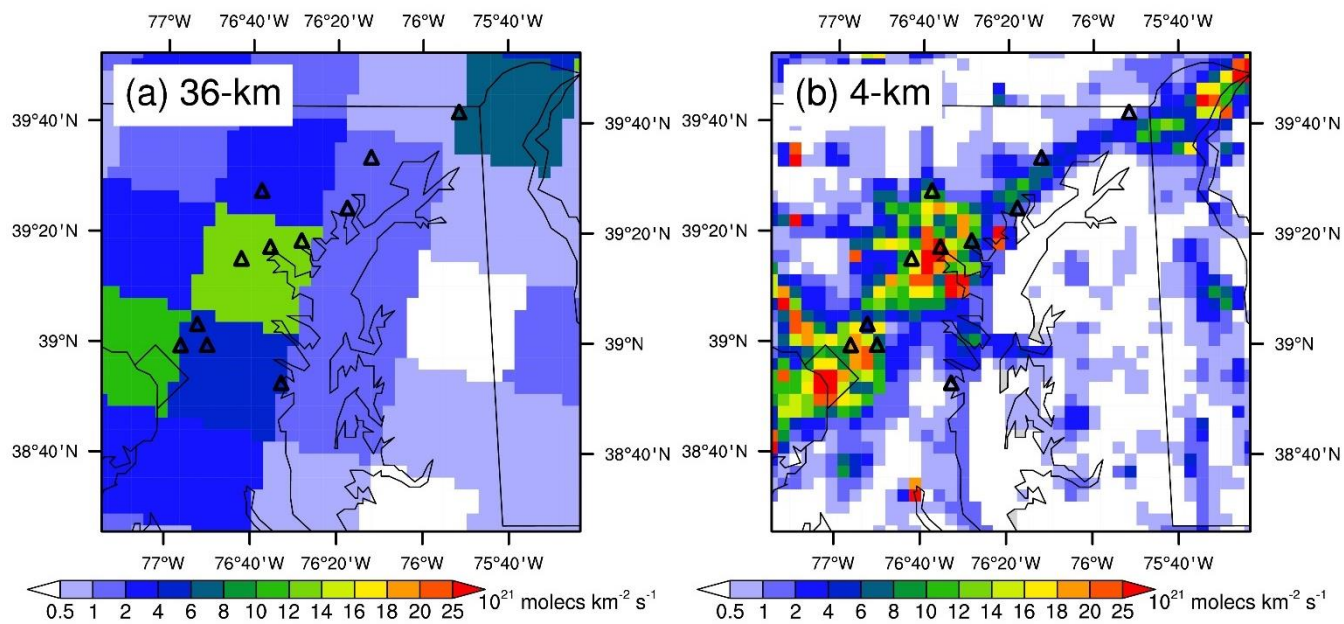
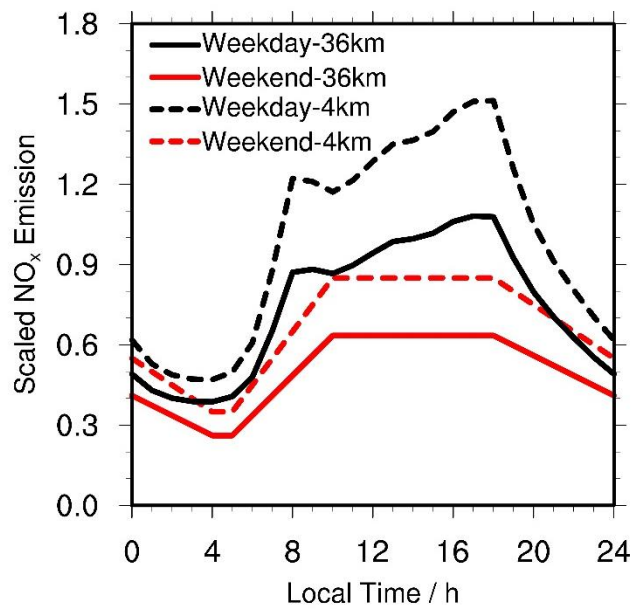
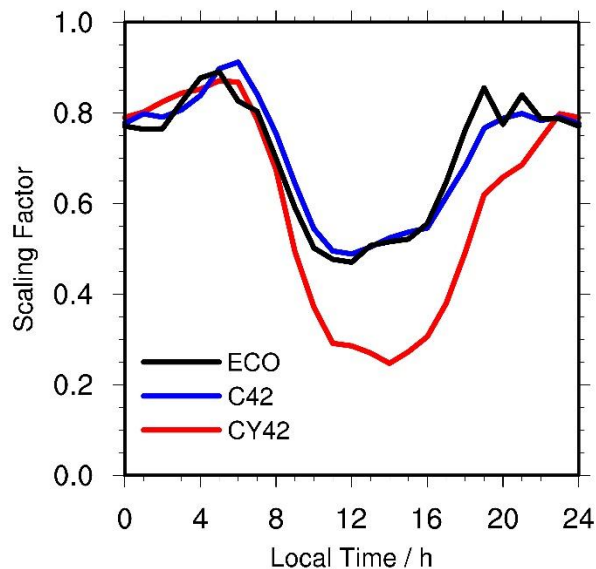


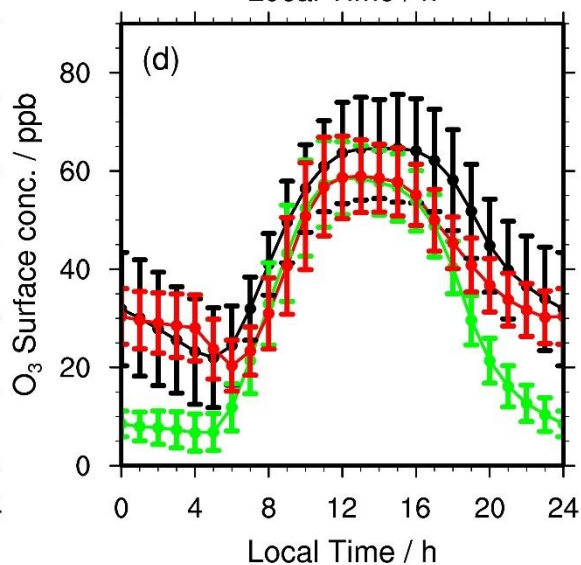
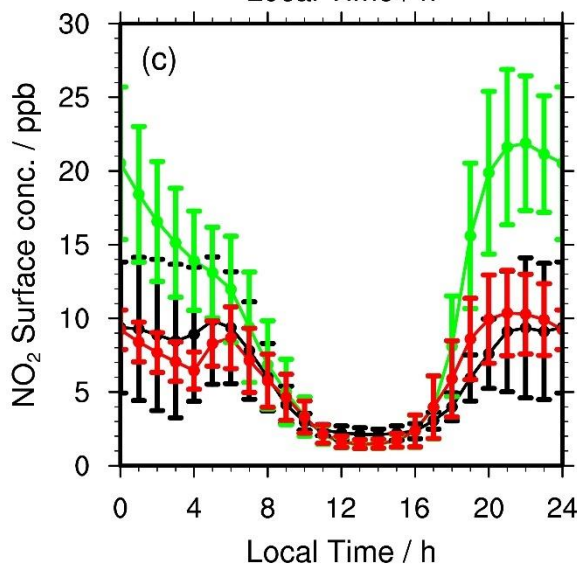
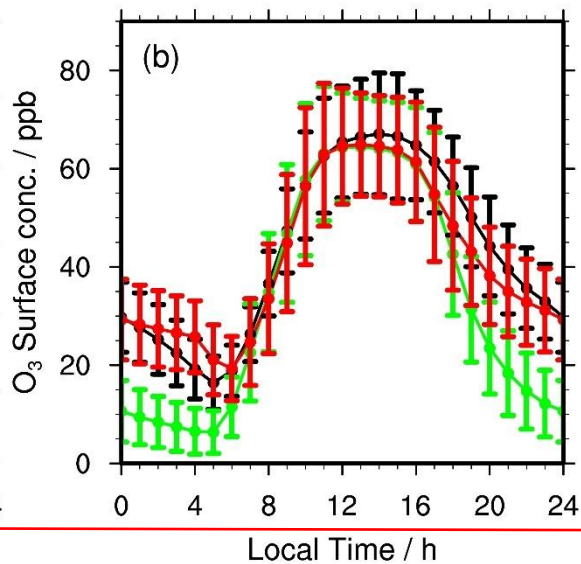
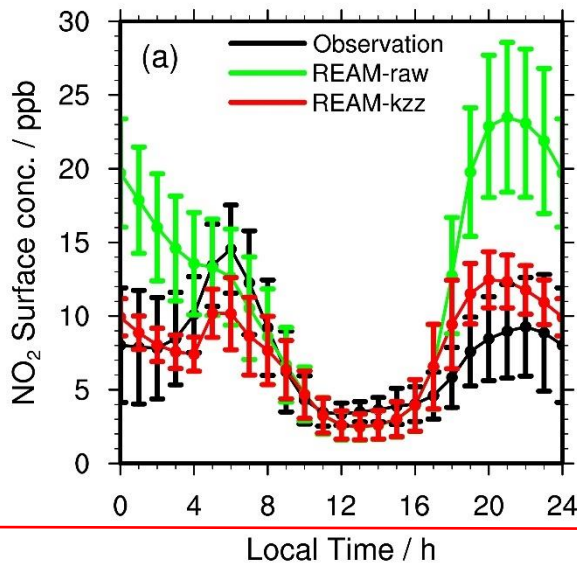
Figure 2. Distributions of NO_x emissions for the (a) 36-km and (b) 4-km REAM simulations around the DISCOVER-AQ 2011 region. Here NO_x emissions refer to the mean values ($\text{molecules km}^{-2} \text{s}^{-1}$) in one week (Monday – Sunday).

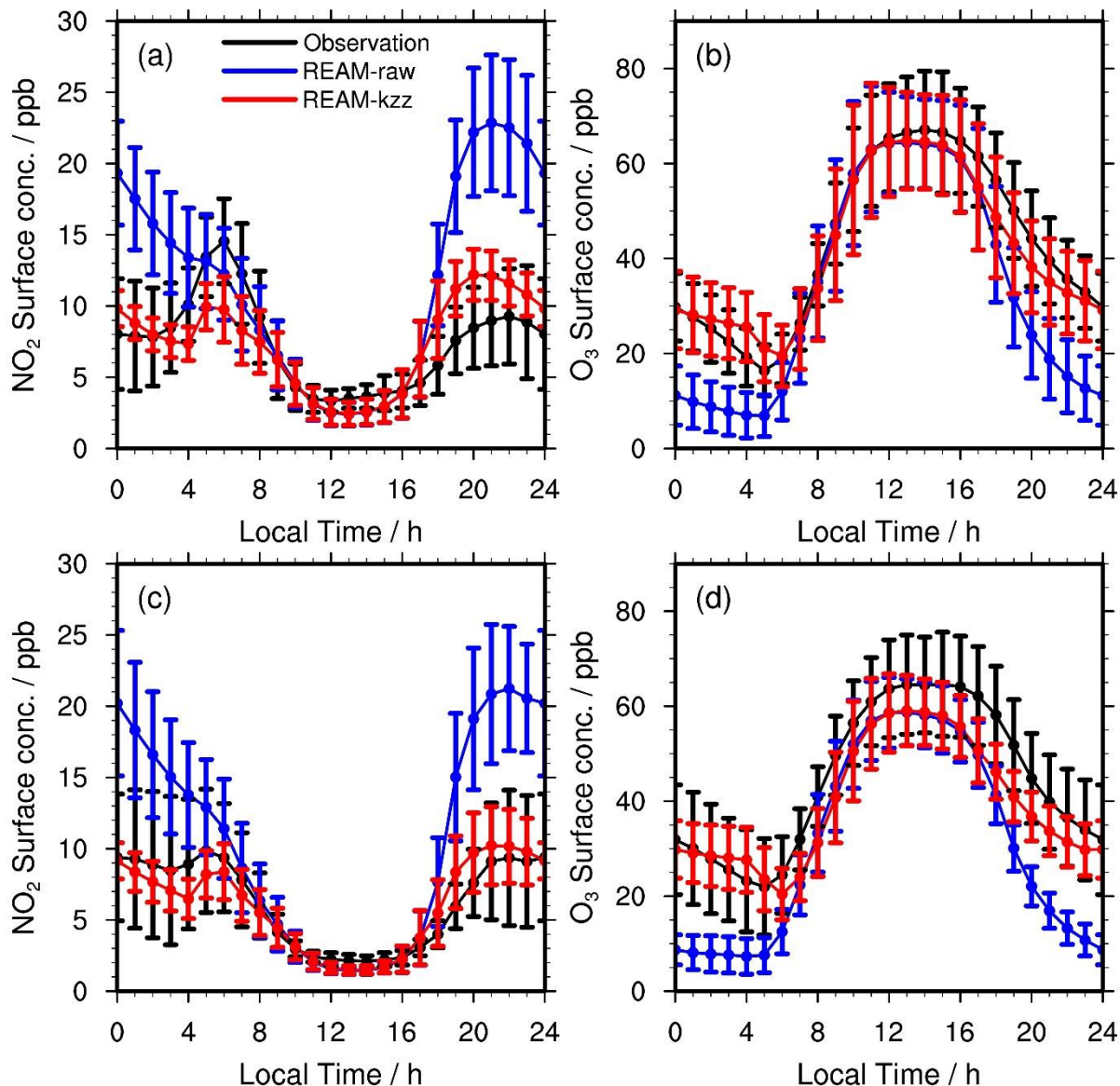


1291
 1292 **Figure 34.** Relative diurnal profiles of weekday and weekend NO_x emissions ($\text{molecules km}^{-2} \text{s}^{-1}$) in the DISCOVER-AQ
 1293 2011 region (the 36/4 km grid cells over the 11 inland Pandora sites shown in Figure S1) for the 36-km and 4-km REAM.
 1294 All the profiles are scaled by the 4-km weekday emission average value ($\text{molecules km}^{-2} \text{s}^{-1}$).
 1295



1296
1297 **Figure 42.** Hourly ratios of NO₂ measurements from the Teledyne API model 200 eup photolytic NO_x analyzer to NO₂ from
1298 coincident catalytic instruments for 2011 July. “CY42” denotes the ratios of photolytic NO₂ to NO₂ from the Thermo
1299 Electron 42C-Y NO_y analyzer in Edgewood, “C42” denotes the ratios of photolytic NO₂ to NO₂ from the Thermo Model
1300 42C NO_x analyzer in Padonia, and “ECO” denotes the ratios of photolytic NO₂ to NO₂ from the Ecotech Model 9841 T-NO_y
1301 analyzer in Padonia. “ECO” ratios are also used to scale NO₂ measurements from the Ecotech Model 9843 T-NO_y analyzer.
1302 ~~Thermo Model 42I-Y NO_y analyzer was used only in Padonia, where photolytic measurements were available, so we do not~~
1303 ~~use the Thermo Model 42I-Y NO_y analyzer measurements in this study.~~
1304





1306
 1307 **Figure 53.** Diurnal cycles of surface (a, c) NO₂ and (b, d) O₃ concentrations on (a, b) weekdays and (c, d) weekends during
 1308 the DISCOVER-AQ campaign in the DISCOVER-AQ region (the 36-km grid cells over the 11 inland Pandora sites shown
 1309 in Figure S1). Black lines denote the mean observations from all the 11 NO₂ surface monitoring sites and 19 O₃ surface sites
 1310 during the campaign (Figure S1), as mentioned in Section 2.5. “REAM-raw” (green-blue lines) denotes the coincident 36-km
 1311 REAM simulation results with WRF-YSU simulated k_{zz} data, and “REAM-kzz” (red lines) is the coincident 36-km REAM
 1312 simulation results with updated k_{zz} data. See the main text for details. Vertical bars denote corresponding standard deviations.
 1313

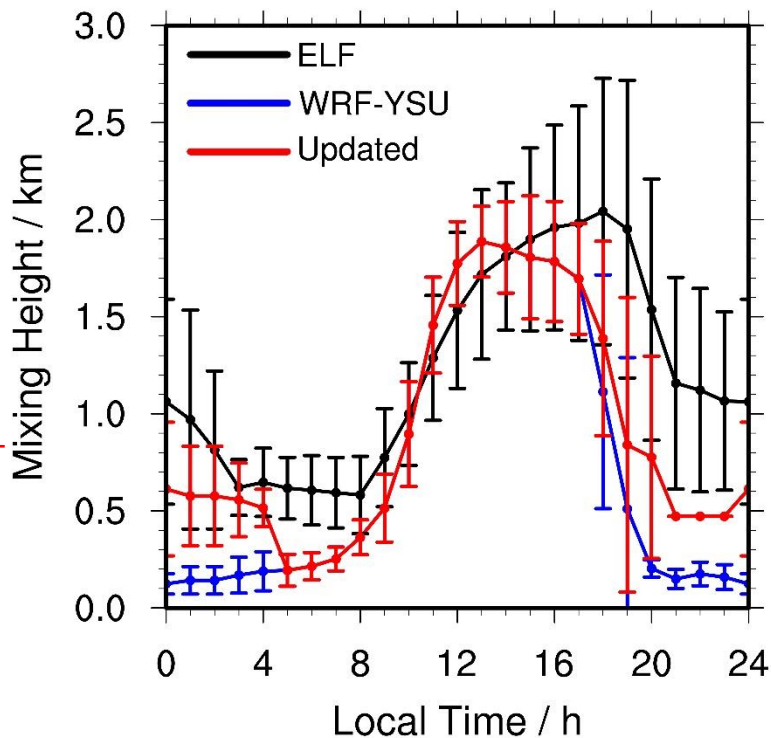
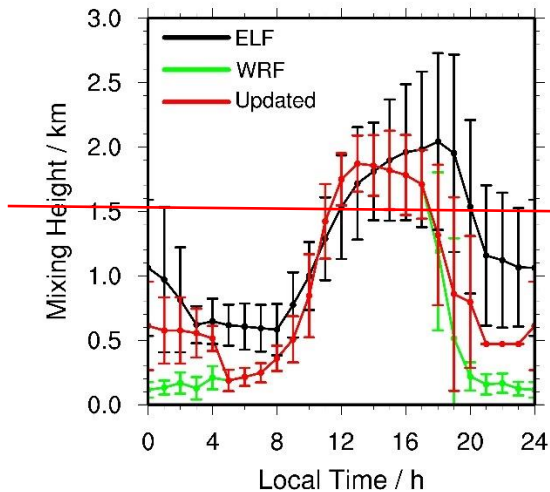
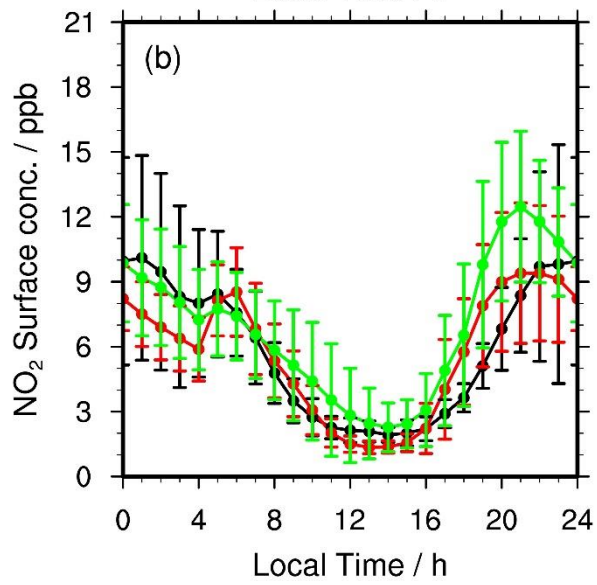
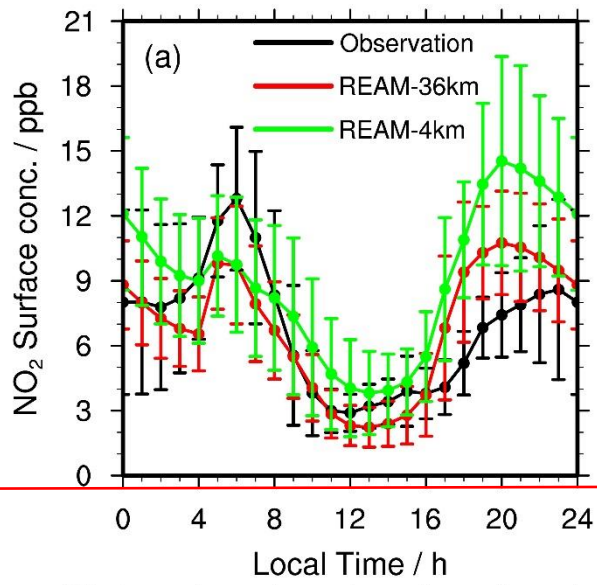
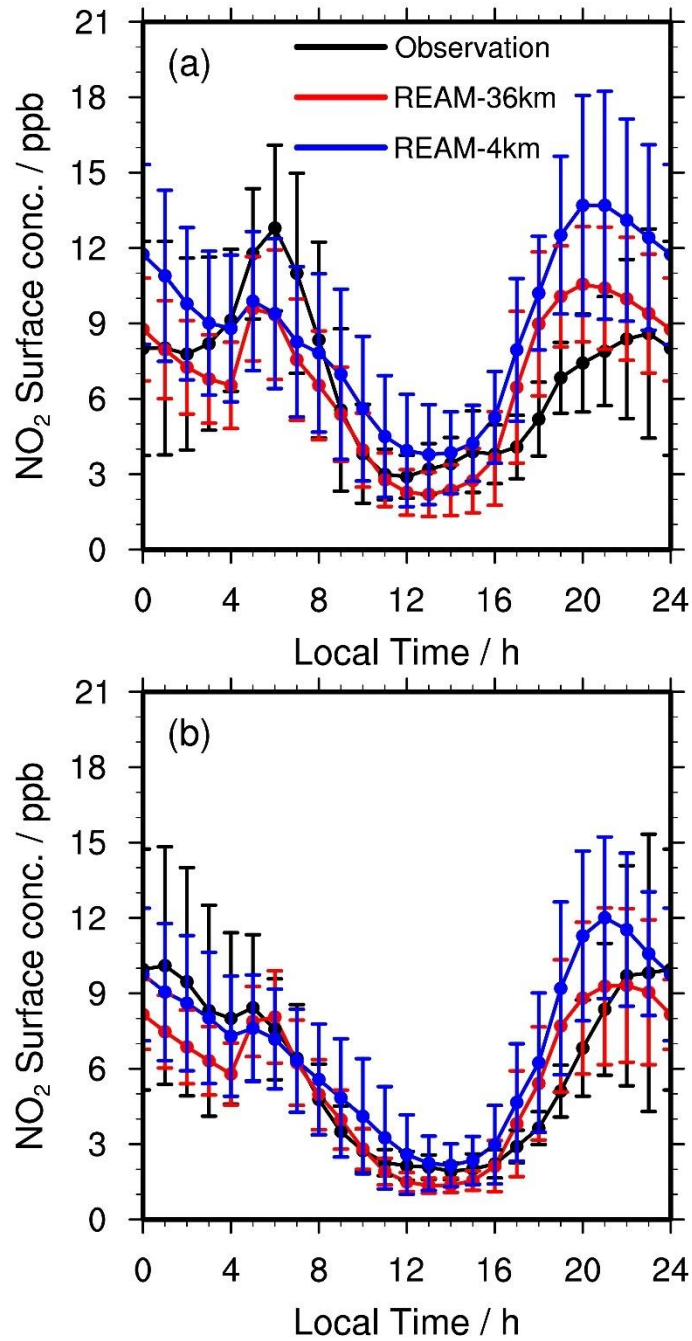
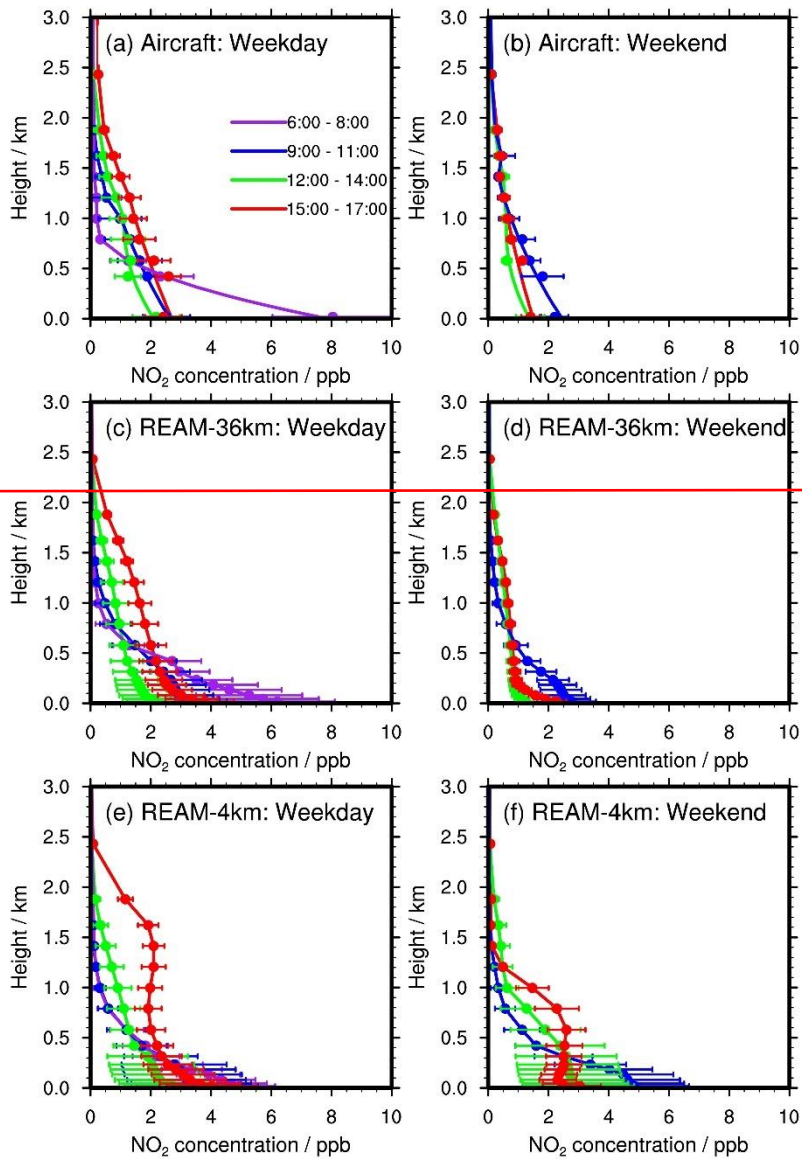


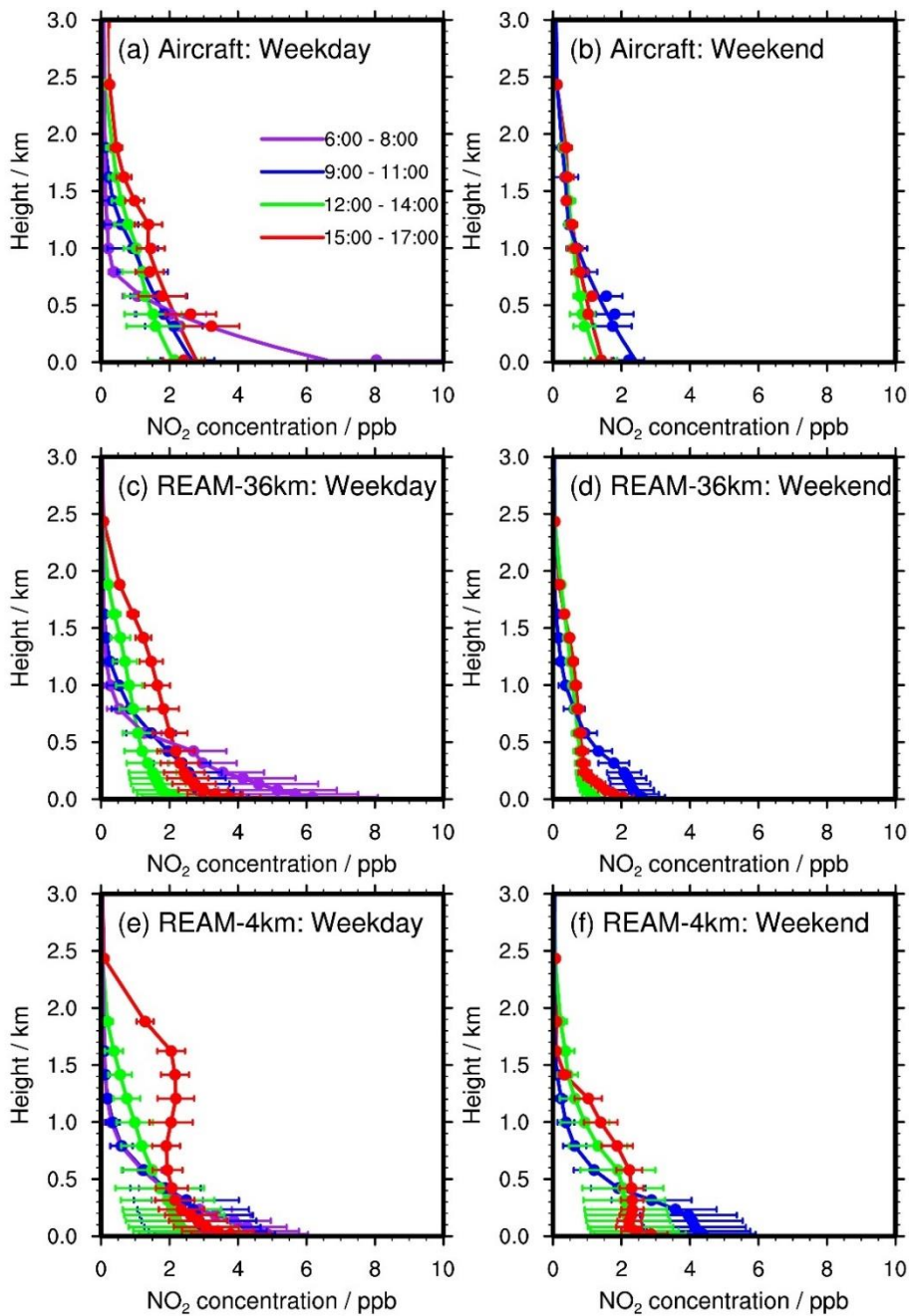
Figure 64. ELF observed and model simulated diurnal variations of PBLH at the UMBC site during the Discover-AQ campaign. “ELF” denotes ELF derived PBLHs by using the covariance wavelet transform method. “WRF-YSU” denotes the 36-km WRF-YSU k_{zz} -determined PBLHs, and “Updated” denotes updated k_{zz} -determined PBLHs. See the main text for details. Vertical bars denote standard deviations.



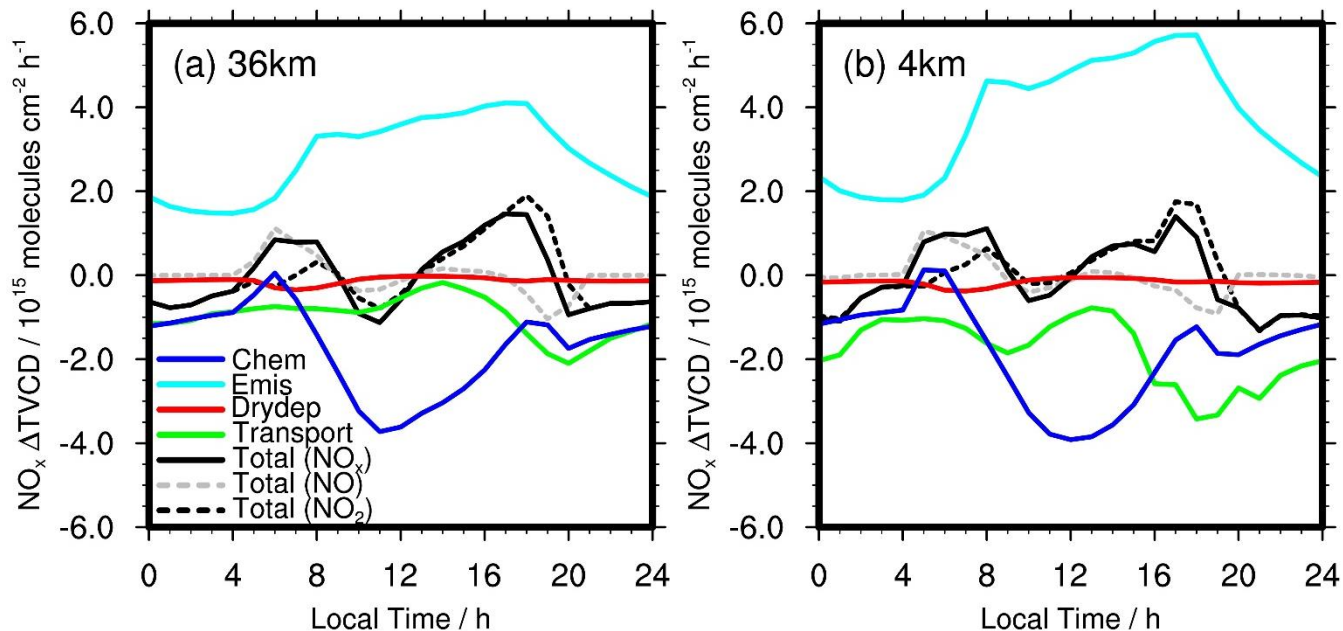


1321
 1322 **Figure 75.** Diurnal cycles of observed and simulated average surface NO₂ concentrations over Padonia, Oldtown, Essex,
 1323 Edgewood, Beltsville, and Aldino (Table S1) on (a) weekdays and (b) weekends. Black lines denote mean observations from
 1324 the six sites. Red lines denote coincident 36-km REAM simulation results, and ~~green-blue~~ lines are for coincident 4-km
 1325 REAM simulation results. Error bars denote standard deviations.
 1326

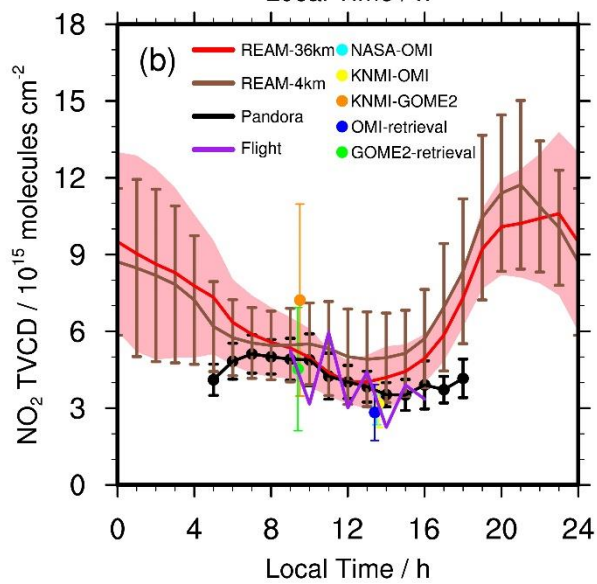
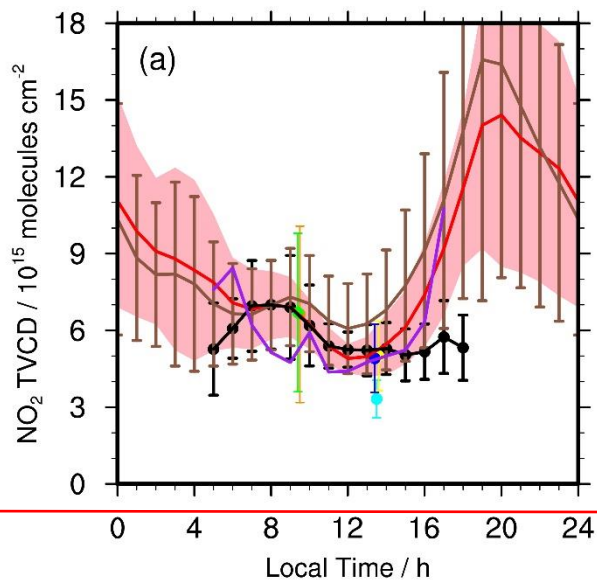


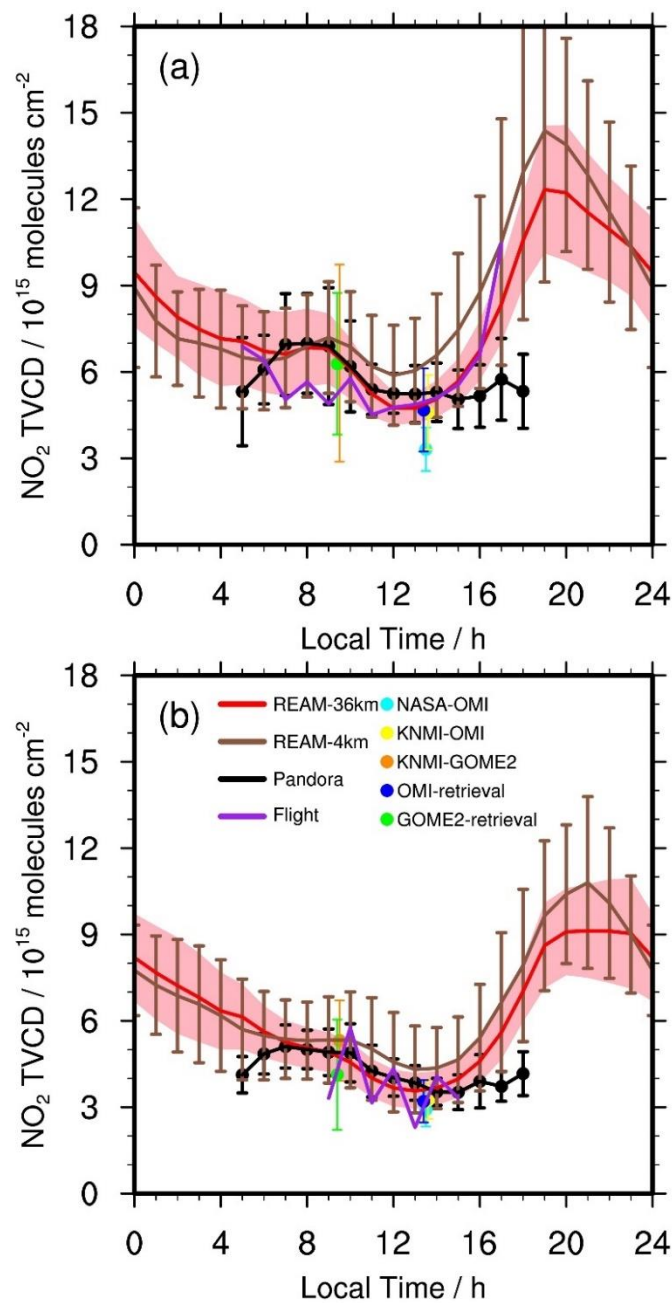


1328
 1329 **Figure 86.** Temporal evolutions of NO₂ vertical profiles below 3 km on (a, c, e) weekdays and (b, d, f) weekends from the
 1330 (a, b) P-3B aircraft and (c, d) 36-km and (e, f) 4-km REAM during the DISCOVER-AQ campaign. Horizontal bars denote
 1331 the corresponding standard deviations. In (a) and (b), dots denote aircraft measurements, while lines below 1 km are based
 1332 on quadratic polynomial fitting, as described in section 2.6. The fitting values are mostly in reasonable agreement with the
 1333 aircraft and surface measurements in the boundary layer. On weekends, no aircraft observations were made at 6:00 – 8:00
 1334 LT, and therefore no corresponding model profiles are shown.
 1335

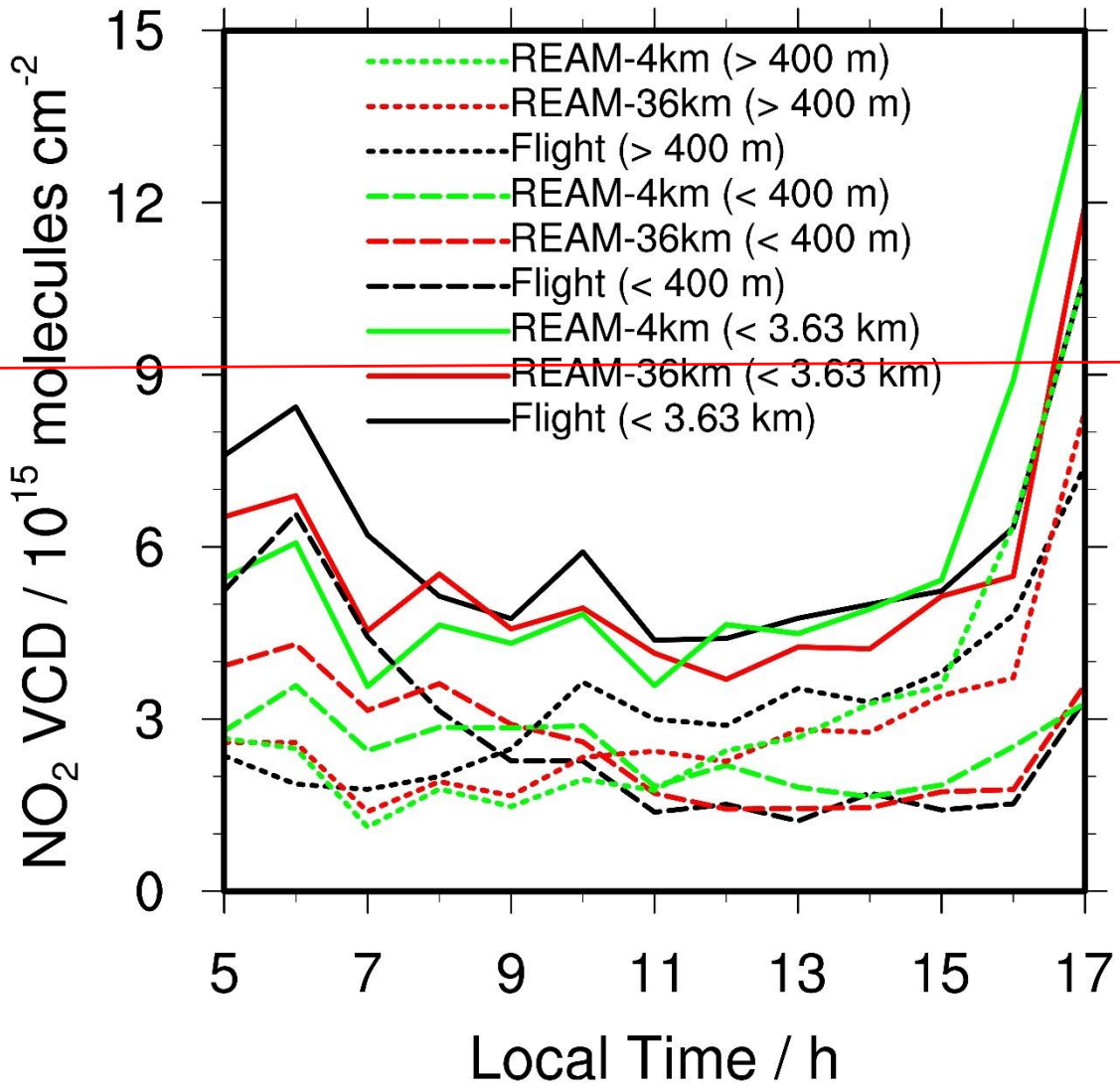


1336
 1337 **Figure 9.** Contributions of emission, chemistry, transport, and dry deposition to NO_x TVCD diurnal variations over the 11
 1338 inland Pandora sites (Table S1 and Figure 1) on weekdays in July 2011 for the (a) 36-km and (b) 4-km REAM simulations.
 1339 “Chem” refers to net NO_x chemistry production; “Emis” refers to NO_x emissions; “Drydep” denotes NO_x dry depositions;
 1340 “Transport” includes advection, turbulent mixing, lightning NO_x production, and wet deposition. “Total (NO_x)” is the hourly
 1341 change of NO_x TVCDs ($\Delta(\text{TVCD}) = \text{TVCD}_{t+1} - \text{TVCD}_t$). “Total (NO_2)” is the hourly change of NO_2 TVCDs, and “Total
 1342 (NO)” is the hourly change of NO TVCDs.
 1343





1345
 1346 **Figure 107.** Daily variations of NO₂ TVCDs on (a) weekdays and (b) weekends during the DISCOVER-AQ campaign.
 1347 “REAM-36km” refers to the 36-km REAM simulation results over the 11 inland Pandora sites. “REAM-4km” refers to the
 1348 4-km REAM simulation results over the 11 inland Pandora sites. “Pandora” refers to updated Pandora TVCD data. “Flight”
 1349 denotes P-3B aircraft-derived NO₂ VCDs below 3.63 km. “NASA-OMI” denotes the OMI NO₂ TVCDs retrieved by NASA
 1350 over the Pandora sites; “KNMI-OMI” denotes the OMI NO₂ TVCDs from KNMI; “KNMI-GOME2” is the GOME-2A NO₂
 1351 TVCDs from KNMI. “OMI-retrieval” and “GOME2-retrieval” denote OMI and GOME-2A TVCDs retrieved by using the
 1352 KNMI DOMINO algorithm with corresponding 36-km REAM vertical profiles, respectively. We list NO₂ TVCD values at
 1353 9:30 and 13:30 LT in Table S3.



1355

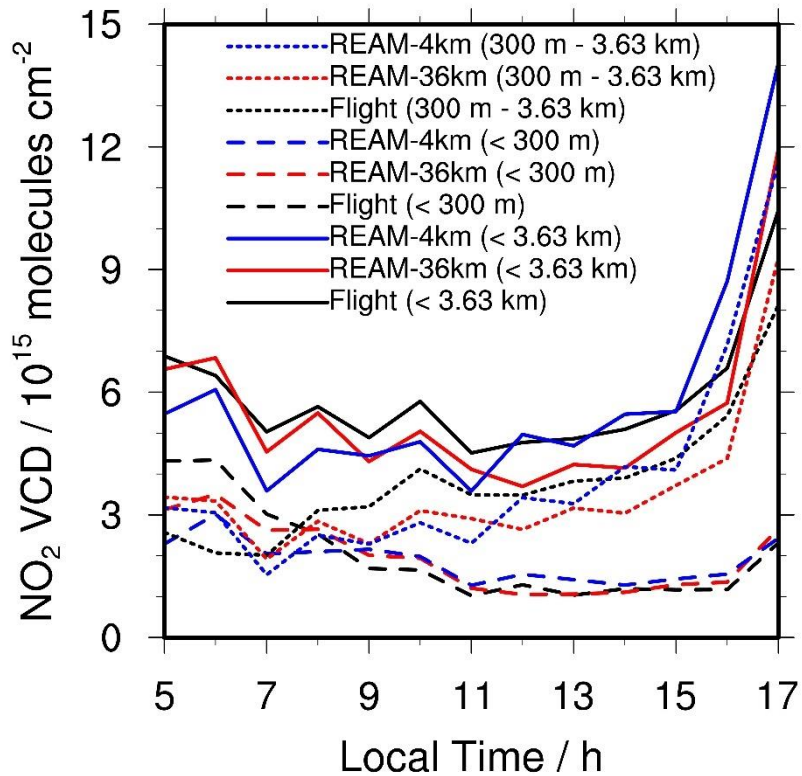
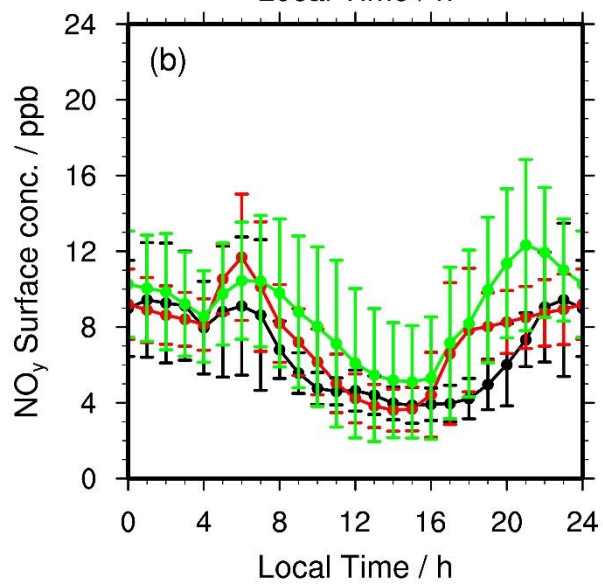
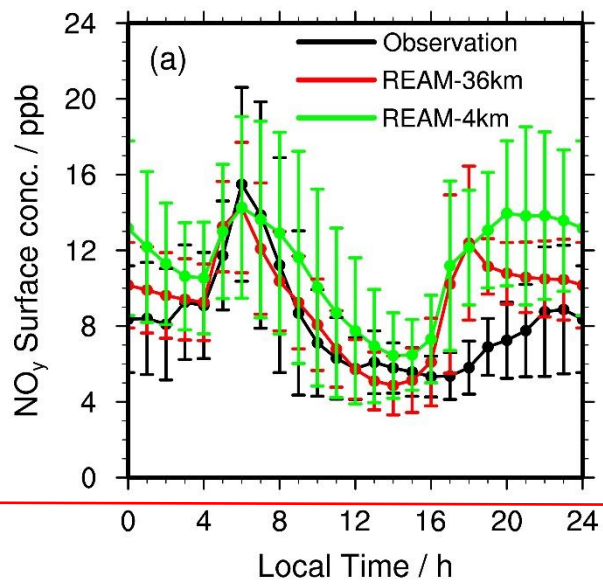
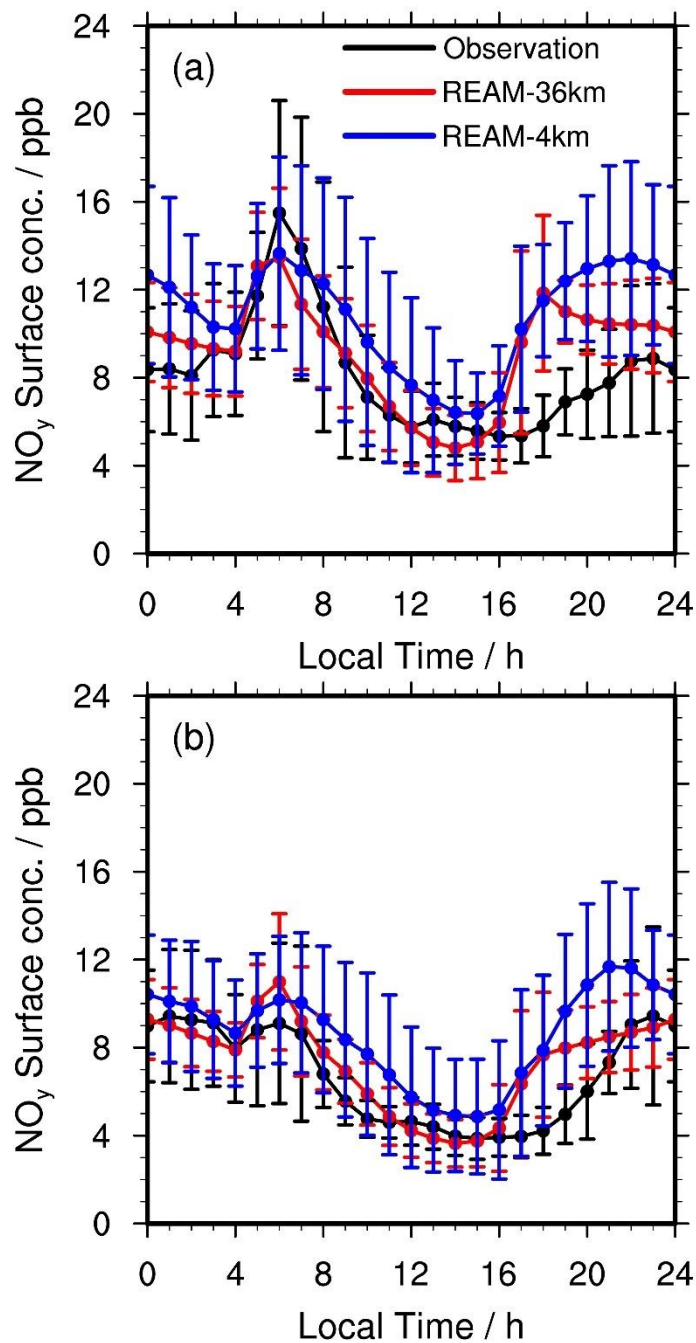


Figure 118. Weekday hourly variations of NO₂ VCDs at different height (AGL) bins (< 3.63 km AGL, < 3400 m AGL, and 3400 m ~ 3.63 km AGL) based on P-3B aircraft-derived datasets and the 36-km and 4-km REAM results. “Flight” denotes P-3B aircraft-derived NO₂ VCDs, “REAM-36km” denotes coincident 36-km REAM simulated VCDs, and “REAM-4km” denotes coincident 4-km REAM simulated VCDs.





1363
 1364 **Figure 129.** Diurnal cycles of observed and simulated average surface NO_y concentrations at Padonia, Edgewood, Beltsville,
 1365 and Aldino on (a) weekdays and (b) weekends. Vertical bars denote the corresponding standard deviations. It is noteworthy
 1366 that the mean NO_x emissions over Padonia, Edgewood, Beltsville, and Aldino are 99% higher in the 4-km than the 36-km
 1367 REAM simulations (Table S1 and Figure S1).
 1368

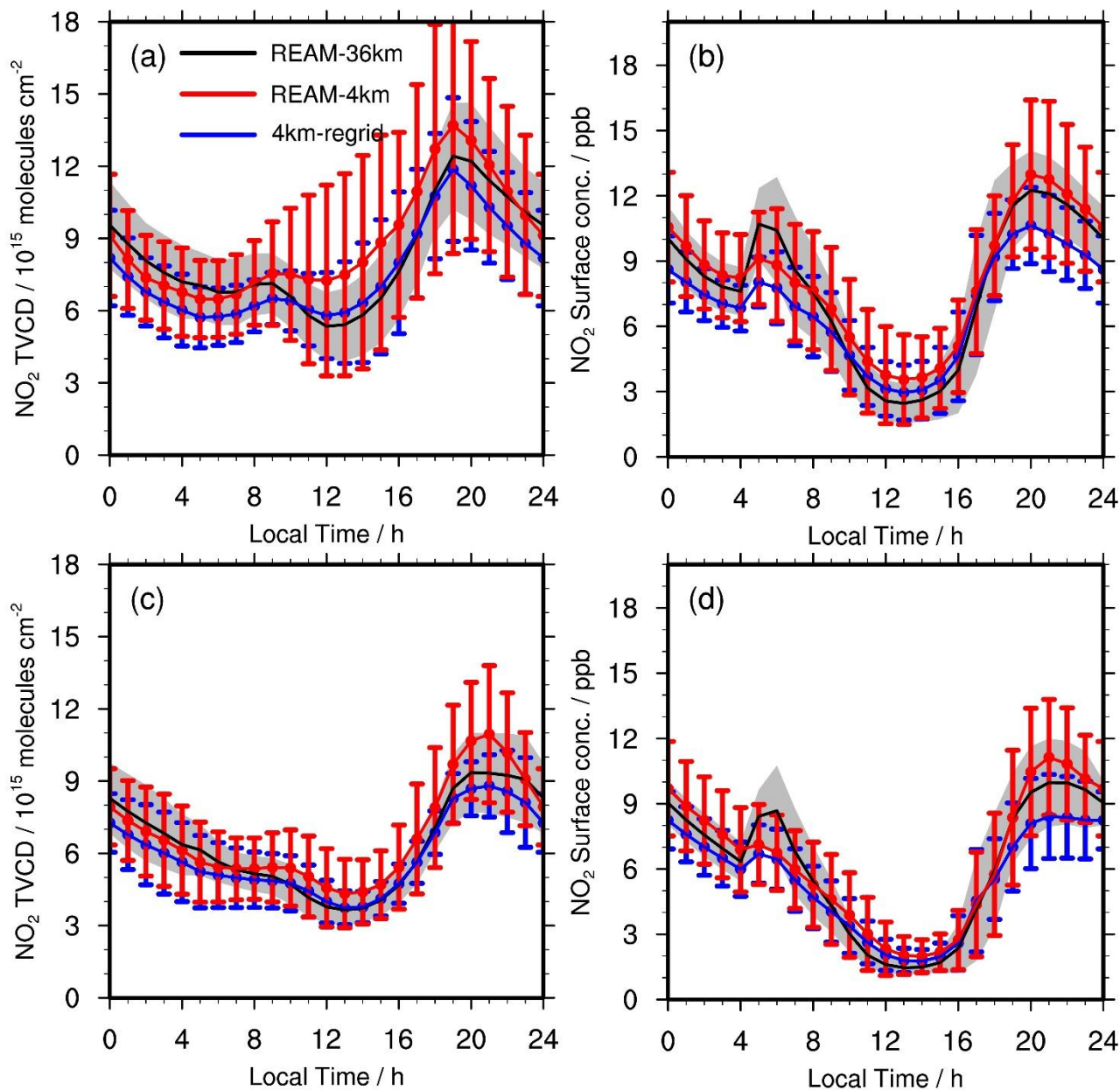
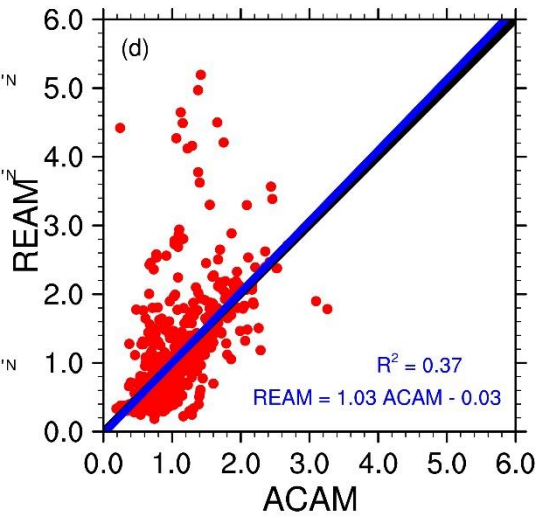
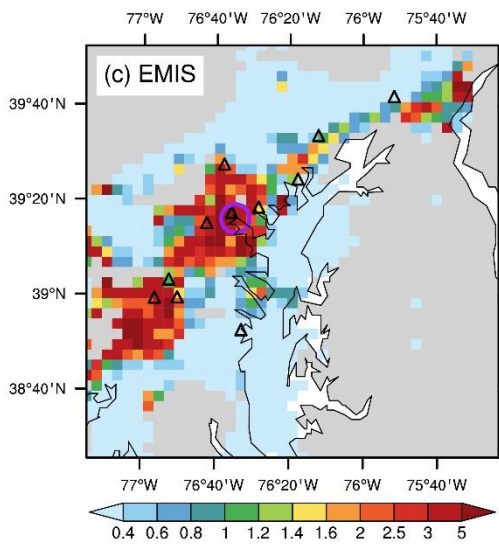
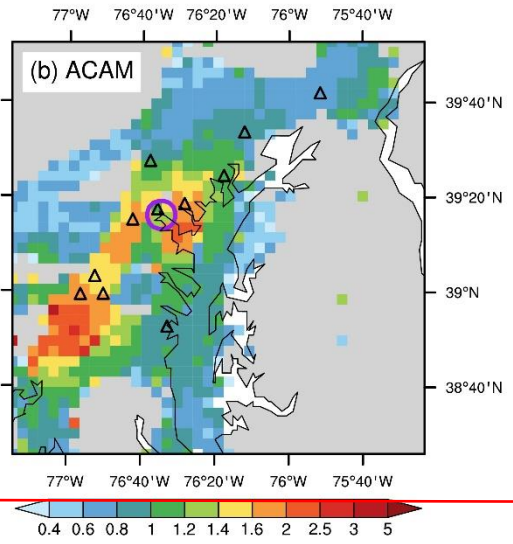
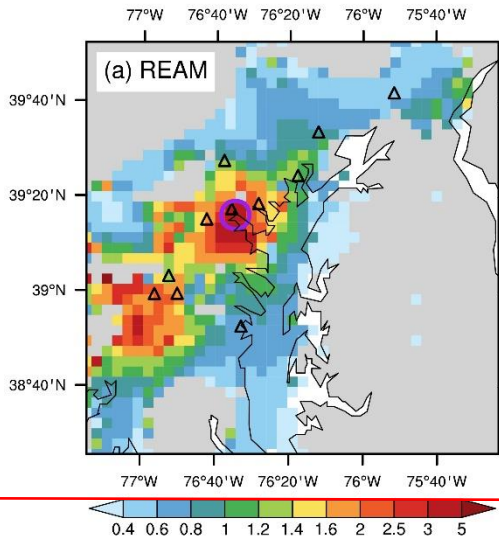


Figure 13. Comparisons of NO₂ (a, c) TVCDs and (b, d) surface concentrations over the 11 inland Pandora sites between the 4-km and 36-km REAM simulations on (a, b) weekdays and (c, d) weekends for July 2011. “REAM-36km” (black lines) denotes the 36-km REAM simulation results; “REAM-4km” (red lines) denotes the 4-km REAM simulation results; “4km-regrid” (blue lines) refers to the 36-km values by re-gridding the 4-km REAM simulation results into 36-km REAM grid cells. Error bars denote standard deviations.



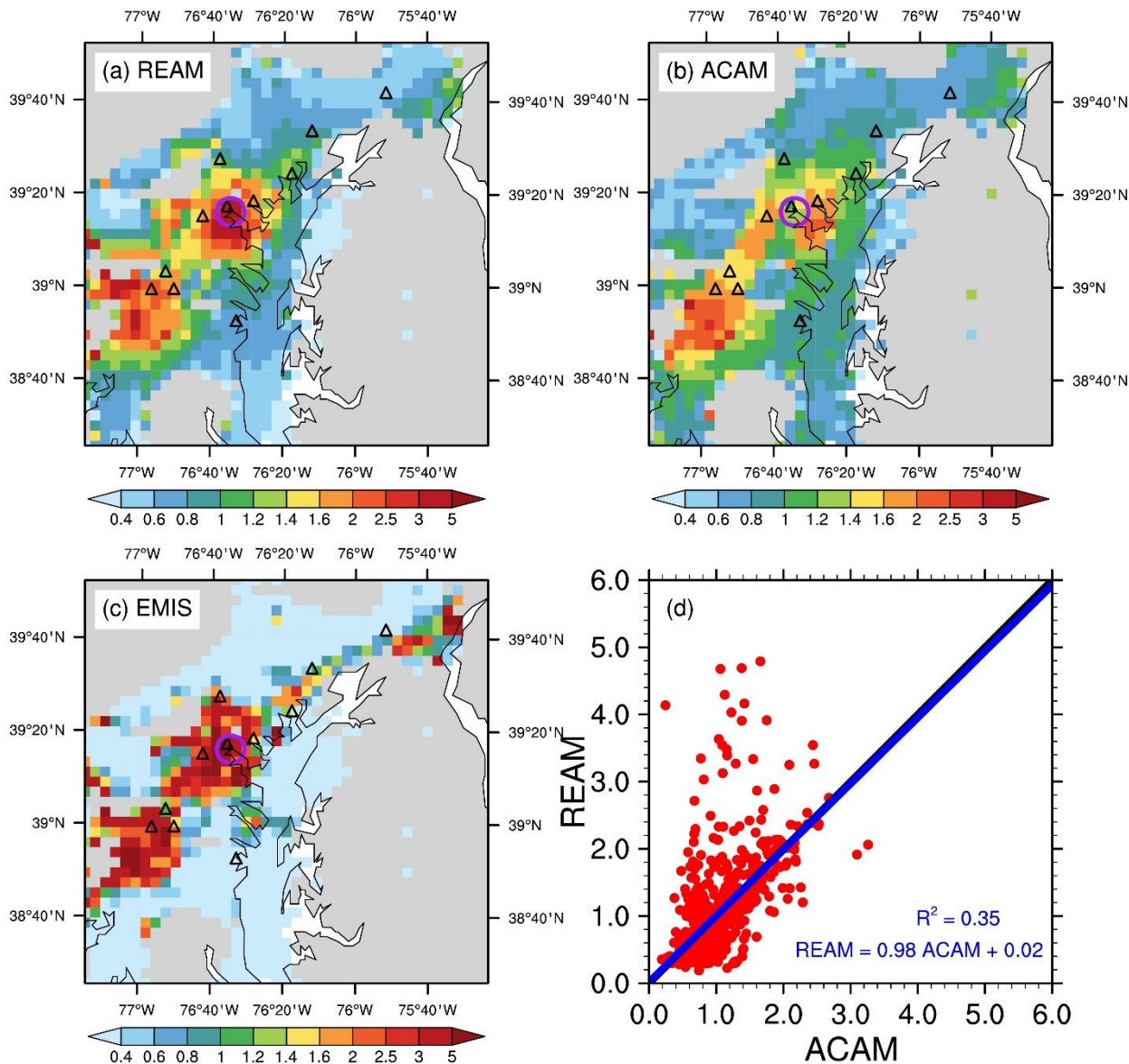


Figure 140. Distributions of the scaled mean (a) ACAM NO₂ VCDs below the UC-12 aircraft and (b) coincident 4-km REAM simulation results on weekdays in July 2011. (c), the distribution of the scaled NEI2011 NO_x emissions on weekdays. The purple circles denote a small region surrounded by high-NO_x emission pixels and with high NO₂ VCDs in the 4-km REAM but low NO₂ VCDs in ACAM. (d) is the scatter plot of the scaled ACAM and 4-km REAM NO₂ VCDs from (a) and (b). Here, we scale all values (VCDs and NO_x emissions) based on their corresponding domain averages. The domain averages of ACAM and coincident 4-km REAM NO₂ VCDs are 4.7 ± 2.0 and $4.65 \pm 3.2 \times 10^{15}$ molecules cm⁻², respectively.

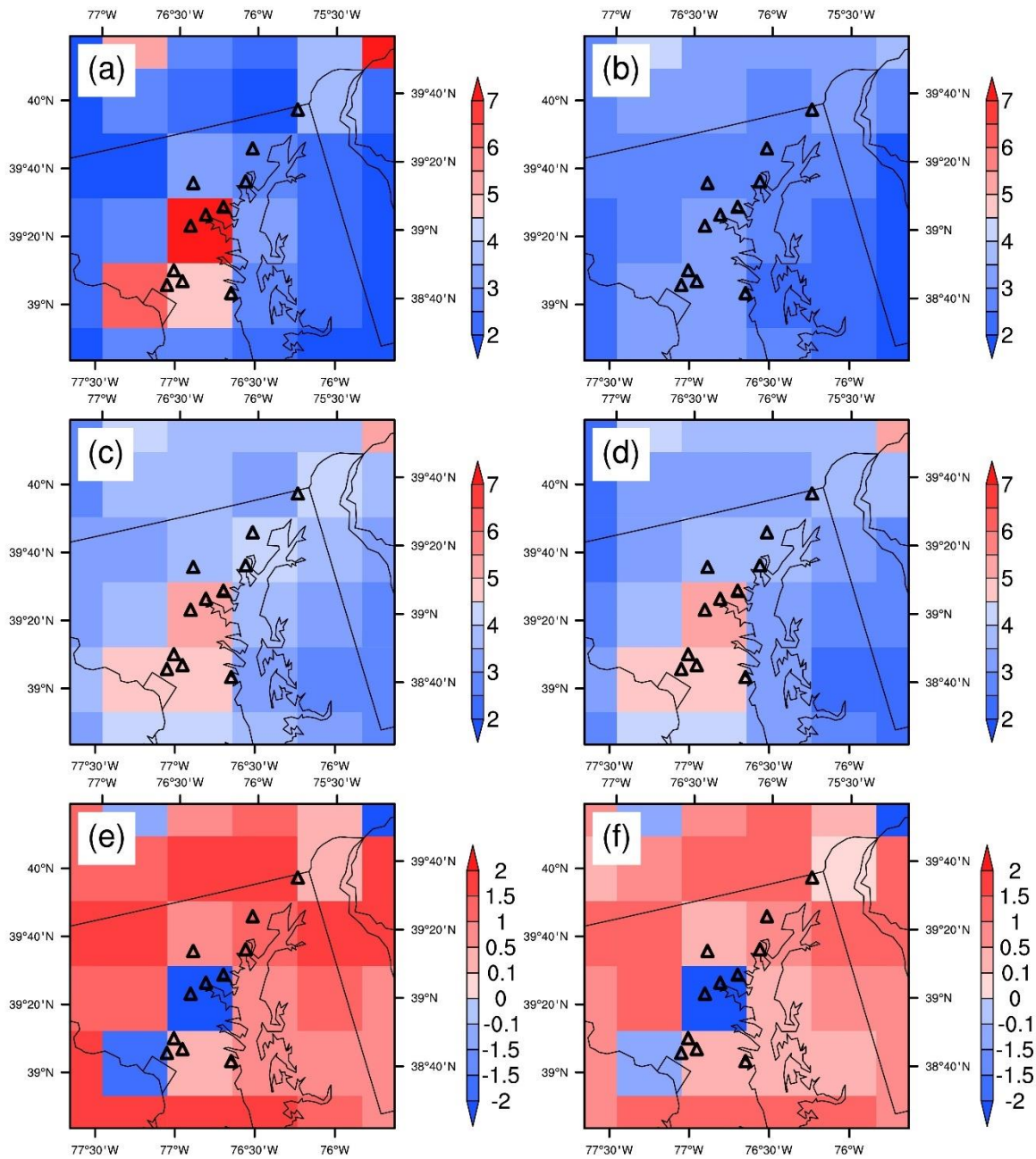


Figure 15. Distributions of weekday NO_2 TVCDs around the DISCOVER-AQ 2011 region for 13:30 LT in July 2011: (a) the 36-km REAM simulation results, (b) the NASA OMI product (OMNO2), (c) the KNMI OMI product, (d) the retrieved OMI NO_2 TVCDs by using the KNMI DOMINO algorithm with corresponding 36-km REAM vertical profiles, (e) the distribution of the NO_2 TVCD differences (c minus a) between KNMI OMI and 36-km REAM, and (f) the difference (d minus a) between retrieved OMI NO_2 TVCDs and the 36-km REAM results. The NO_2 TVCD unit is 10^{15} molecules cm^{-2} .

1 Supporting figures for

2 **Comprehensive evaluations of diurnal NO₂ measurements during**
3 **DISCOVER-AQ 2011: Effects of resolution dependent representation of NO_x**
4 **emissions**

5 Jianfeng Li^{1, a}, Yuhang Wang^{1*}, Ruixiong Zhang¹, Charles Smeltzer¹, Andrew Weinheimer², Jay
6 Herman³, K. Folkert Boersma^{4, 5}, Edward A. Celarier^{6, 7, b}, Russell W. Long⁸, James J. Szykman⁸,
7 Ruben Delgado³, Anne M. Thompson⁶, Travis N. Knepp^{9, 10}, Lok N Lamsal⁶, Scott J Janz⁶,
8 Matthew G Kowalewski⁶, Xiong Liu¹¹, Caroline R. Nowlan¹¹

9 ¹School of Earth and Atmospheric Sciences, Georgia Institute of Technology, Atlanta, Georgia,
10 USA

11 ²National Center for Atmospheric Research, Boulder, Colorado, USA

12 ³University of Maryland Baltimore County JCET, Baltimore, Maryland, USA

13 ⁴Royal Netherlands Meteorological Institute, De Bilt, the Netherlands

14 ⁵Wageningen University, Meteorology and Air Quality Group, Wageningen, the Netherlands

15 ⁶NASA Goddard Space Flight Center, Greenbelt, Maryland, USA

16 ⁷Universities Space Research Association, Columbia, Maryland, USA

17 ⁸National Exposure Research Laboratory, Office of Research and Development, U.S.

18 Environmental Protection Agency, Research Triangle Park, NC, USA

19 ⁹NASA Langley Research Center, Virginia, USA

20 ¹⁰Science Systems and Applications, Inc., Hampton, Virginia, USA

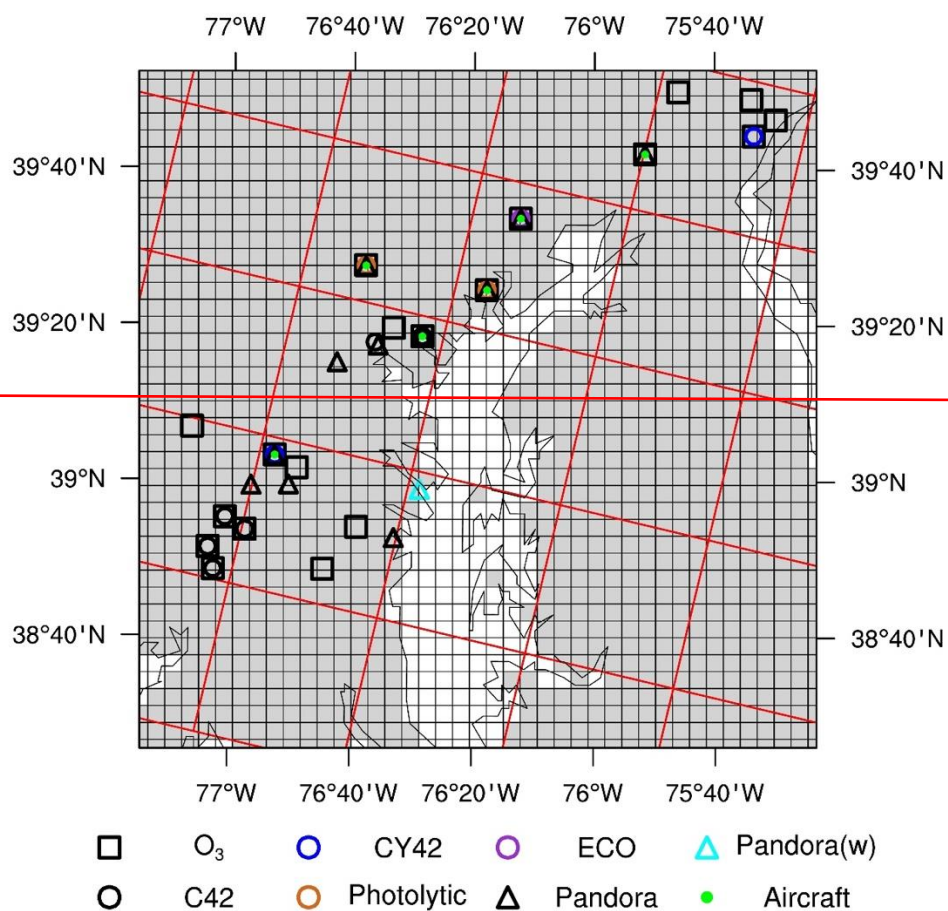
21 ¹¹Harvard-Smithsonian Center for Astrophysics, Cambridge, Massachusetts, USA

22
23 ^anow at: Atmospheric Sciences and Global Change Division, Pacific Northwest National
24 Laboratory, Richland, Washington, USA

25 ^bnow at: Digital Spec, Tyson's Corner, VA, USA

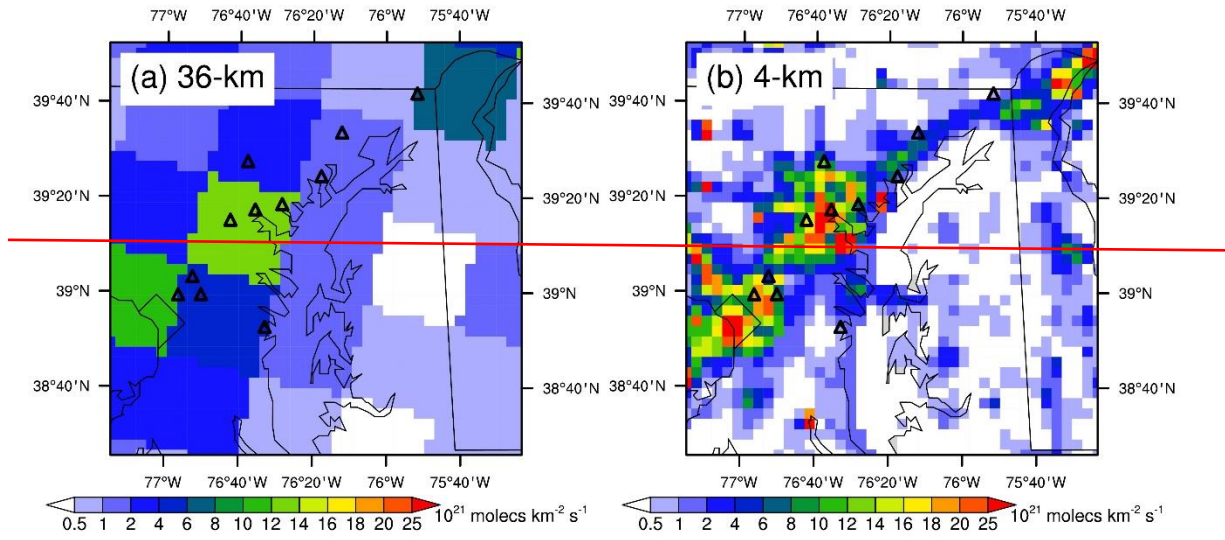
26 * *Correspondence to* Yuhang Wang (yuhang.wang@eas.gatech.edu)

27



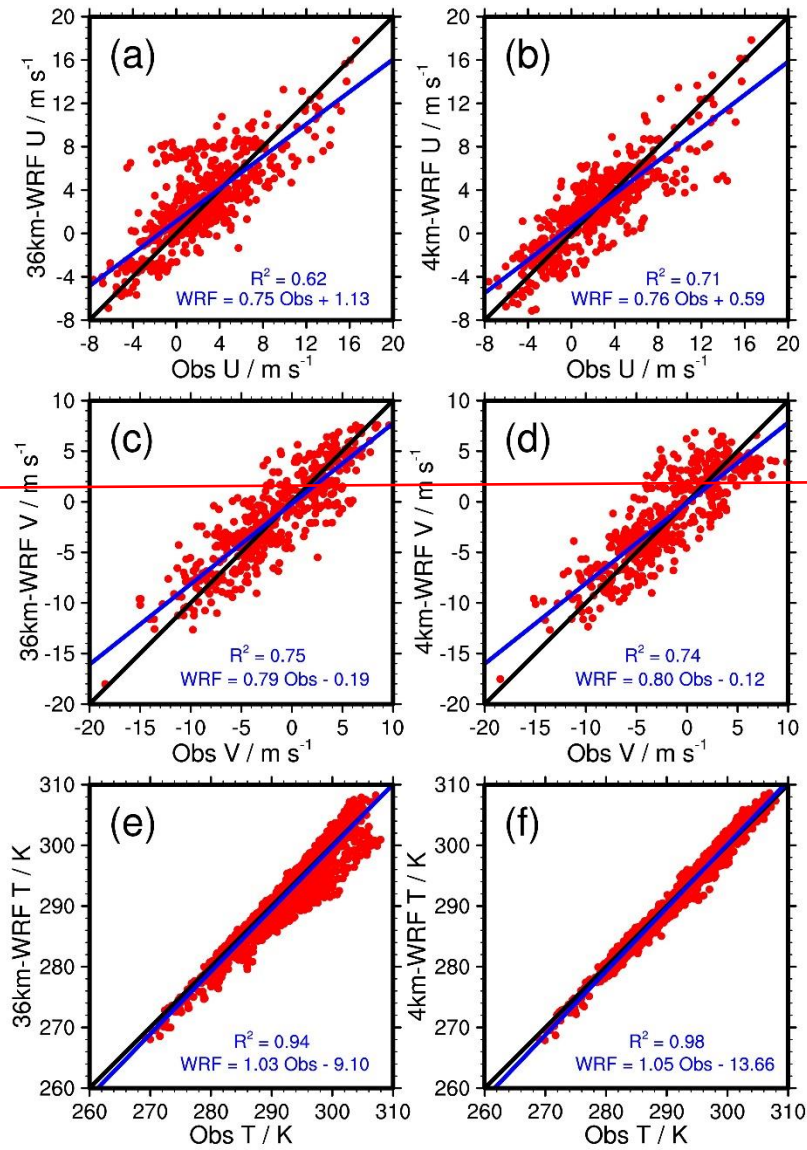
28
 29
 30
 31
 32
 33
 34
 35
 36
 37
 38
 39

Figure S1. The locations of surface and P-3B aircraft observations during the DISCOVER AQ 2011 campaign. We mark the 36 km REAM grid cells with red lines and the 4 km REAM grid cells with black lines. Gray shading denotes land surface in the nested 4 km WRF domain, while white denotes ocean/water surface. Black squares denote surface O₃ observation sites. Circles denote surface NO₂ observation sites, and their colors denote different measurement instruments: blue for the Thermo Electron 42C-Y NO_y analyzer, dark orchid for the Ecotech Model 9841/9843 T-NO_y analyzers, black for the Thermo Model 42C NO_x analyzer, and chocolate for the Teledyne API model 200eup photolytic NO_x analyzer. Triangles denote Pandora sites, and the cyan triangle denotes a Pandora site (USNA) on a ship. Green dots denote the inland P-3B aircraft spiral locations.



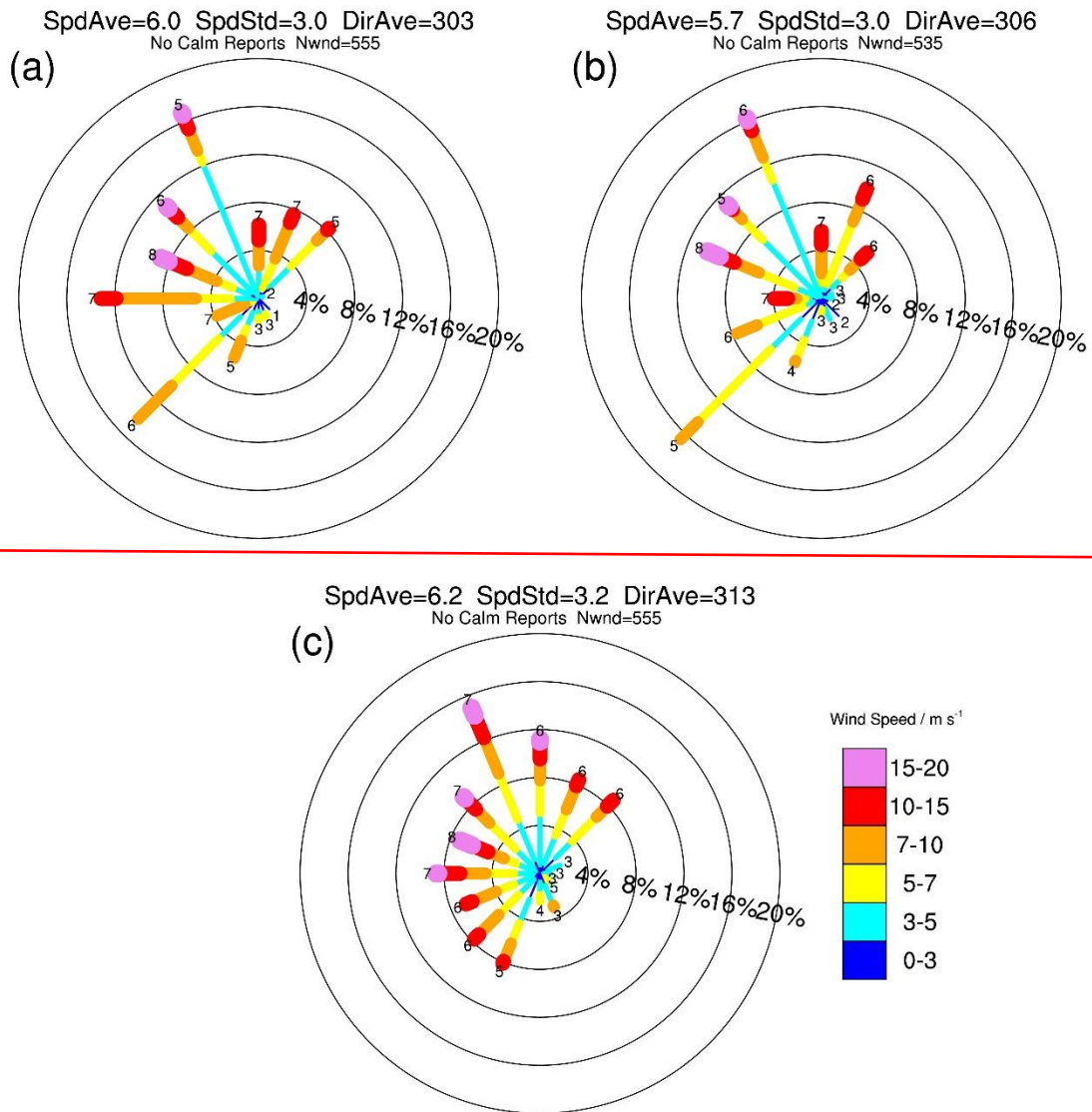
40
41
42
43
44

Figure S2. Distributions of NO_x emissions for the (a) 36 km and (b) 4 km REAM simulations. Here NO_x emissions refer to the mean values ($\text{molecules km}^{-2} \text{s}^{-1}$) in one week (Monday – Sunday).

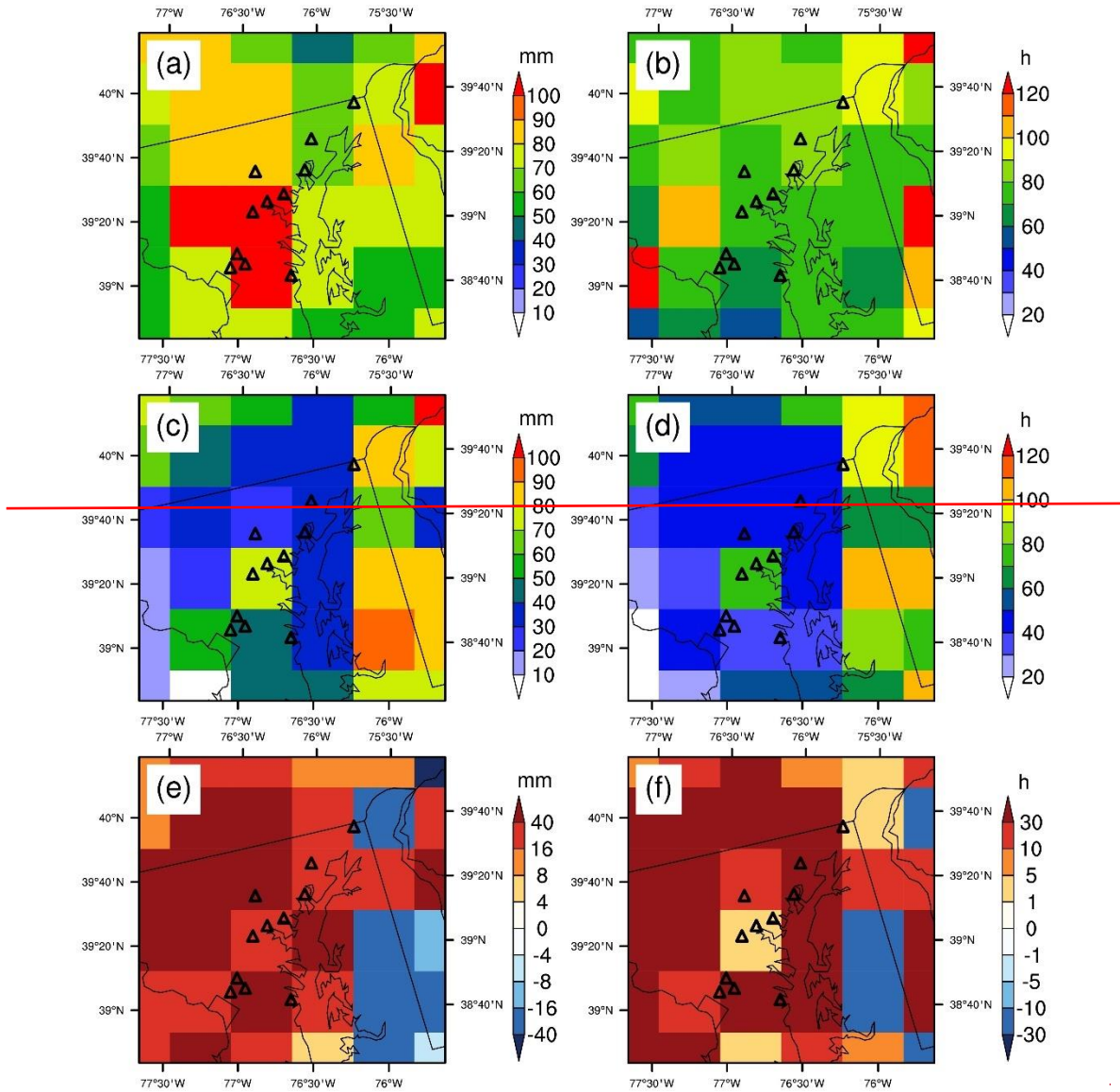


45
 46
 47
 48
 49
 50
 51
 52
 53
 54

Figure S3. Comparisons of (a, b) U wind, (c, d) V wind, and (e, f) temperature (T) between P-3B spirals and coincident WRF simulation results in July 2011. For P-3B observations, we derive U wind and V wind from wind speed and wind direction (Figure S4), which were measured via a Honeywell INS sensor. The accuracies of P-3B wind speed and wind direction are 1 m s^{-1} and $\pm 5^\circ$, respectively. Temperature from P-3B was measured by using a Rosemount model 102 sensor with an accuracy of $\pm 0.2^\circ\text{C}$. The left panel is for comparisons between P-3B and the 36 km WRF simulation, and the right panel is for comparisons between P-3B and the nested 4 km WRF simulation. WRF wind components have been rotated to earth coordinates.

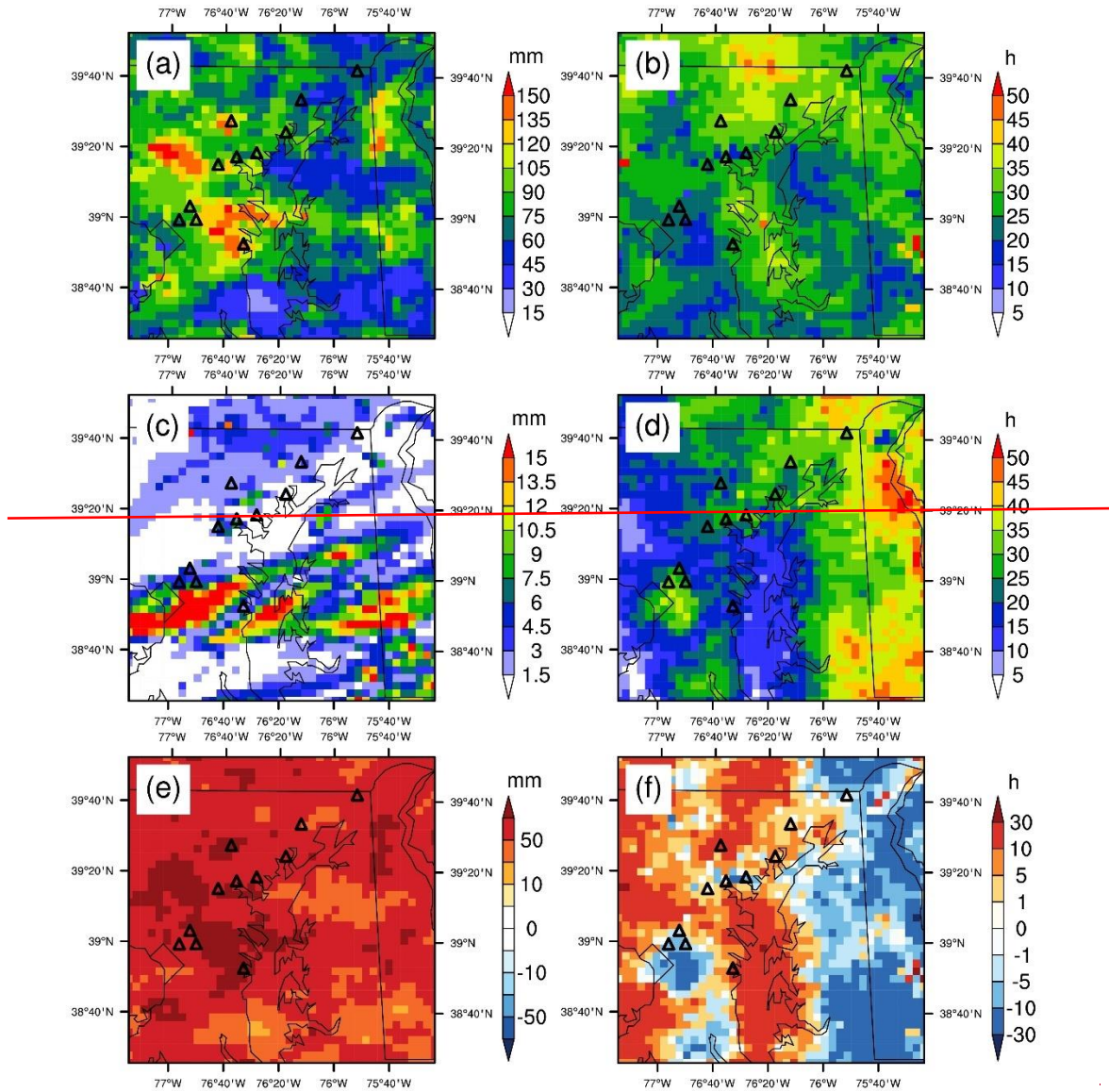


55
 56 **Figure S4.** Wind roses for P-3B observations and coincident WRF simulation results in July
 57 2011, (a) for the 36 km WRF simulation, (b) for the nested 4 km WRF simulation, and (c) for P-
 58 3B observations. WRF wind components have been rotated to earth coordinates. “SpdAve”
 59 denotes the average of wind speed, “SpdStd” denotes the standard deviation of wind speed, and
 60 “DirAve” denotes wind direction derived from averaged U-wind and V-wind.
 61



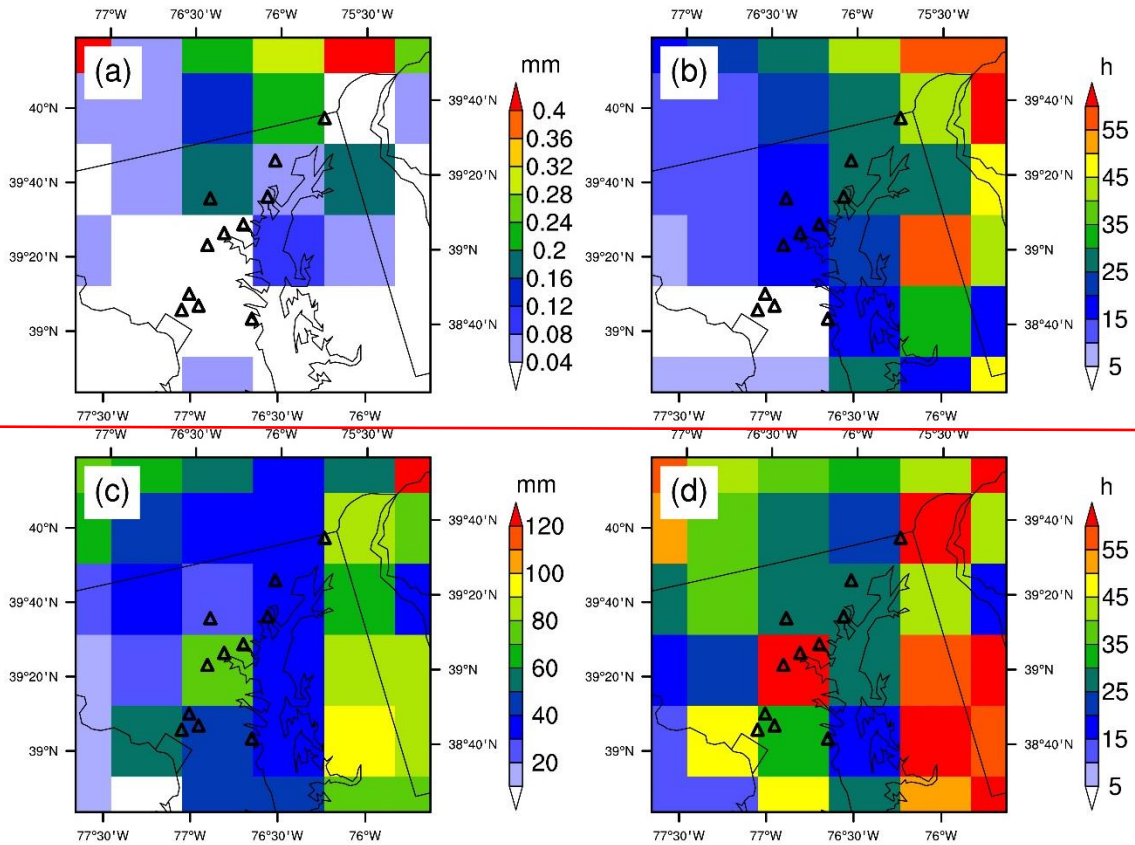
62
 63
 64
 65
 66
 67
 68
 69

Figure S5. Distributions of (a, c) precipitation amounts and (b, d) precipitation durations in July 2011 for (a, b) Stage IV and (c, d) the 36 km WRF simulation. (e) and (f) are the differences in precipitation amount and precipitation duration between Stage IV and the 36 km WRF simulation. The original resolution of Stage IV is about 4 km over polar stereographic grids, and we regrid the dataset to the 36 km WRF pixels. Triangles denote the inland Pandora sites in Figure S1.



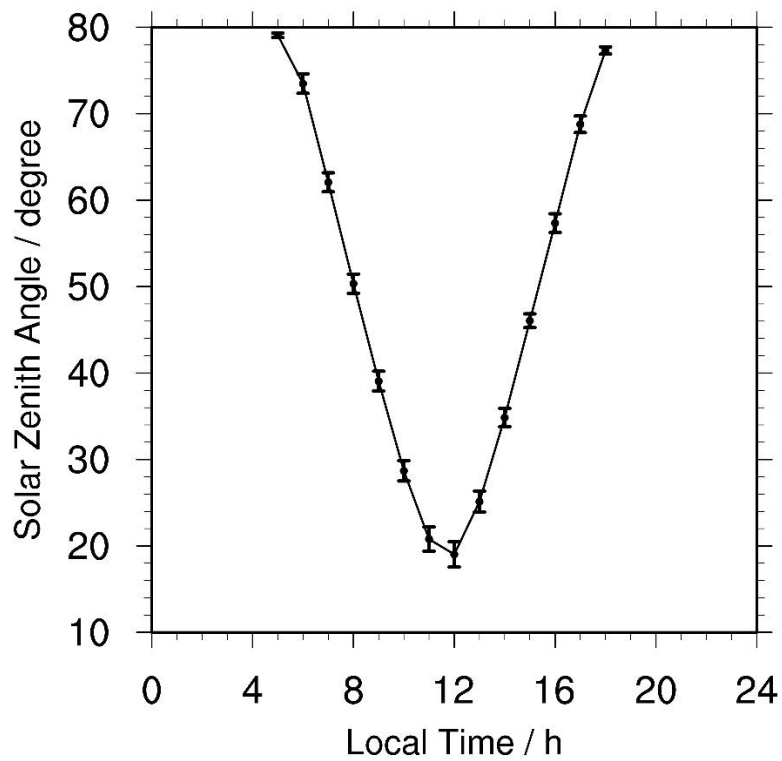
70
71
72
73
74
75
76
77
78

Figure S6. Distributions of (a, c) precipitation amounts and (b, d) precipitation durations in July 2011 for (a, b) Stage IV and (c, d) the nested 4 km WRF simulation. (e) and (f) stand for the differences in precipitation amount and precipitation duration between Stage IV and the nested 4 km WRF simulation. The original resolution of Stage IV is about 4 km over polar stereographic grids, and we regrid the dataset to the nested 4 km WRF pixels. Due to significantly lower precipitation amounts in the nested 4 km WRF simulation, we use different color bars for WRF and Stage IV data. Triangles denote the inland Pandora sites in Figure S1.



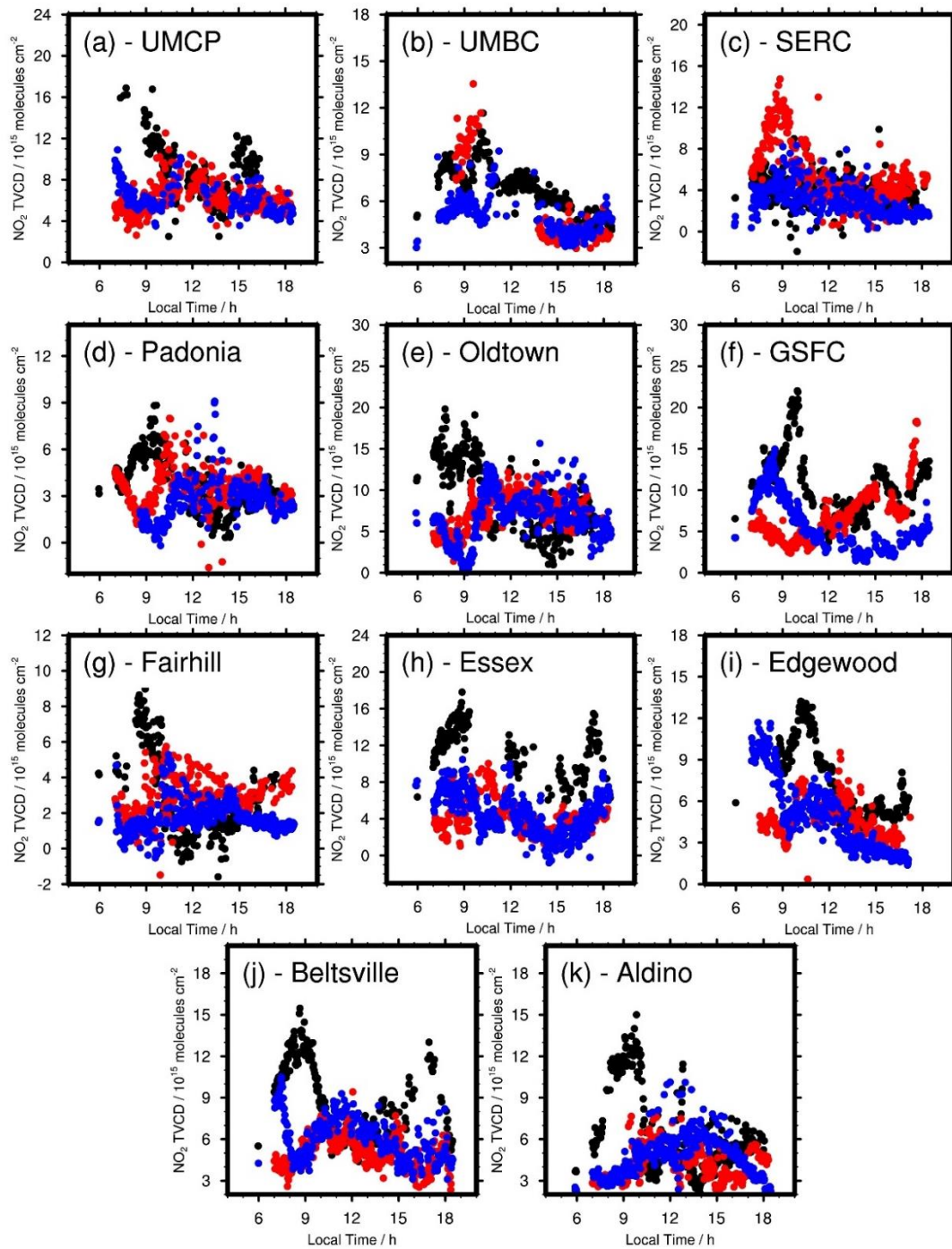
79
80
81
82
83
84

Figure S7. Distributions of (a, b) large-scale and (c, d) convective precipitation (a, c) amounts and (b, d) durations in July 2011 for the 36-km WRF simulation. Due to significantly lower large-scale precipitation amounts compared to convective precipitation, we use different color bars for them. Triangles denote the inland Pandora sites in Figure S1.



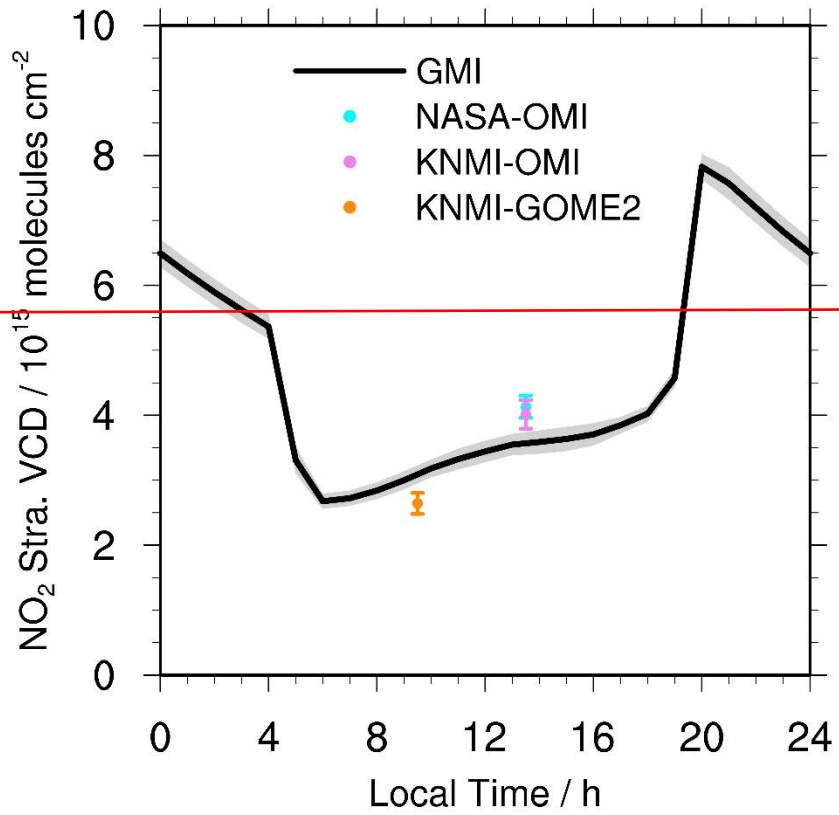
85
86
87
88
89

Figure S18. Diurnal variations of the solar zenith angles of Pandora measurements in July 2011. Here we use monthly averages of the 11 inland Pandora sites (Table S1 and Figure S1). Error bars denote standard deviations.

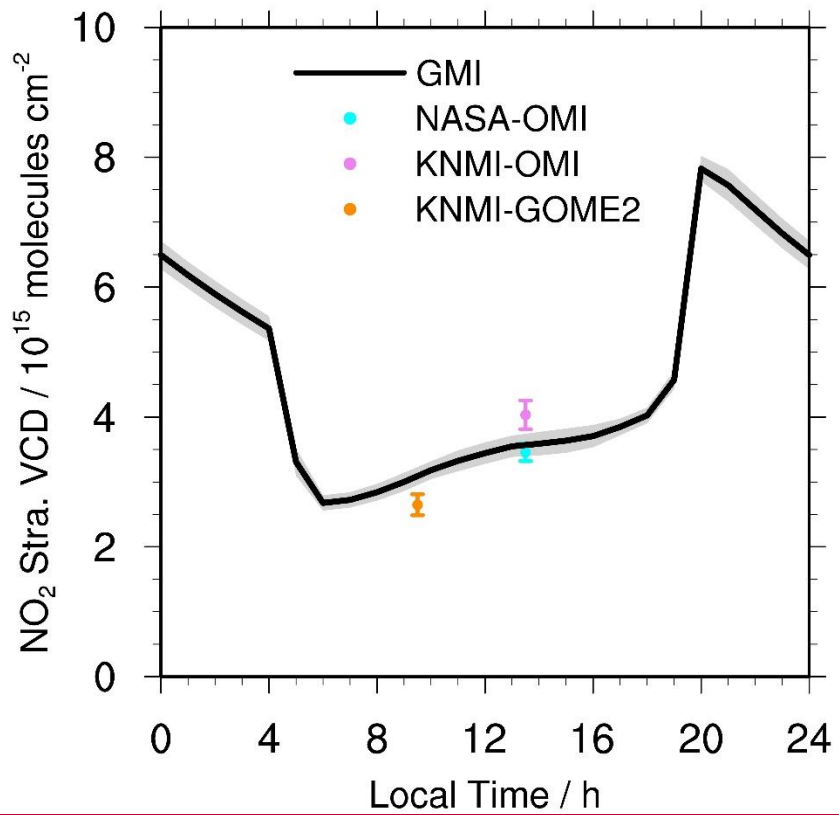


● 07/16/2011
 ● 07/18/2011
 ● 07/27/2011

90 **Figure S29.** Daily variations of Pandora NO_2 TVCDs at the 11 inland sites for three randomly
 91 selected days in July 2011. Blue dots denote Pandora measurements on July 16, 2011 (Saturday),
 92 black dots denote July 18, 2011 (Monday), and red dots denote July 27, 2011 (Wednesday). Here
 93 Pandora NO_2 TVCDs are calculated by subtracting stratospheric NO_2 VCDs from Pandora total
 94 NO_2 VCDs. See the main text for details.
 95
 96

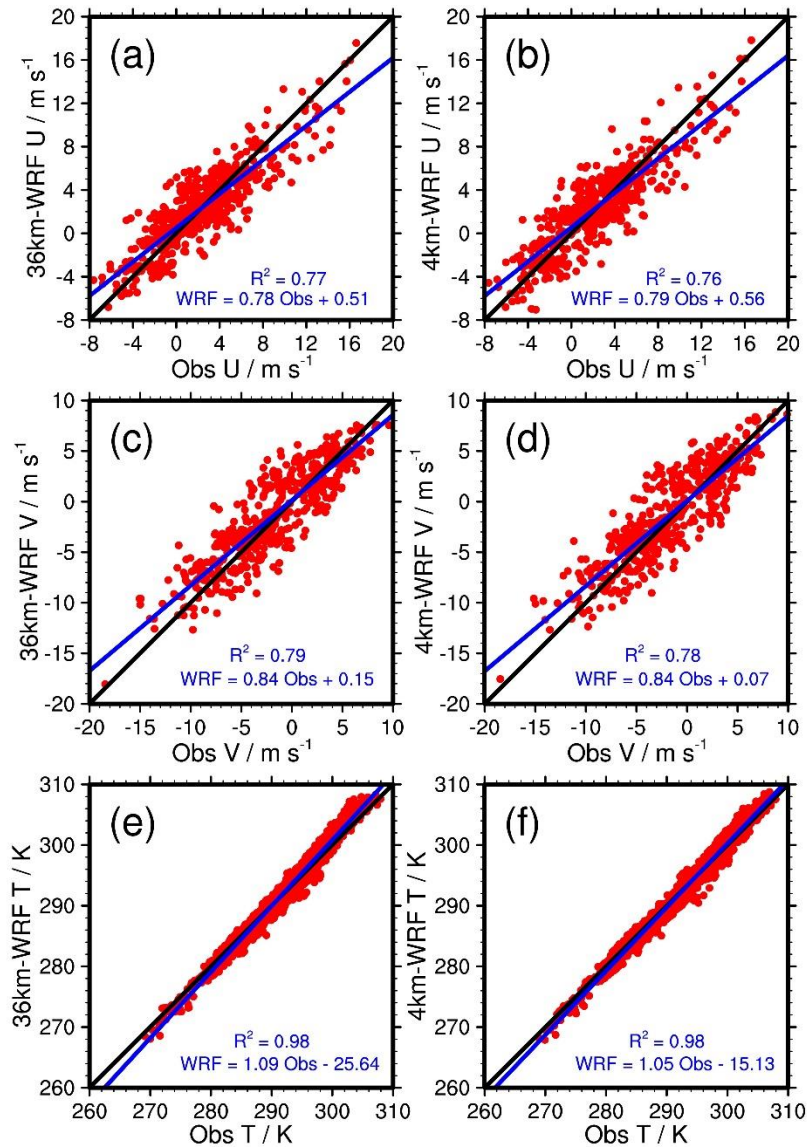


97



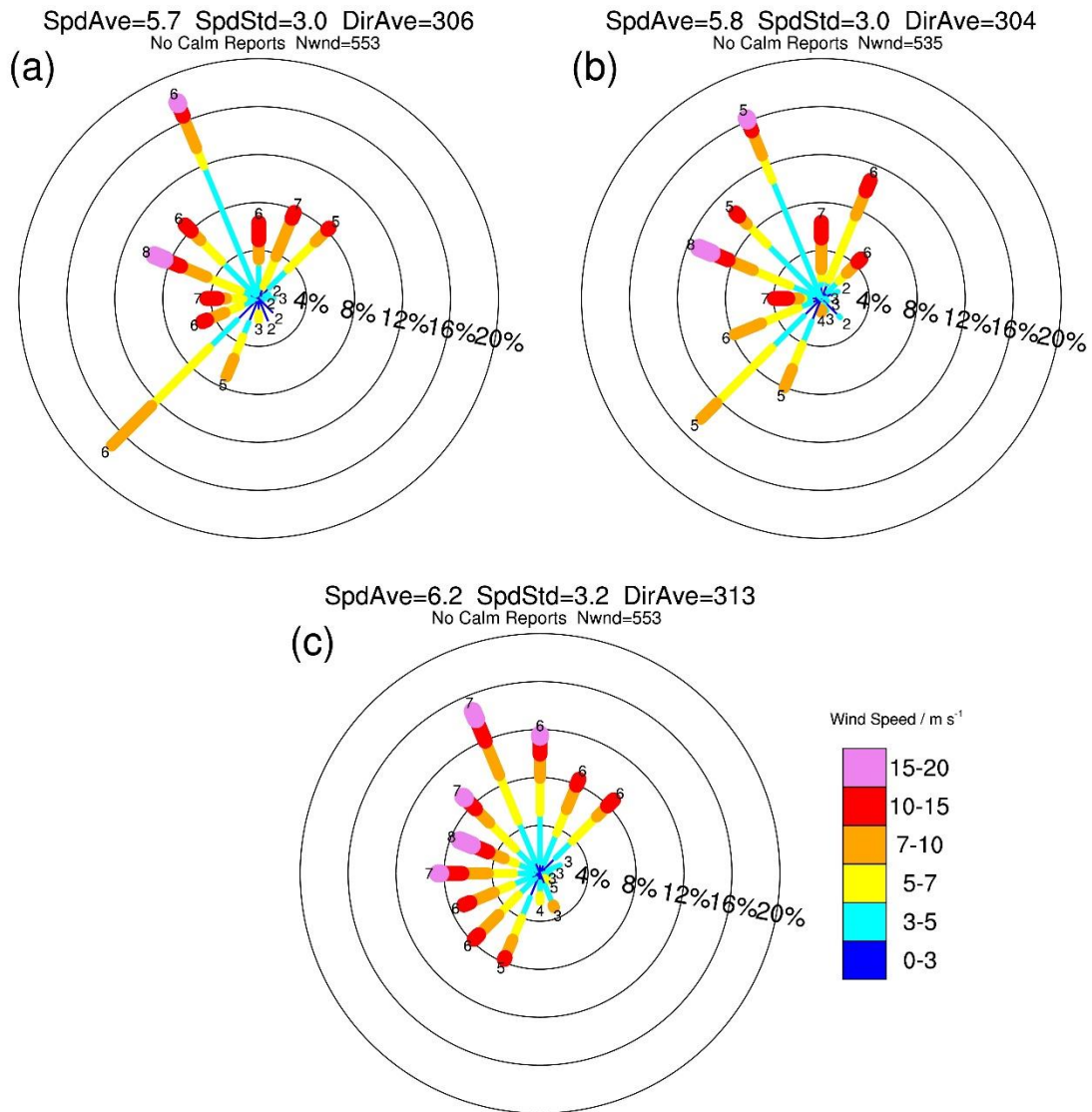
98

99 **Figure S310.** Stratospheric NO₂ VCD diurnal variations at the Greenbelt station in Maryland (39°
100 N, 76.89° W) from the GMI MERRA-2 1° × 1.25° simulation
101 (<https://gmi.gsfc.nasa.gov/merra2hindcast/>, last access: May 14, 2019) for July 2011, and the
102 corresponding satellite stratospheric NO₂ VCDs in the DISCOVER-AQ region (about 39.2° N,
103 76.3° W) (Figure S1). “NASA-OMI” denotes the OMI NO₂ VCDs from NASA, “KNMI-OMI”
104 denotes the OMI NO₂ VCDs from KNMI, and “KNMI-GOME2” denotes the GOME-2A NO₂
105 VCDs from KNMI. Gray shading and vertical bars denote the standard deviations of the GMI
106 results and satellite stratospheric VCD products, respectively.
107



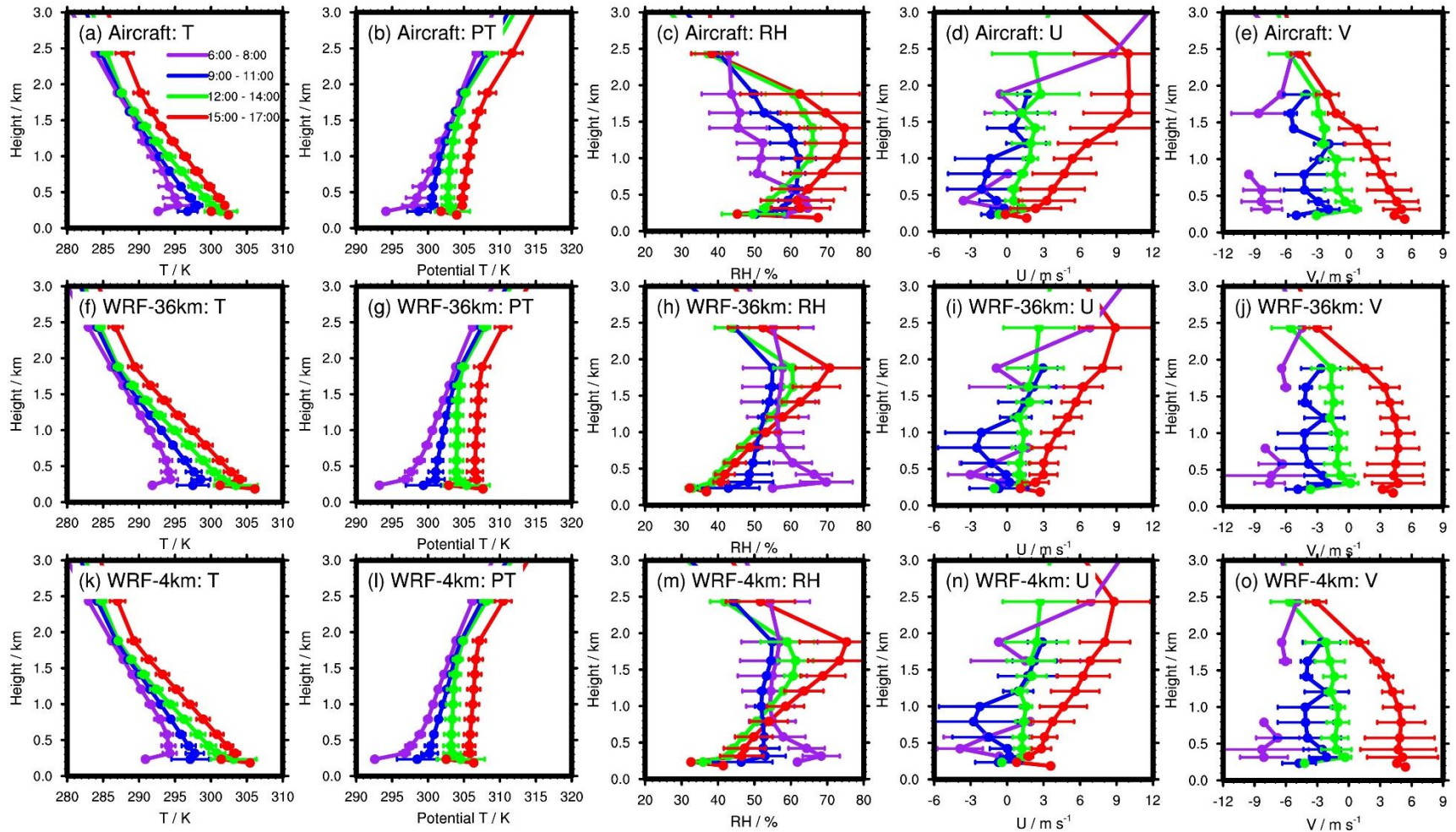
108
 109
 110
 111
 112
 113
 114
 115
 116
 117

Figure S4. Comparisons of (a, b) U wind, (c, d) V wind, and (e, f) temperature (T) between P-3B spirals and coincident WRF simulation results for July 2011. For the P-3B observations, we derive U and V wind from the observed wind speed and wind direction (Figure S5), which were measured via a Honeywell INS sensor. The accuracies of P-3B wind speed and wind direction are 1 m s^{-1} and $\pm 5^\circ$, respectively. Air temperature on P-3B was measured by using a Rosemount model 102 sensor with an accuracy of $\pm 0.2 \text{ }^\circ\text{C}$. The left panel is for comparisons between P-3B and the 36-km WRF simulation, and the right panel is for comparisons between P-3B and the nested 4-km WRF simulation. WRF wind components have been rotated to earth coordinates.



118
 119
 120
 121
 122
 123
 124

Figure S5. Wind roses for P-3B observations and coincident WRF simulation results for July 2011, (a) for the 36-km WRF simulation, (b) for the nested 4-km WRF simulation, and (c) for P-3B observations. WRF wind components have been rotated to earth coordinates. “SpdAve” denotes the average of wind speed, “SpdStd” denotes the standard deviation of wind speed, and “DirAve” denotes wind direction derived from averaged U-wind and V-wind.



125

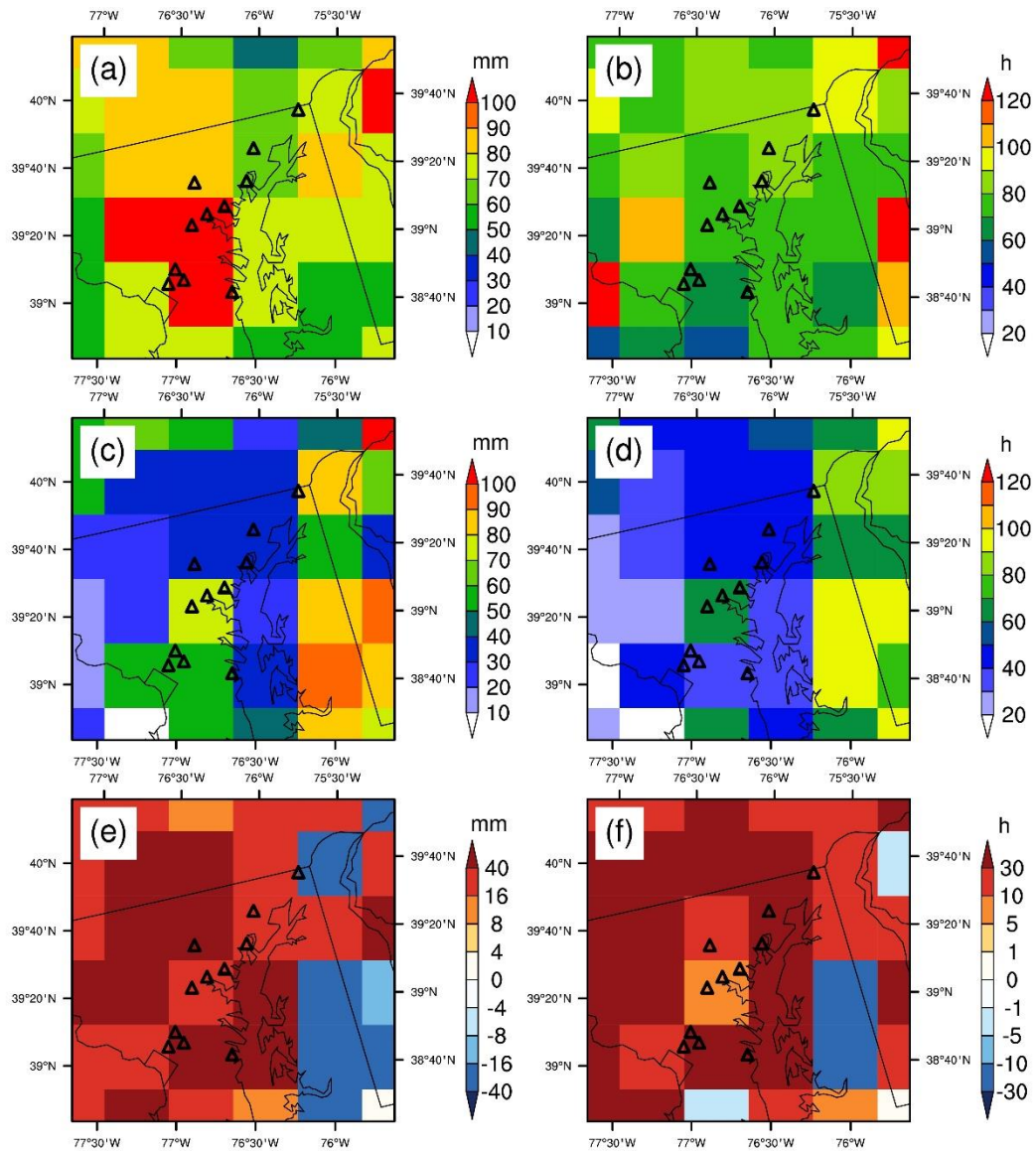
126

127

128

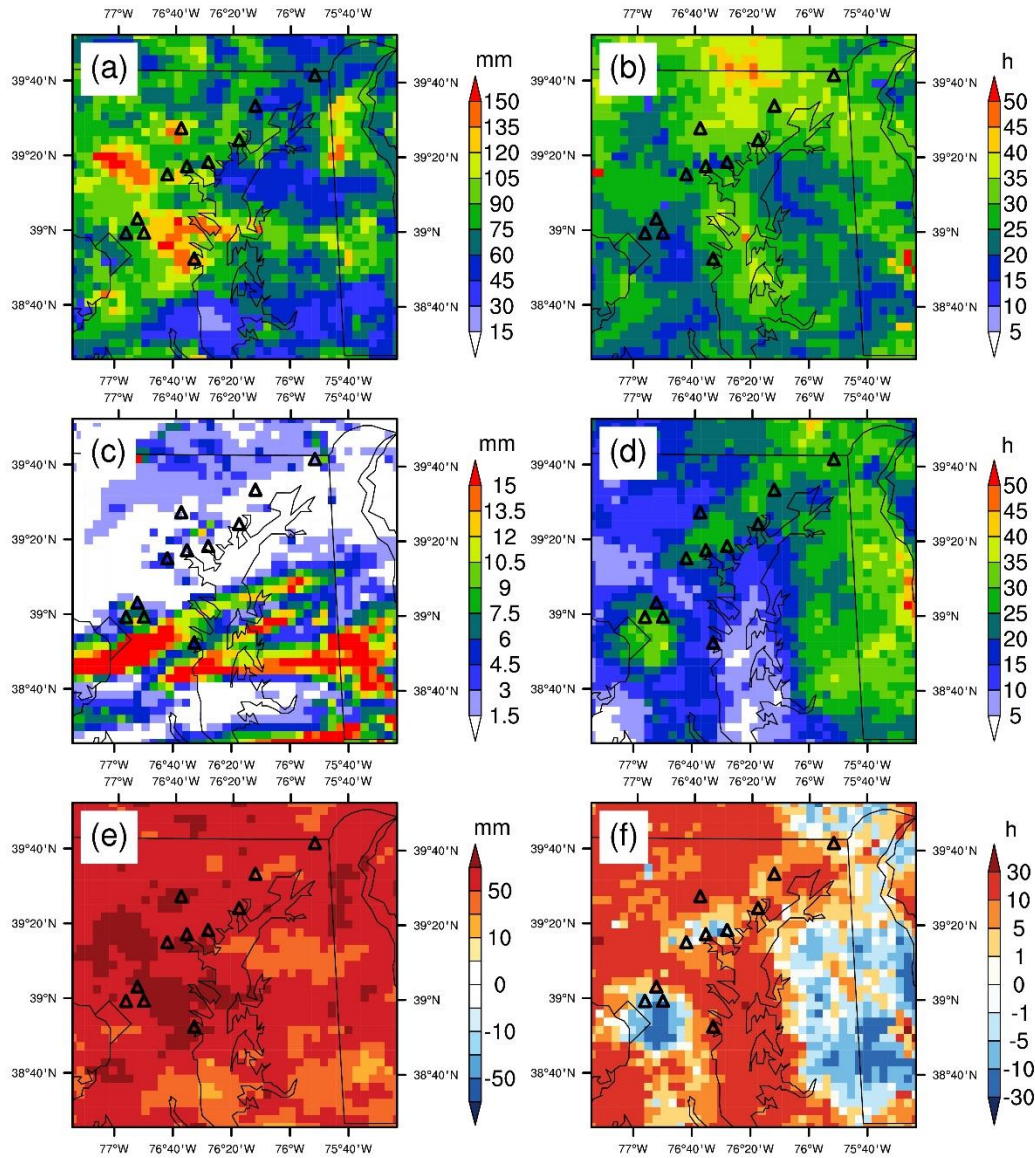
129

Figure S6. Temporal evolutions of vertical profiles for (a, f, k) temperature (T), (b, g, l) potential temperature (PT), (c, h, m) relative humidity (RH), (d, i, n) U-wind, and (e, j, o) V-wind below 3 km from the (a, b, c, d, e) P-3B aircraft and (f, g, h, i, j) 36-km and (k, l, m, n, o) nested 4-km WRF simulations during the DISCOVER-AQ campaign. Horizontal bars denote corresponding standard deviations. Purple lines denote 6:00 – 8:00 LT, blue lines for 9:00 – 11:00 LT, green lines for 12:00 – 14:00 LT, and red lines for 15:00 – 17:00 LT.



130
 131
 132
 133
 134
 135
 136
 137

Figure S7. Distributions of (a, c) precipitation amounts and (b, d) precipitation durations in July 2011 for (a, b) Stage IV and (c, d) the 36-km WRF simulation. (e) and (f) are the differences in precipitation amount and precipitation duration between Stage IV and the 36-km WRF simulation. The original resolution of Stage IV is about 4 km over polar stereographic grids, and we regrid the dataset to the 36-km WRF pixels. Triangles denote the inland Pandora sites in [Figure 1](#).



138

139

140

141

142

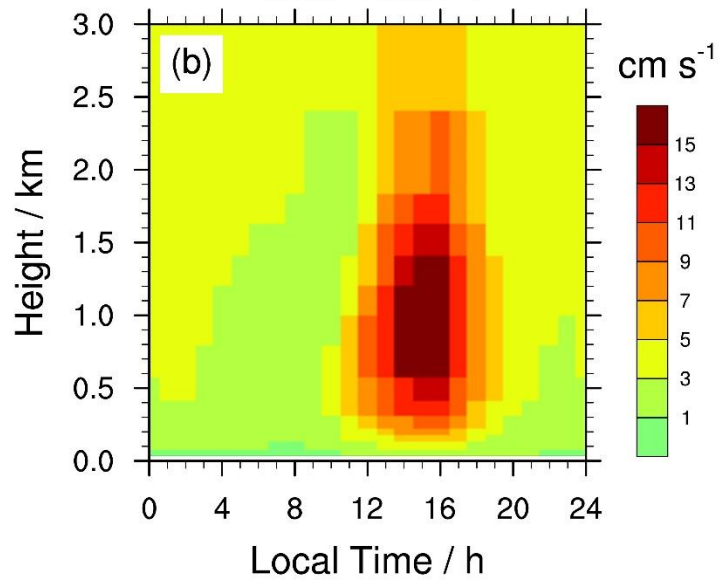
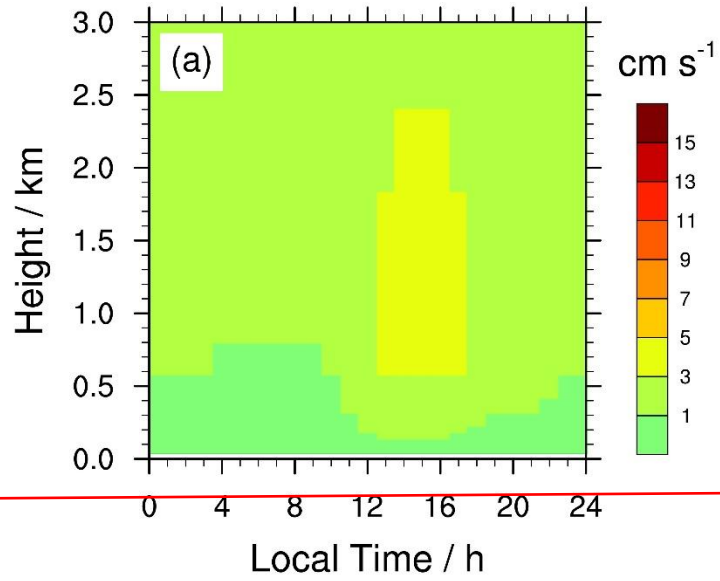
143

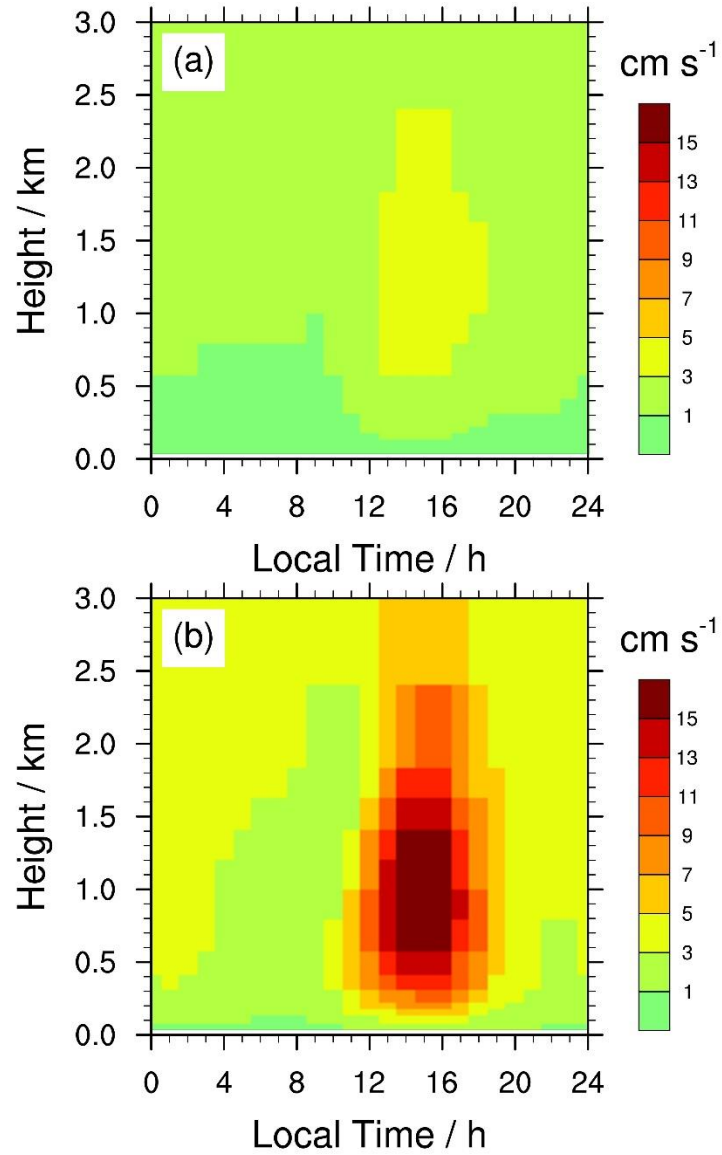
144

145

146

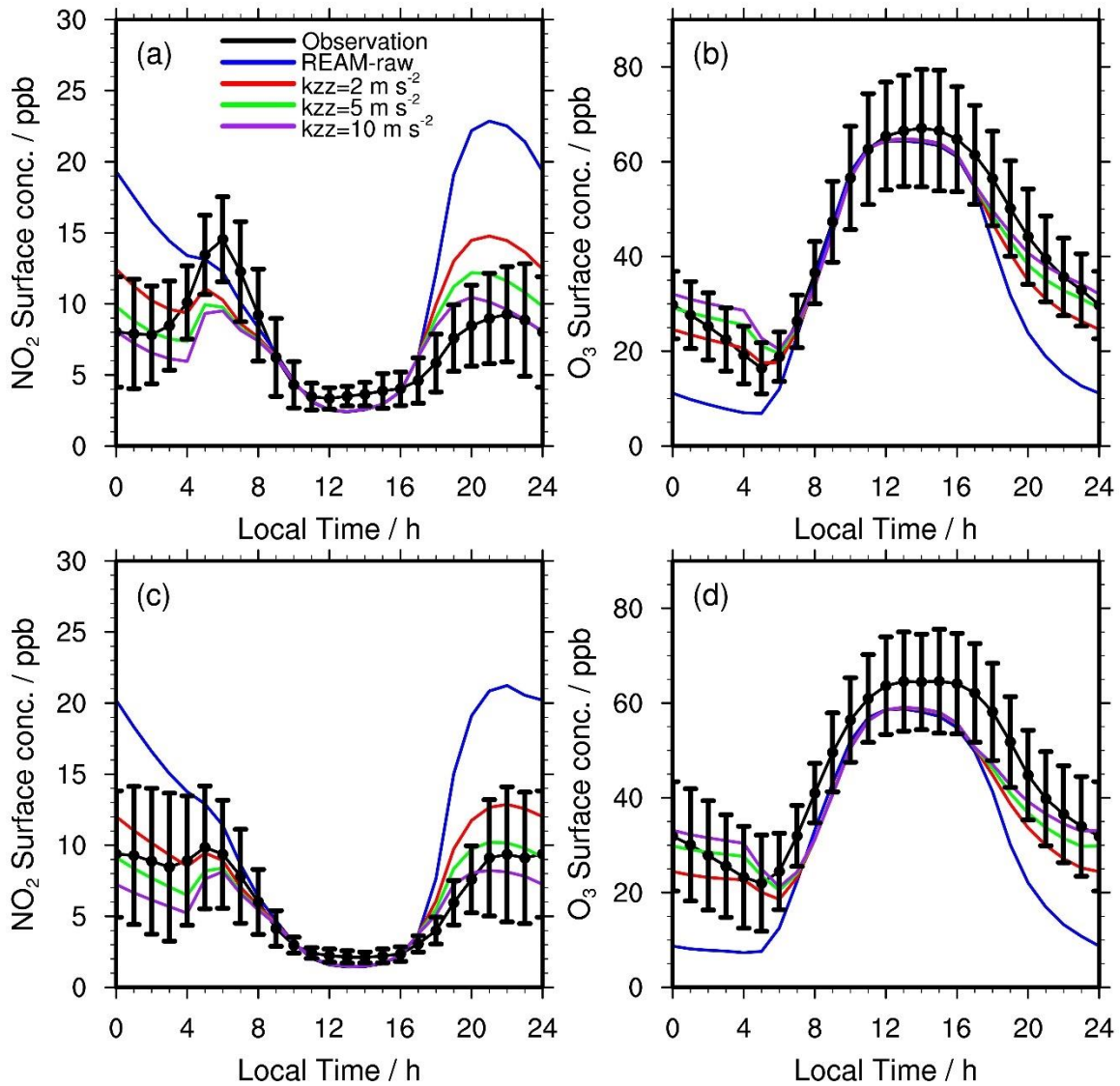
Figure S8. Distributions of (a, c) precipitation amounts and (b, d) precipitation durations in July 2011 for (a, b) Stage IV and (c, d) the nested 4-km WRF simulation. (e) and (f) stand for the differences in precipitation amount and precipitation duration between Stage IV and the nested 4-km WRF simulation. The original resolution of Stage IV is about 4 km over polar stereographic grids, and we regrid the dataset to the nested 4-km WRF pixels. Due to significantly lower precipitation amounts in the nested 4-km WRF simulation, we use different color bars for WRF and Stage IV data. Triangles denote the inland Pandora sites in Figure 1.





148
149
150
151

Figure S911. Diurnal variations of boundary-layer vertical velocities for the (a) 36-km and (b) nested 4-km WRF simulations in the DISCOVER-AQ region (Figure S1) for July 2011.



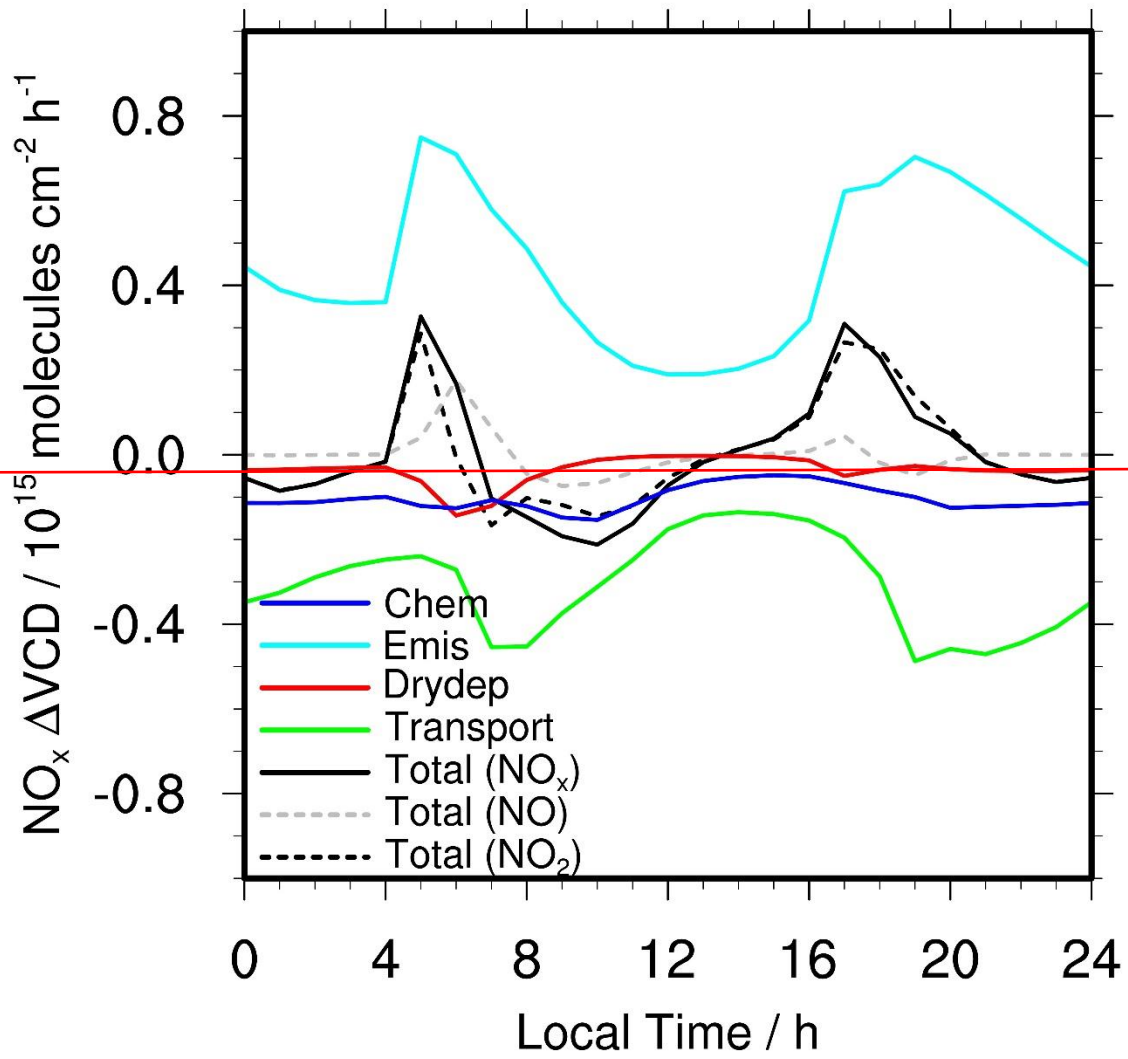
152

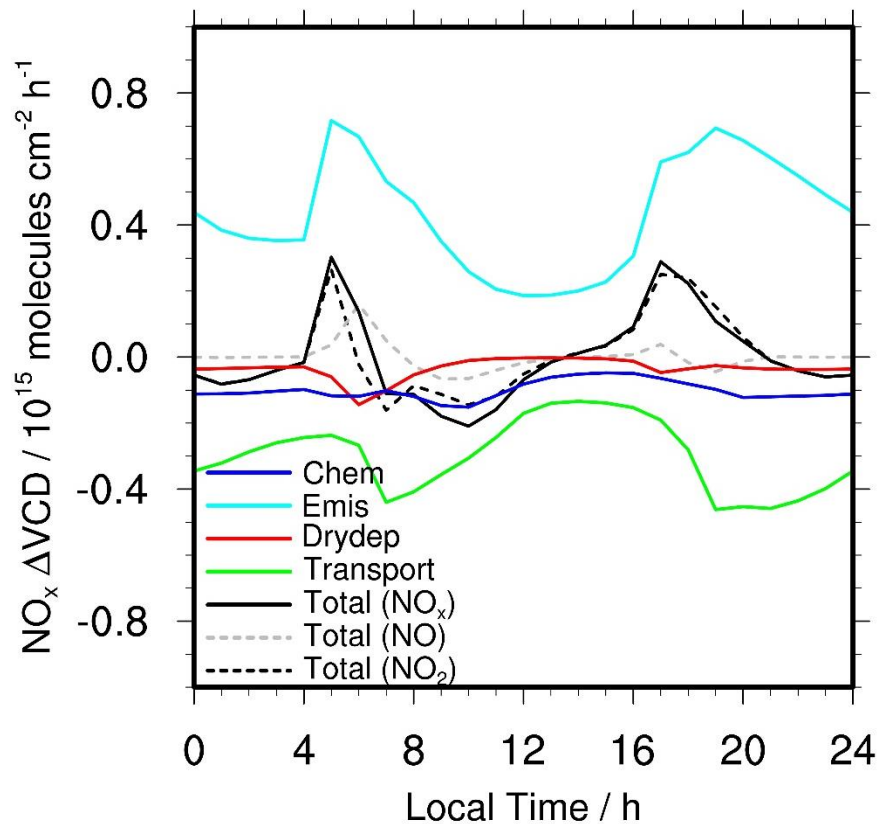
153

154

155

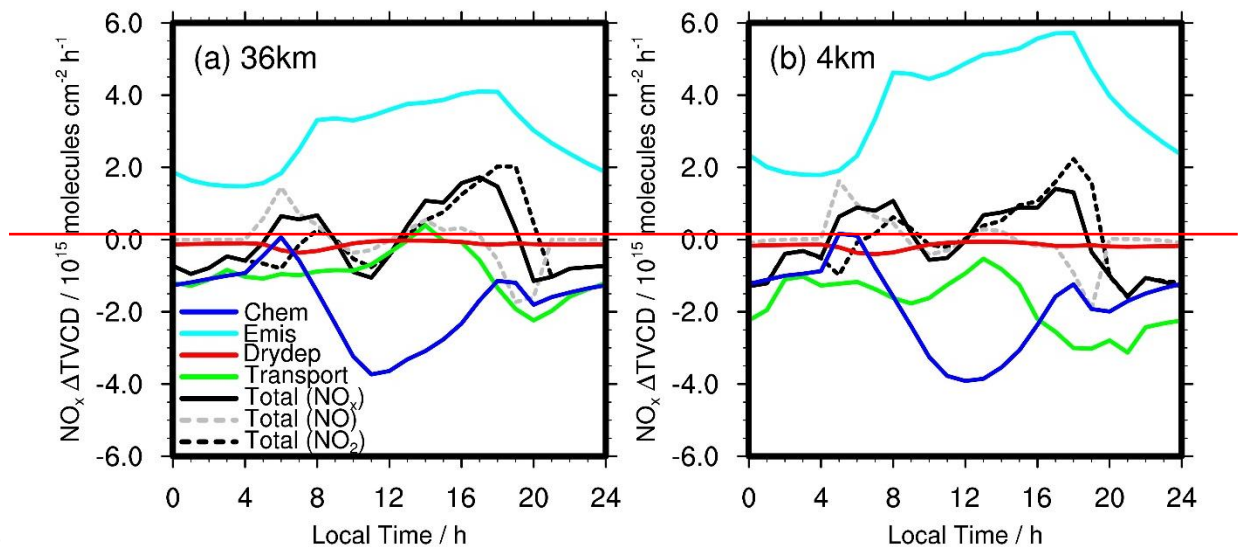
Figure S10. Similar as Figure 5 but with two additional REAM sensitivity tests with k_{zz} updated to 2 m s^{-2} or 10 m s^{-2} instead of 5 m s^{-2} following the approach mentioned in the main text.





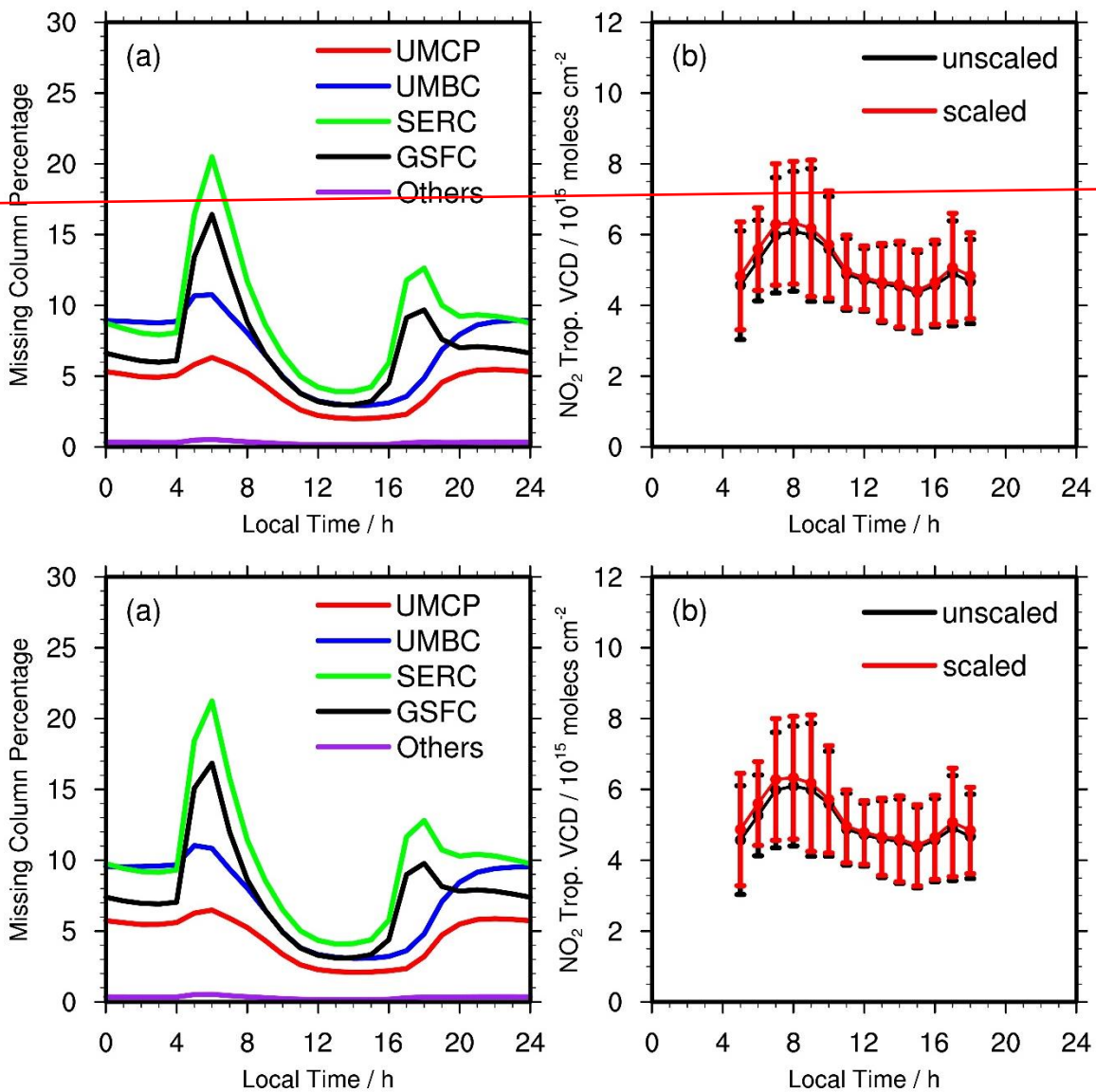
157

158 **Figure S112.** Contributions of emission, chemistry, transport, and dry deposition to NO_x VCD
 159 diurnal variations in the surface layer of the 36-km REAM simulation in the DISCOVER-AQ
 160 region on weekdays in July 2011. “Chem” refers to net NO_x chemistry production in the surface
 161 layer; “Emis” refers to NO_x emissions in the surface layer with the impact of vertical turbulent
 162 mixing; “Drydep” denotes NO_x dry depositions in the surface layer; “Transport” includes
 163 advection, turbulent mixing, lightning NO_x production, and wet deposition in the surface layer.
 164 “Total (NO_x)” is the hourly change of surface-layer NO_x VCDs ($\Delta(VCD) = VCD_{t+1} - VCD_t$).
 165 “Total (NO₂)” is the hourly change of surface-layer NO₂ VCDs, and “Total (NO)” is the hourly
 166 change of surface-layer NO VCDs.
 167



168
 169
 170
 171
 172
 173
 174
 175
 176

Figure S13. Contributions of emission, chemistry, transport, and dry deposition to NO_x -TVCD diurnal variations over the 11 inland Pandora sites (Table S1 and Figure S1) on weekdays in July 2011 for the (a) 36-km and (b) 4-km REAM simulations. “Chem” refers to net NO_x -chemistry production; “Emis” refers to NO_x -emissions; “Drydep” denotes NO_x -dry depositions; “Transport” includes advection, turbulent mixing, lightning NO_x production, and wet deposition. “Total (NO_x)” is the hourly change of NO_x -TVCDs ($\Delta(\text{TVCD}) = \text{TVCD}_{t+\Delta t} - \text{TVCD}_t$). “Total (NO_2)” is the hourly change of NO_2 -TVCDs, and “Total (NO)” is the hourly change of NO -TVCDs.

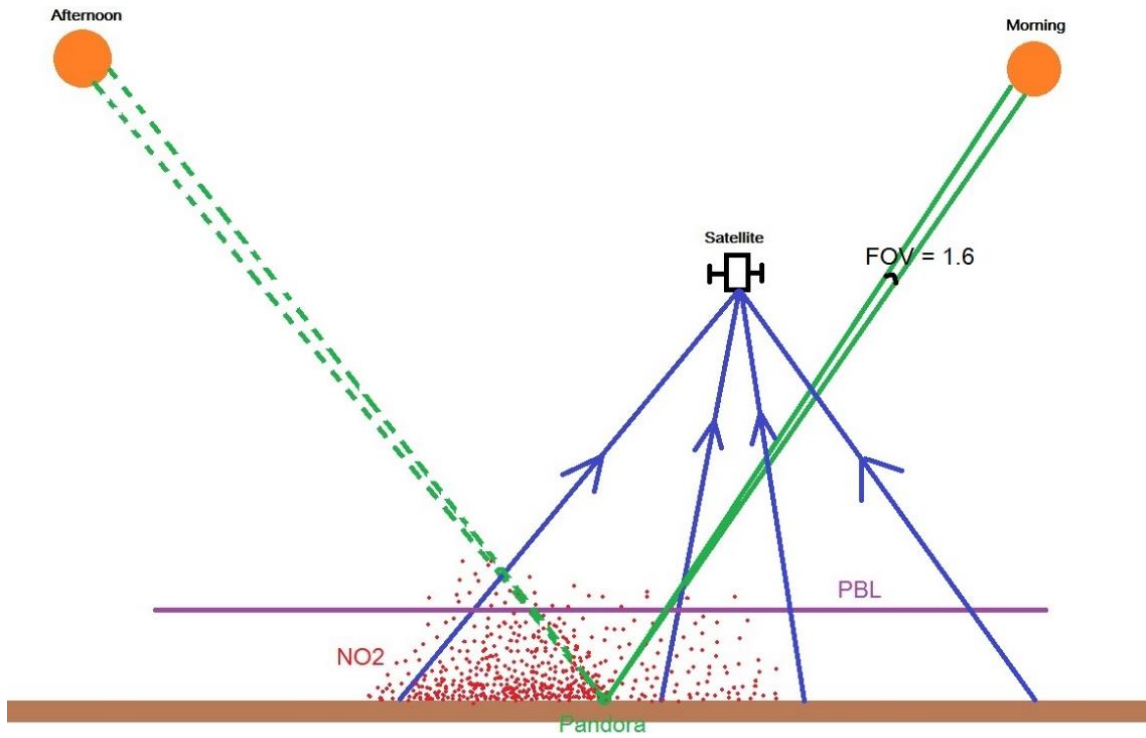


177

178

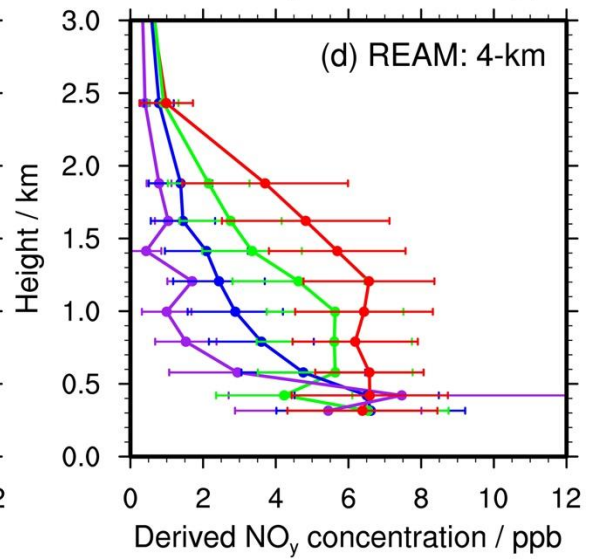
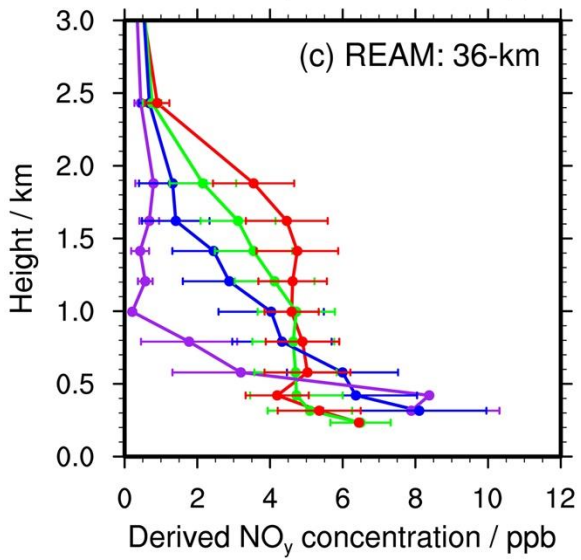
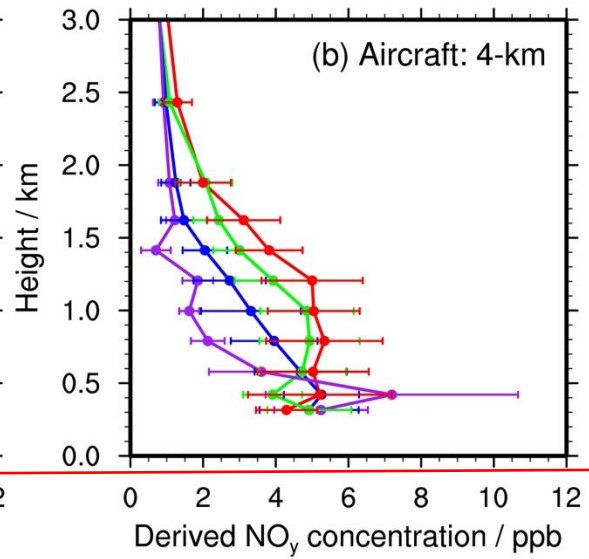
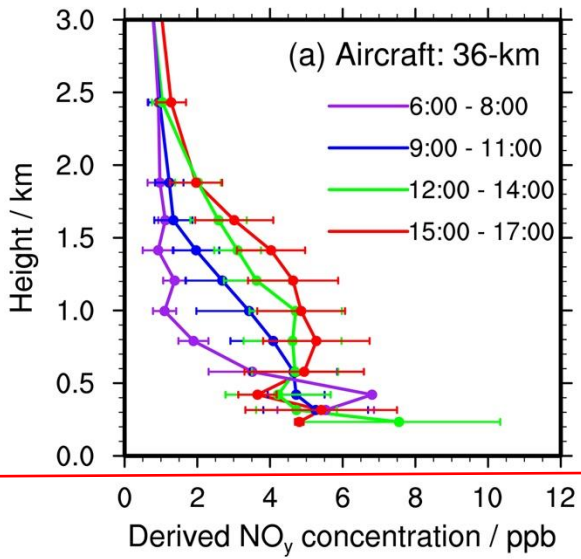
179 **Figure S124.** (a) Percentages of NO_2 VCDs below the heights of Pandora instruments in July
 180 2011 based on 36-km REAM results; (b) the comparison between original Pandora TVCDs
 181 (“unscaled”) and updated Pandora TVCDs (“scaled”) with the inclusion of VCDs below the
 182 Pandora instruments. Here we use monthly averages in July 2011. Error bars in (b) denote
 183 standard deviations.

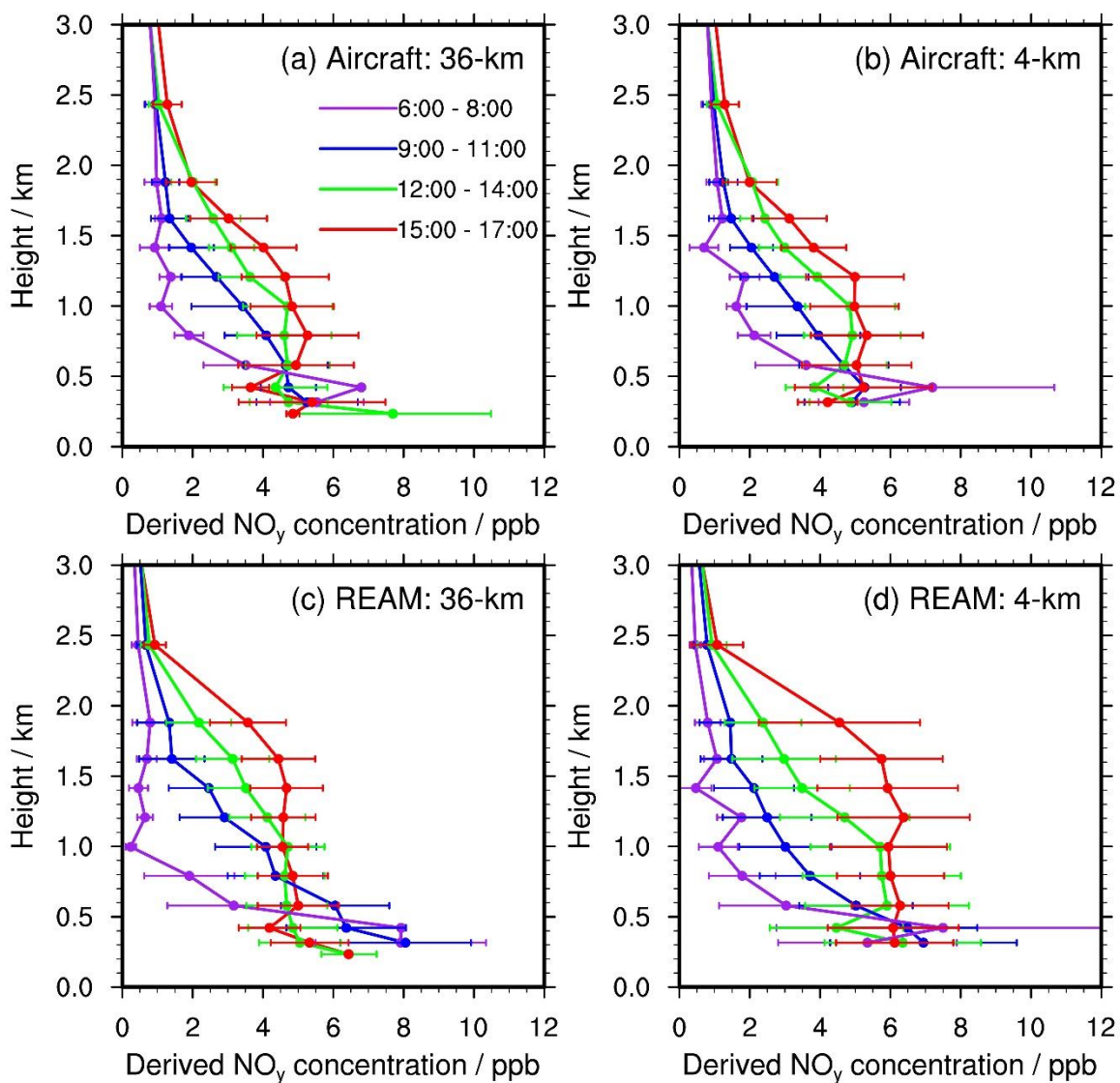
184



185
 186
 187
 188
 189
 190

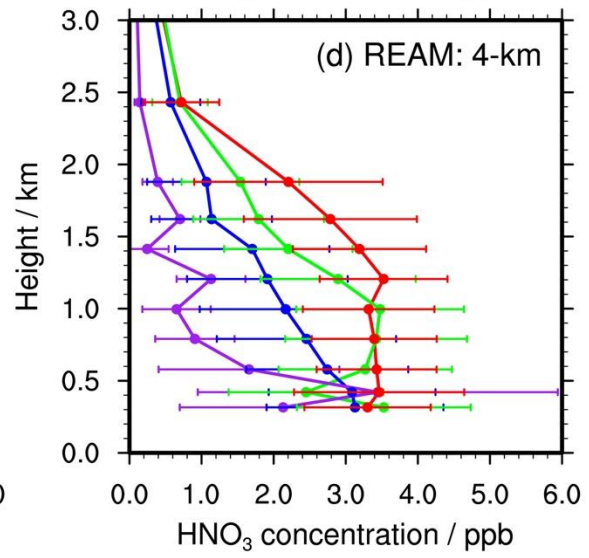
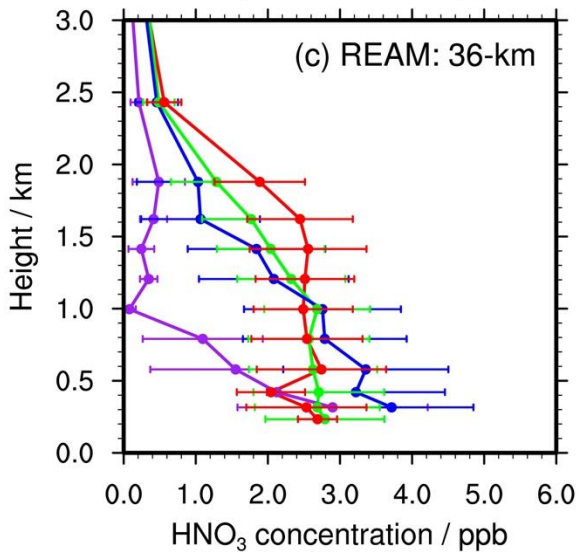
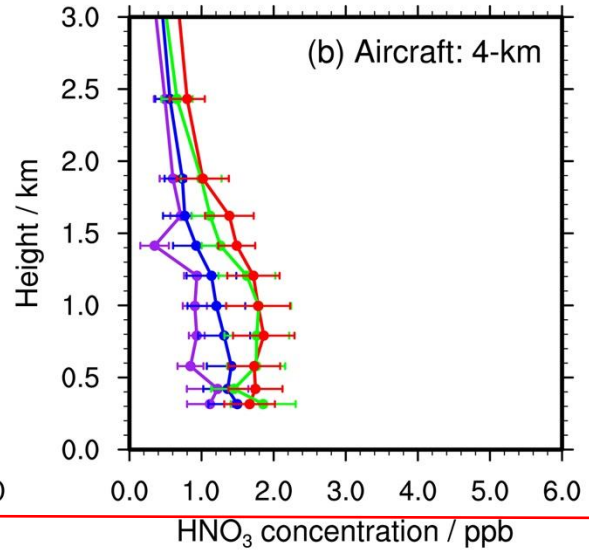
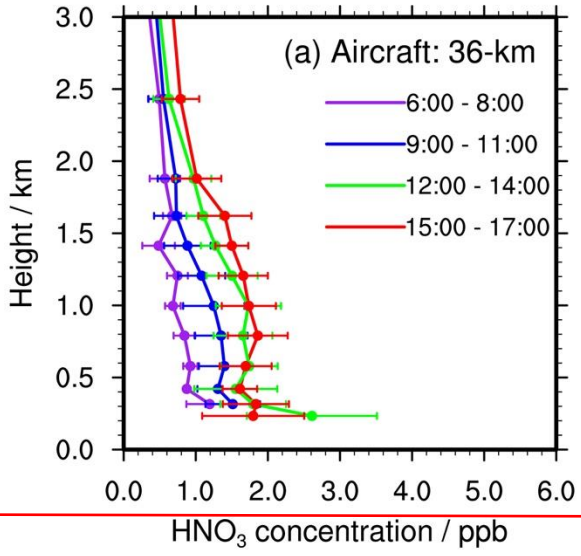
Figure S13. Schematic of remote and ground-based sensing of NO₂ VCDs. Green lines indicate the Pandora measurement rays, solid lines for the morning and dash lines for the afternoon. Red dots denote NO₂ molecules. Blue lines represent the reflected radiation rays received by the satellite. Orange circles denote the sun, and the purple line denote the PBL height.

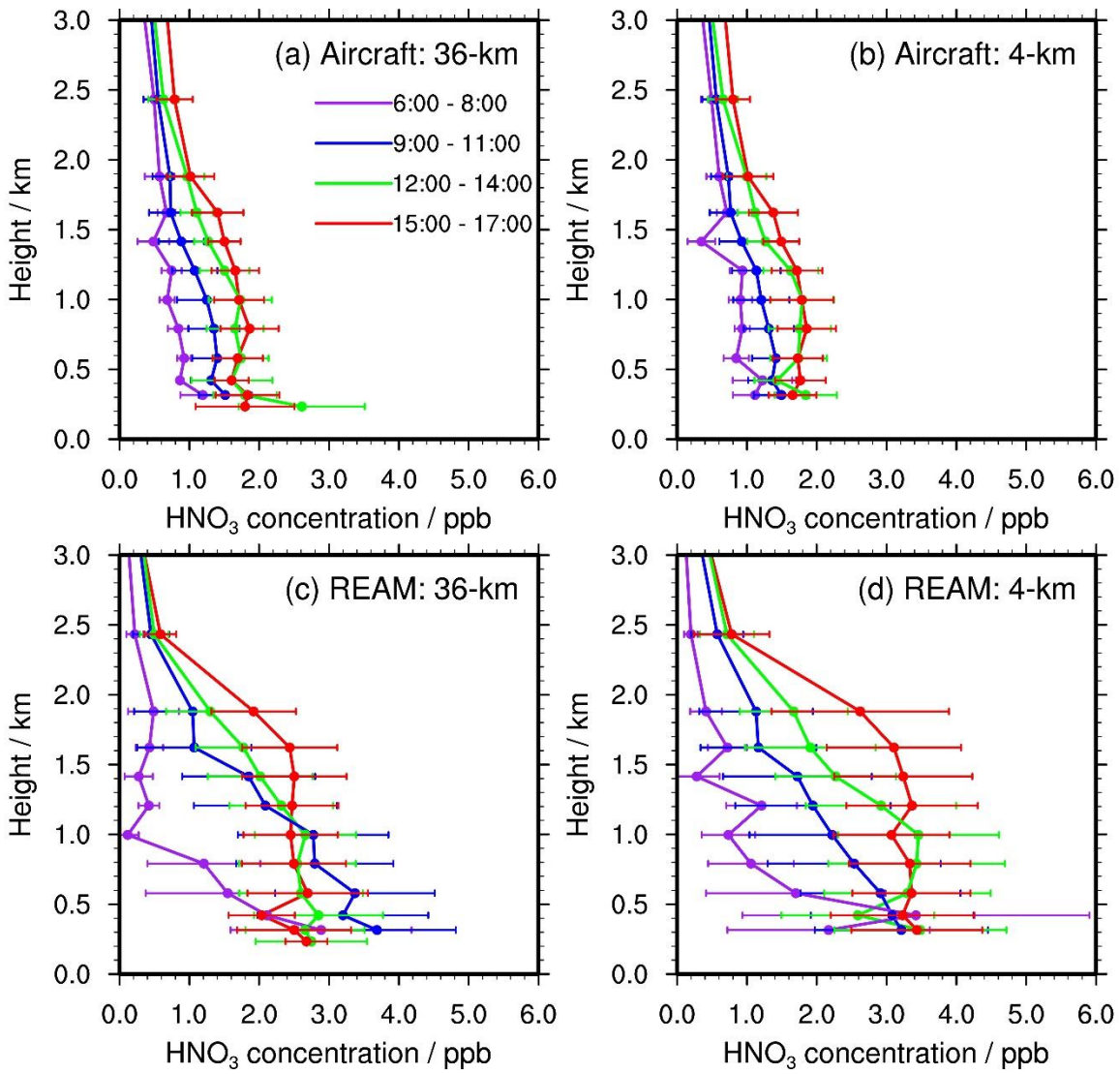




192

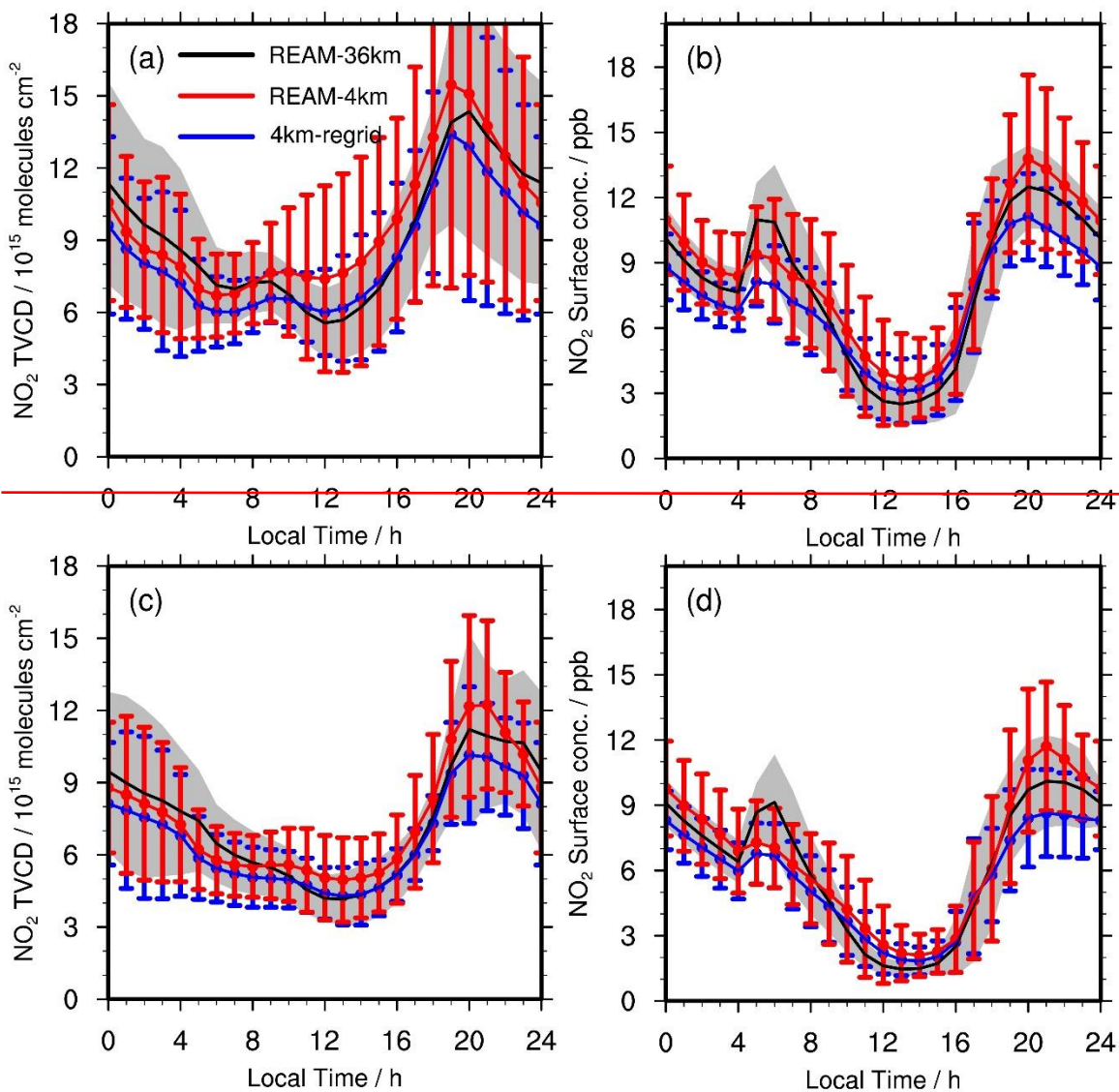
193 **Figure S145.** Temporal evolutions of derived- NO_y vertical profiles from the (a, b) P-3B aircraft
 194 and (c, d) REAM simulations at (a, c) 36-km and (b, d) 4-km resolutions during the DISCOVER-
 195 AQ campaign. Error bars denote the corresponding standard deviations. Due to the limited
 196 number of P-3B derived- NO_y observations and slightly different heights between 36- and 4-km
 197 grid cells from different WRF simulations (Table S2), small differences exist between the 36-km
 198 and 4-km observations when we bin them vertically to REAM grid cells (see also Table 1).
 199





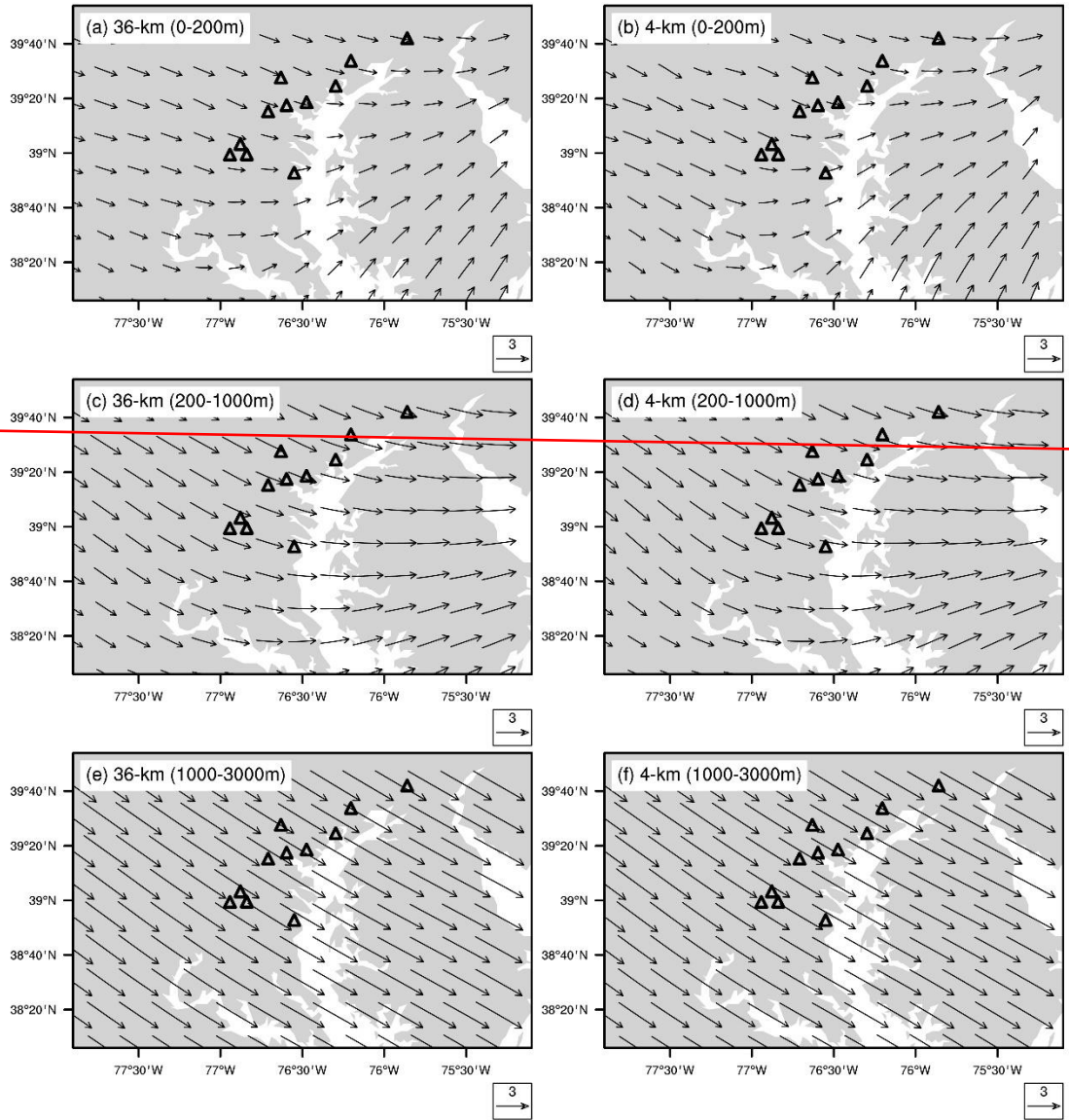
201
202
203

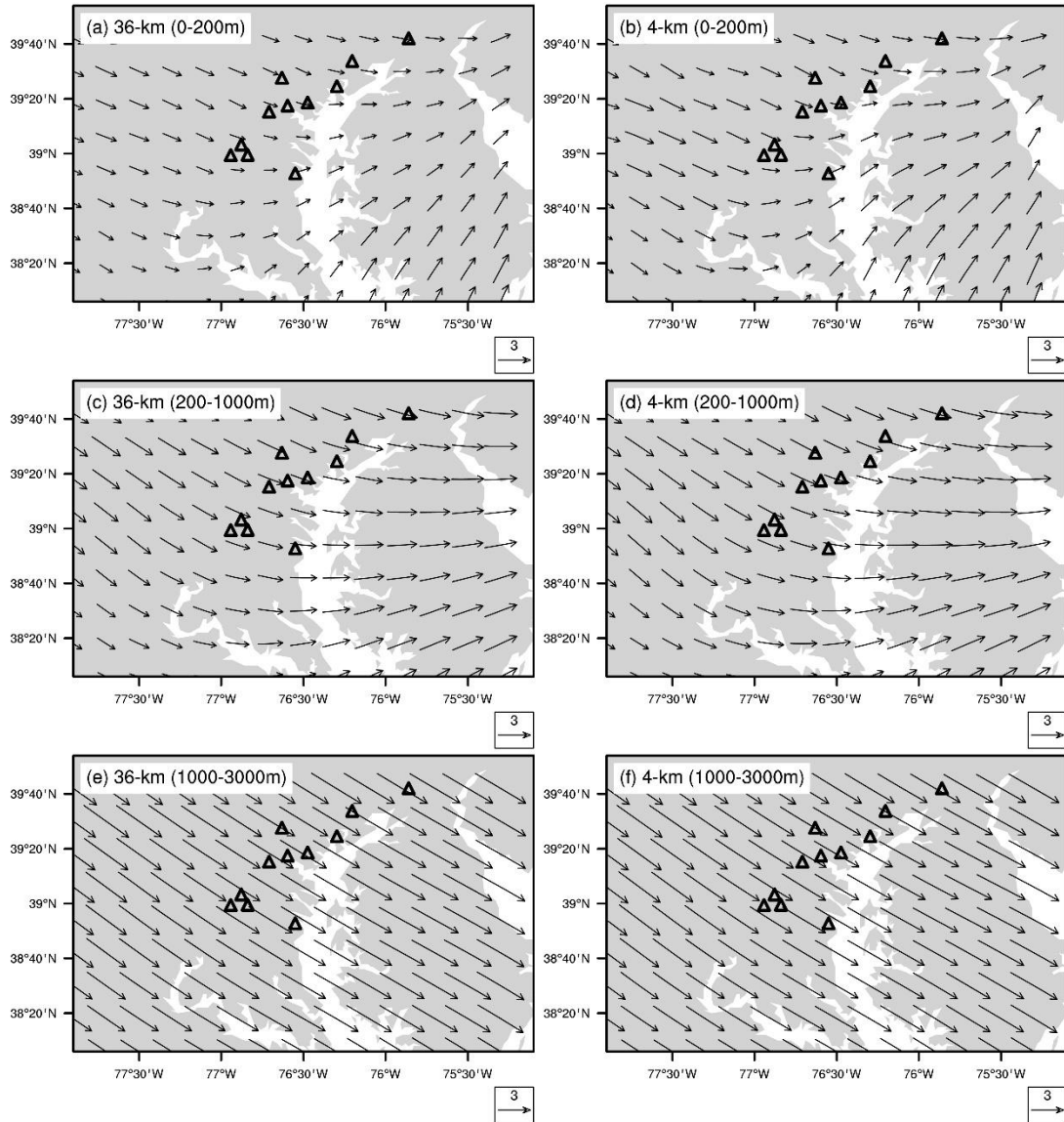
Figure S156. Same as Figure S145 but for coincident HNO_3 concentrations.



204
 205
 206
 207
 208
 209
 210
 211

Figure S17. Comparisons of NO_2 (a, c) TVCDs and (b, d) surface concentrations over the 11 inland Pandora sites between the 4 km and 36 km REAM simulations on (a, b) weekdays and (c, d) weekends for July 2011. “REAM 36km” (black lines) denotes the 36 km REAM simulation results; “REAM 4km” (red lines) denotes the 4 km REAM simulation results; “4km regrid” refers to the 36 km values by re-gridding the 4 km REAM simulation results into 36 km REAM grid-cells. Error bars denote standard deviations.

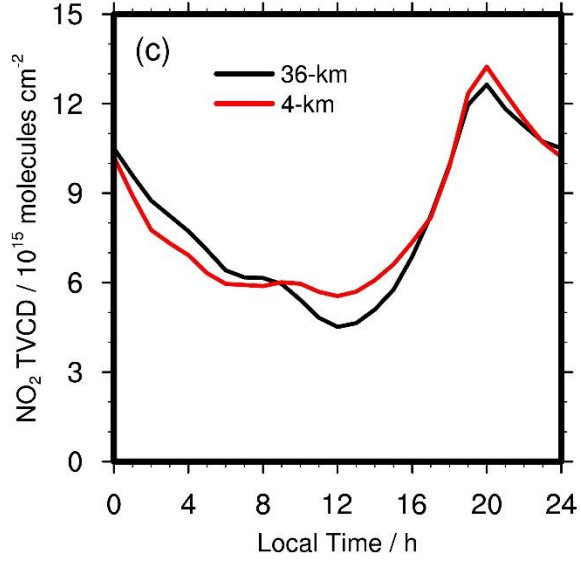
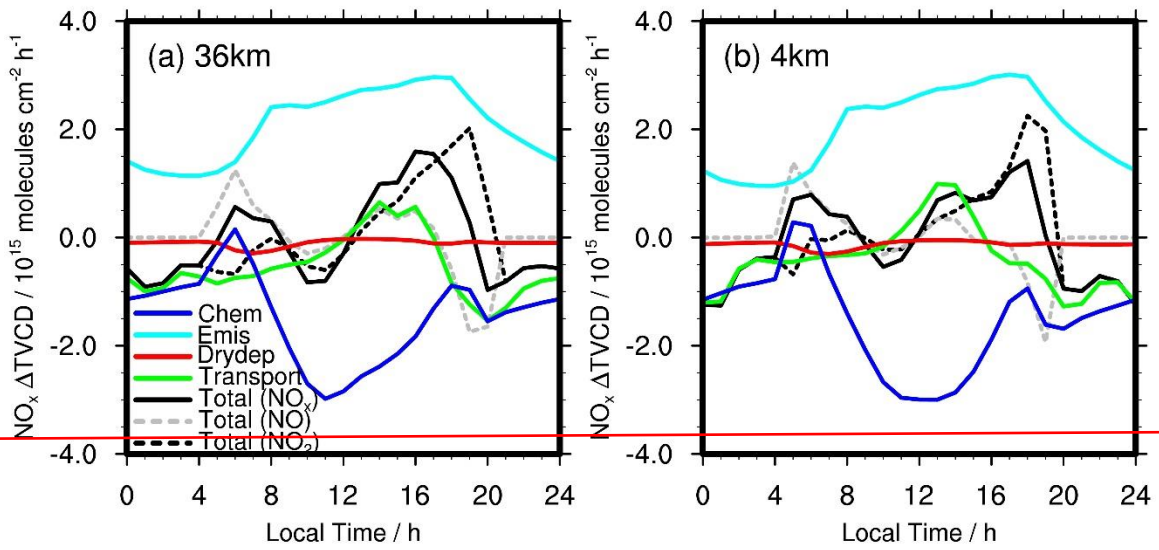


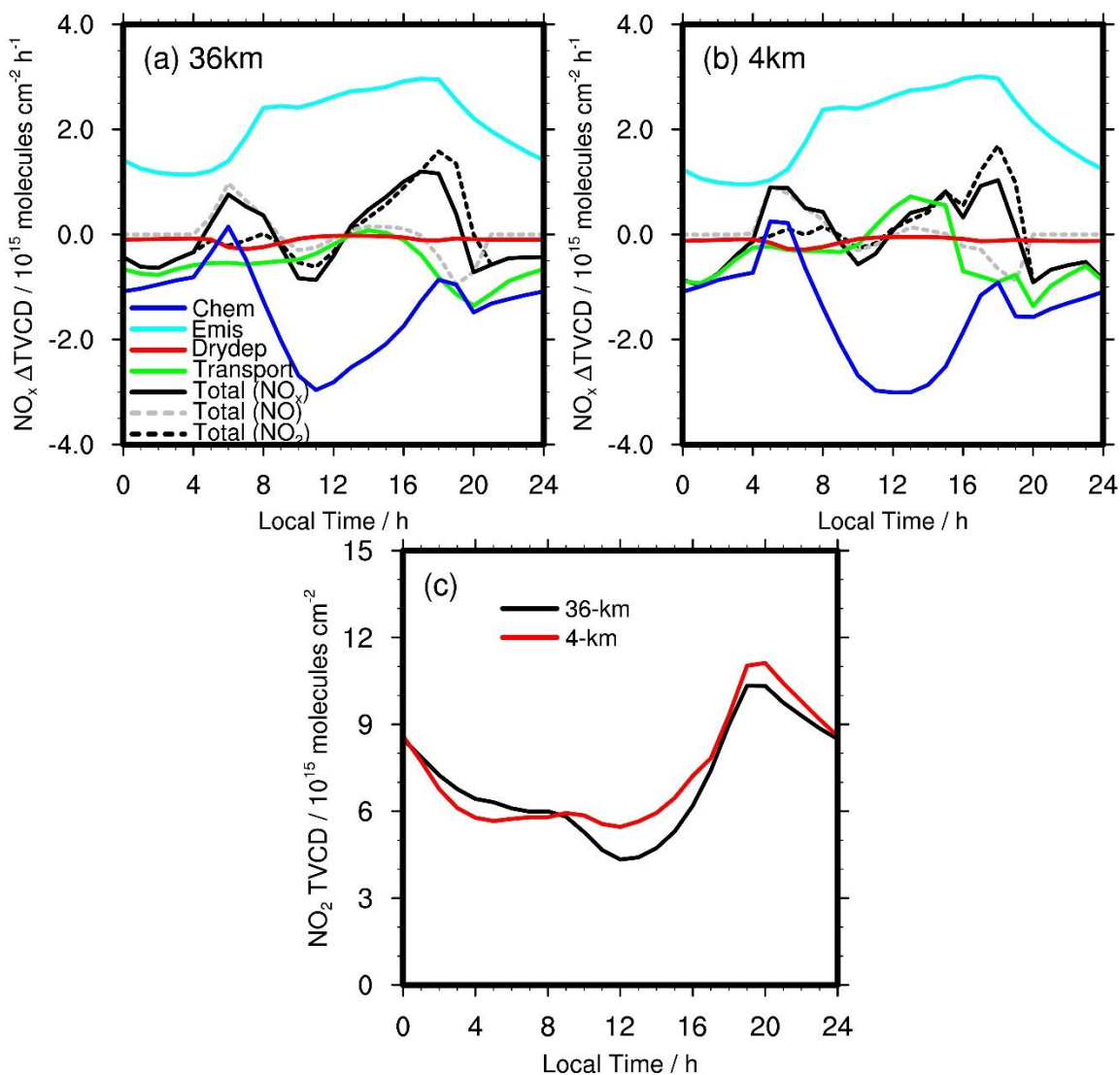


213

214 **Figure S168.** Comparisons of wind fields between the (a, c, e) 36-km and (b, d, f) nested 4-km
 215 WRF simulations for different height (AGL) bins in July 2011. (a) and (b) are for mean wind
 216 fields below about 200 m, (c) and (d) are for about 200 – 1000 m, and (e) and (f) are for about
 217 1000 – 3000 m. Triangles denote the inland Pandora sites in Figure S1. The unit of wind speed is
 218 m s^{-1} .

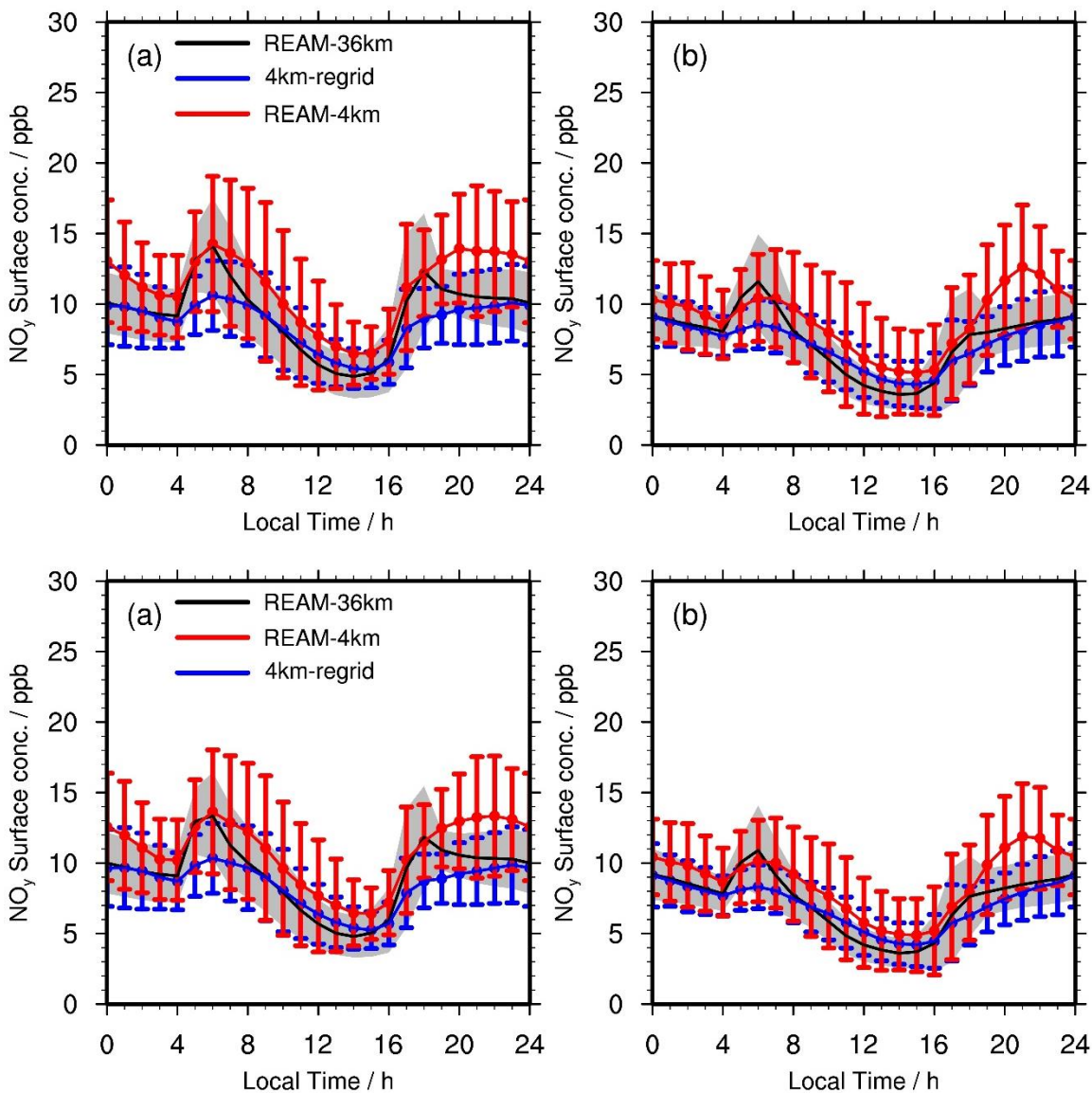
219





221

222 **Figure S179.** Contributions of emission, chemistry, transport, and dry deposition to NO_x TVCD
 223 diurnal variations over the six P-3B spiral sites (Figure S1 and Table S1) on weekdays in July
 224 2011 for the (a) 36-km and (b) 4-km REAM simulations. “Chem” refers to net NO_x chemistry
 225 production; “Emis” refers to NO_x emissions; “Drydep” denotes NO_x dry depositions; “Transport”
 226 includes advection, turbulent mixing, lightning NO_x production, and wet deposition. “Total
 227 (NO_x)” is the hourly change of NO_x TVCDs ($\Delta(TVCD) = TVCD_{t+1} - TVCD_t$). “Total (NO₂)” is
 228 the hourly change of NO₂ TVCDs, and “Total (NO)” is the hourly change of NO TVCDs. (c), the
 229 36-km and 4-km REAM simulated diurnal cycles of NO₂ TVCDs over the P-3B spiral sites on
 230 weekdays in July 2011. The black line in (c) denotes the 36-km REAM simulation results, and the
 231 red line denotes the 4-km REAM simulation results.
 232

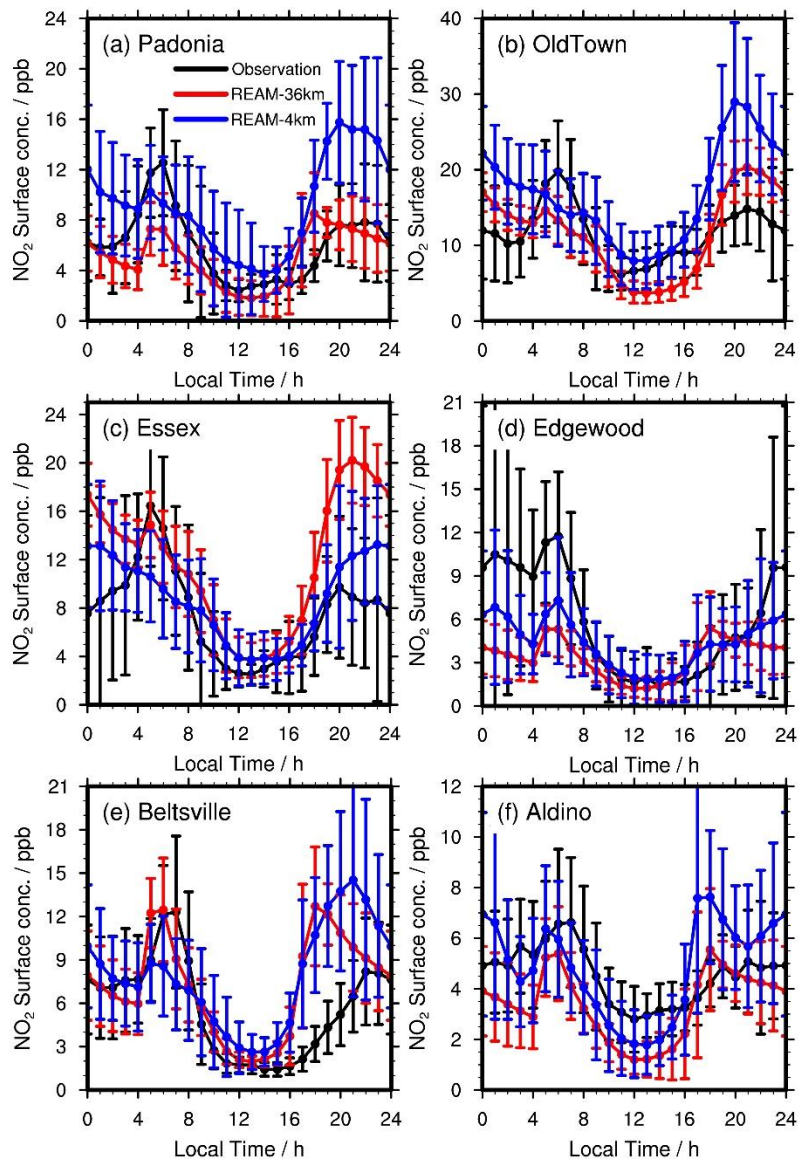


233

234

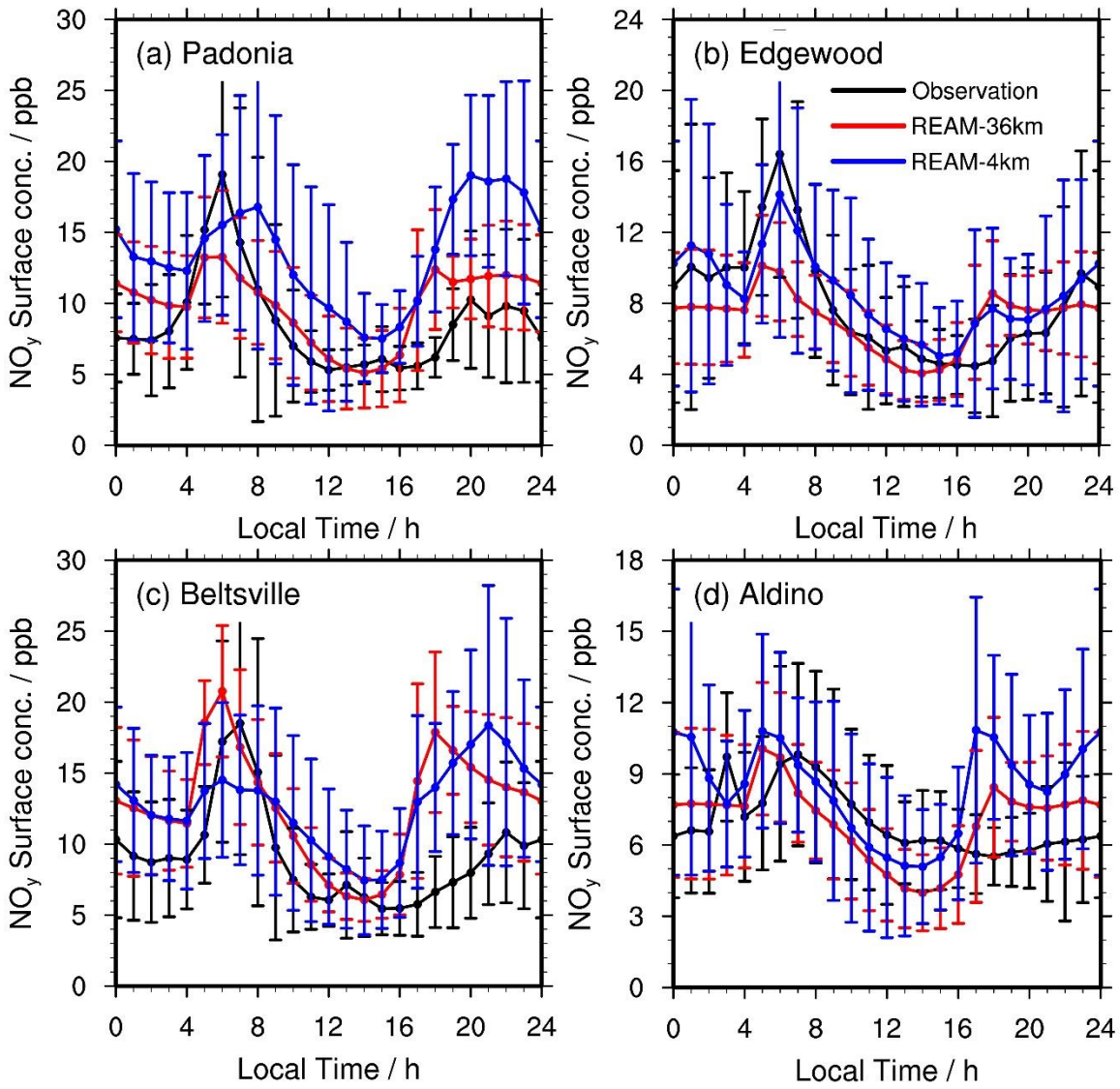
235 **Figure S1820.** Comparisons of mean surface NO_y concentrations at Padonia, Edgewood,
 236 Beltsville, and Aldino between the 4-km and 36-km REAM simulations on (a) weekdays and (b)
 237 weekends for July 2011. “REAM-36km” (black lines) denotes the 36-km REAM simulation
 238 results; “REAM-4km” (red lines) denotes the 4-km REAM simulation results; “4km-regrid”
 239 refers to the 36-km values by re-gridding 4-km REAM simulation results into 36-km REAM grid
 240 cells. Error bars denote standard deviations.

241



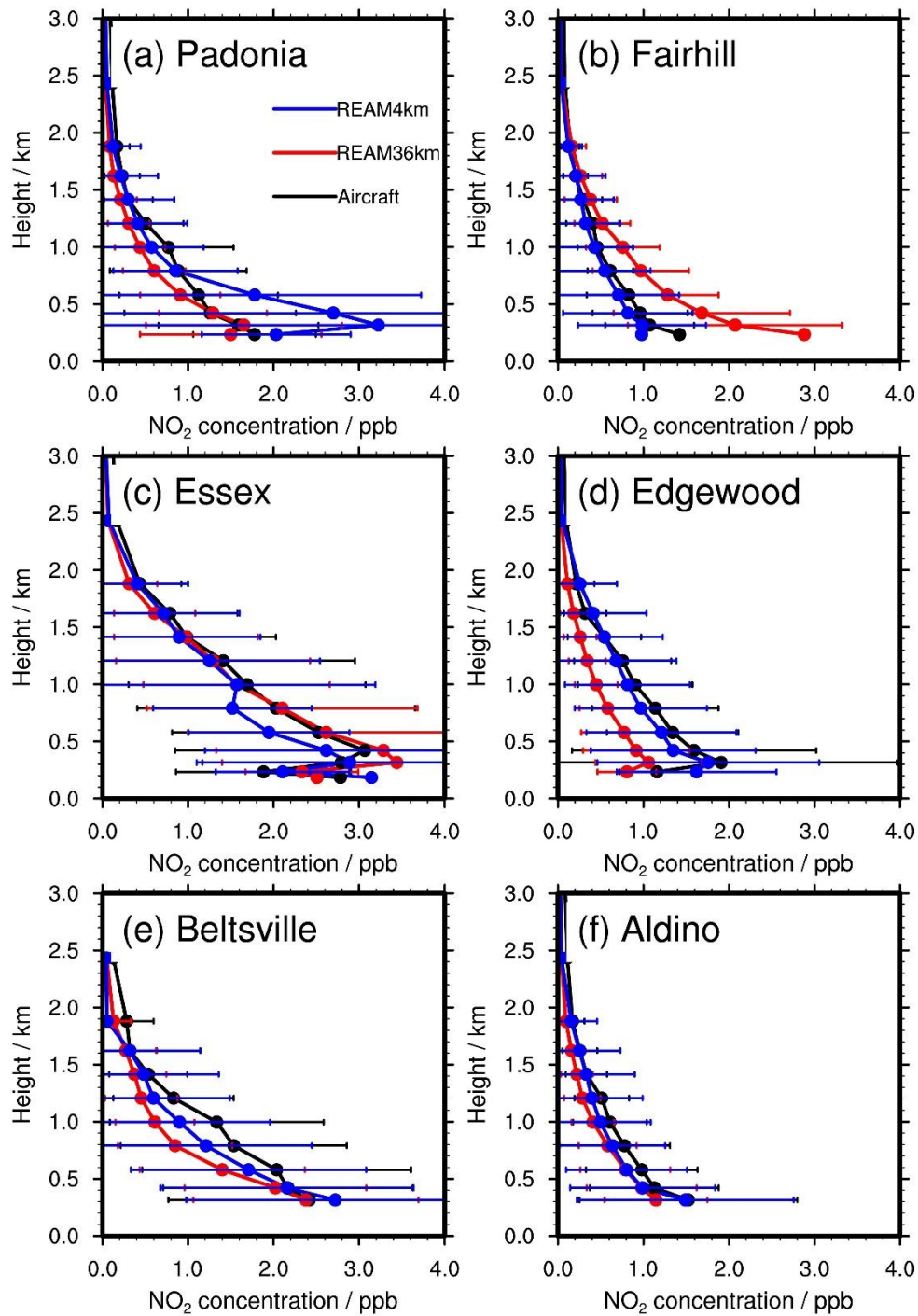
242
 243
 244

Figure S19. Same as Figure 7 but for individual observation sites on weekdays.



245
246
247

Figure S20. Same as Figure 12 but for individual observation sites on weekdays.



248
 249
 250
 251
 252
 253

Figure S21. Comparison of NO₂ vertical profiles among P-3B aircraft observations and the 36-km and 4-km REAM simulations on weekdays in July 2011 for different spiral sites. Here we calculate the average of all available weekday NO₂ vertical profiles for each spiral site but do not consider the temporal evolutions shown in Figure 8.

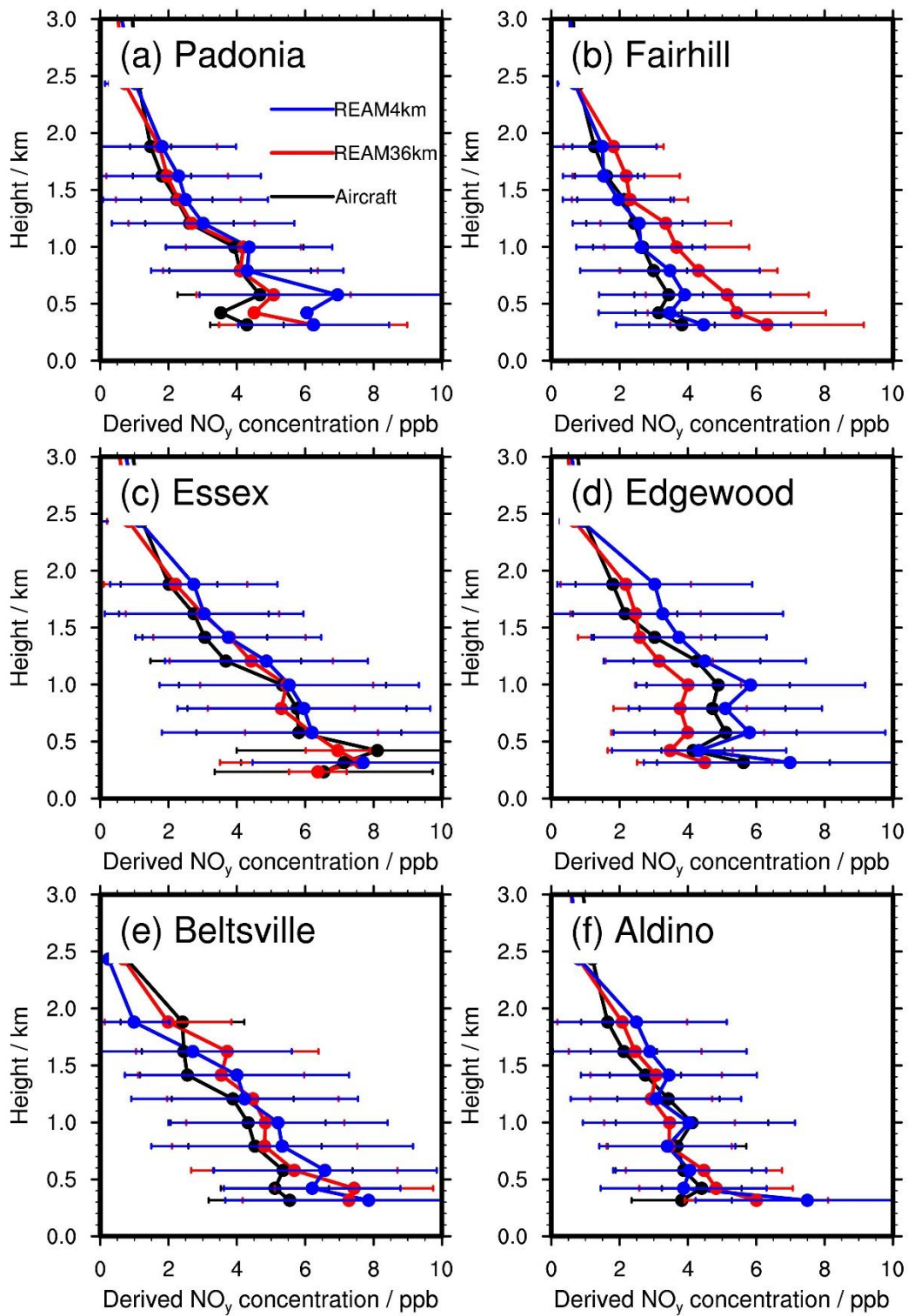
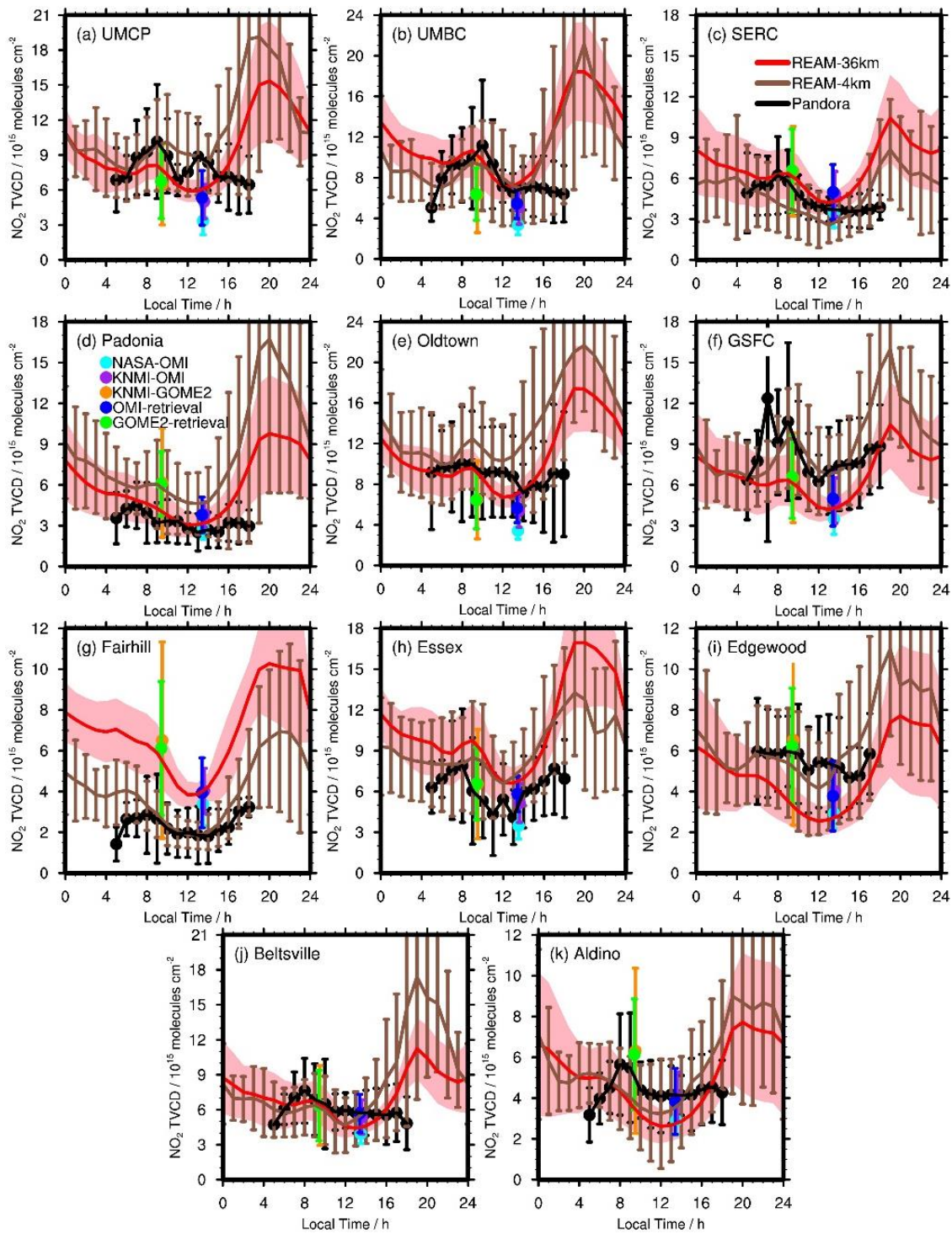


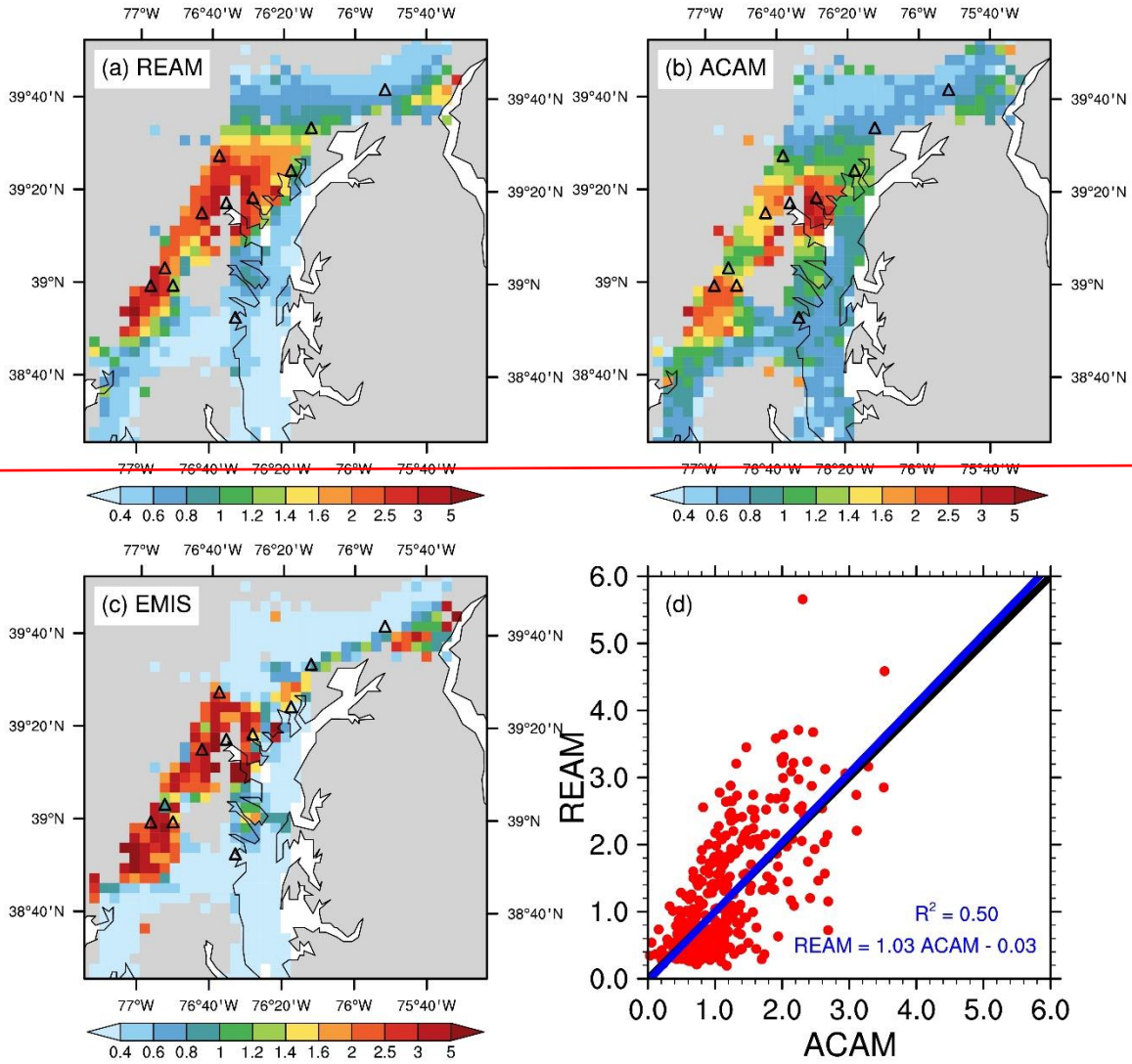
Figure S22. Same as Figure S21 but for derived- NO_y vertical profiles.

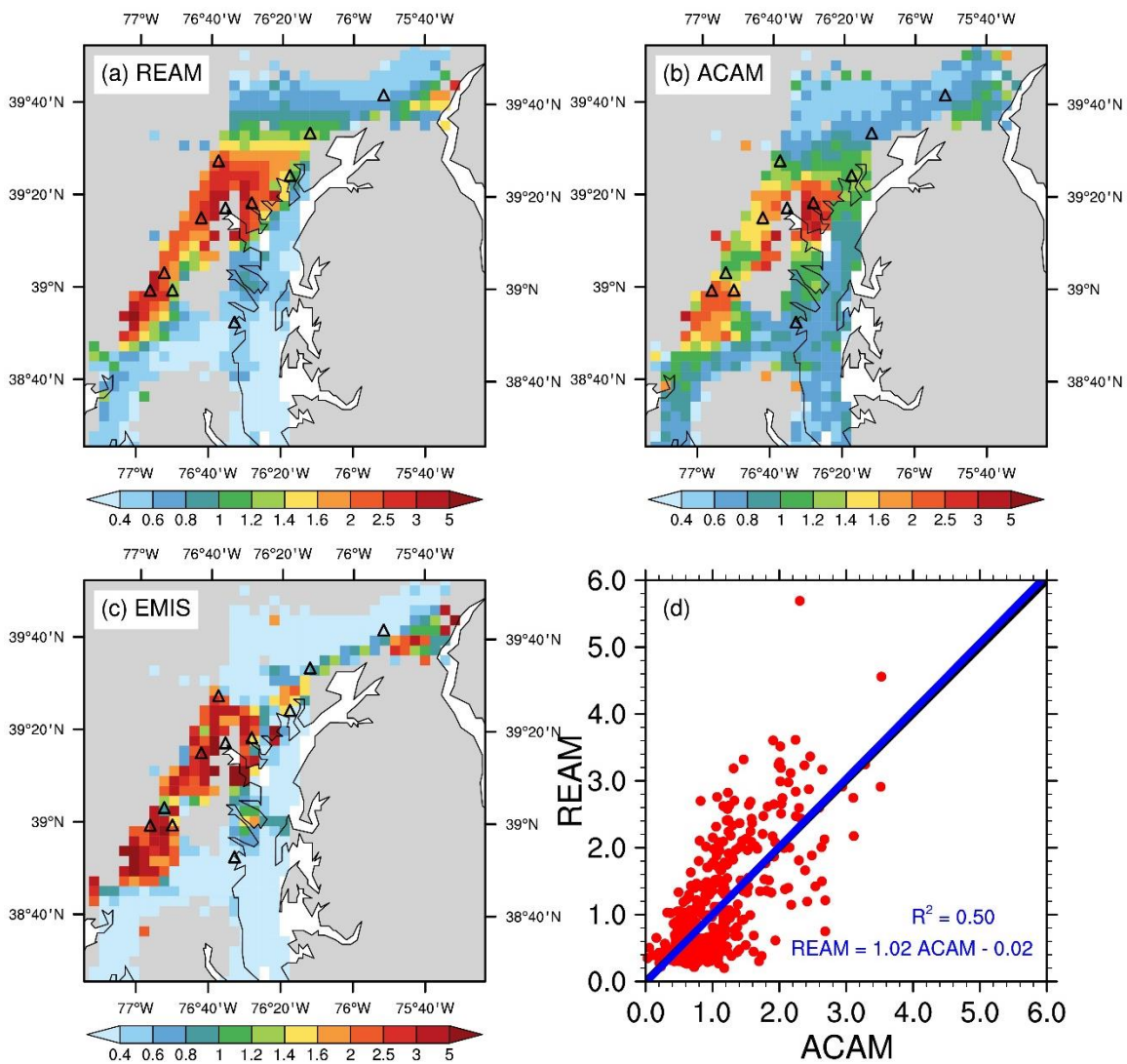
254
255
256



257
 258
 259
 260

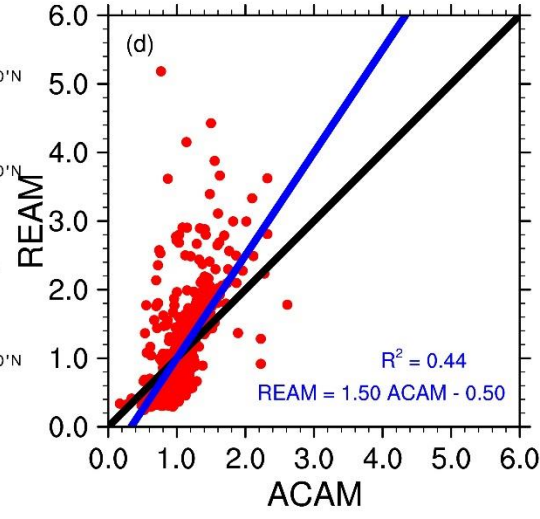
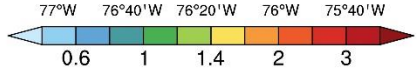
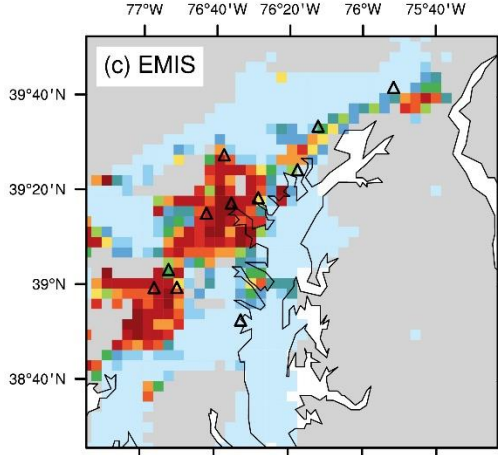
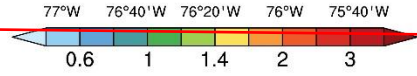
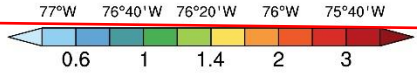
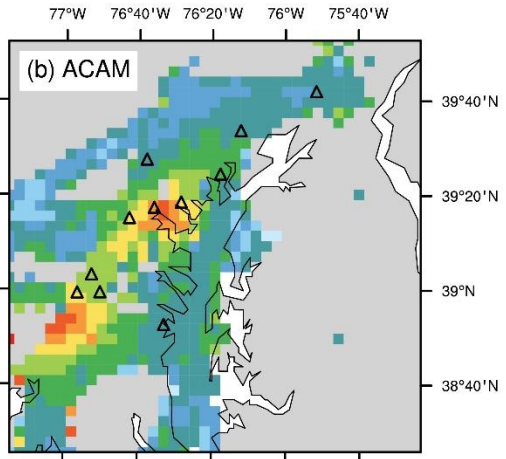
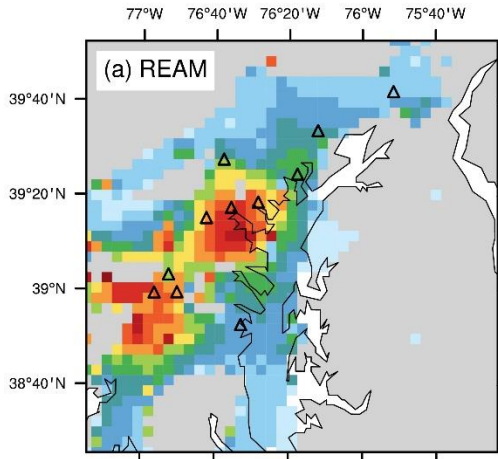
Figure S23. Same as Figure 10 but for individual Pandora sites on weekdays. Here we do not include P-3B aircraft-derived NO_2 VCDs below 3.63 km.

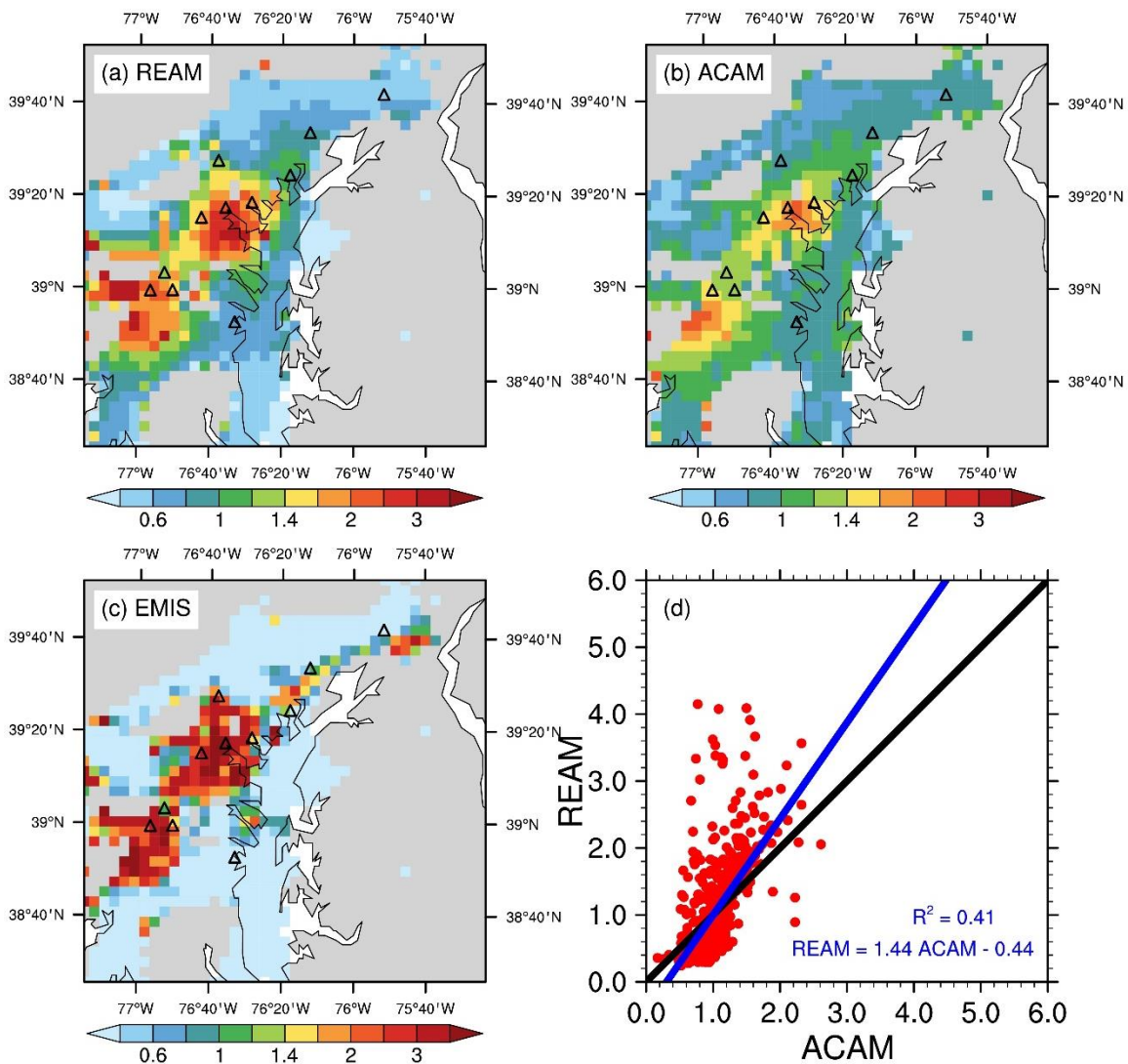




262
 263
 264
 265
 266

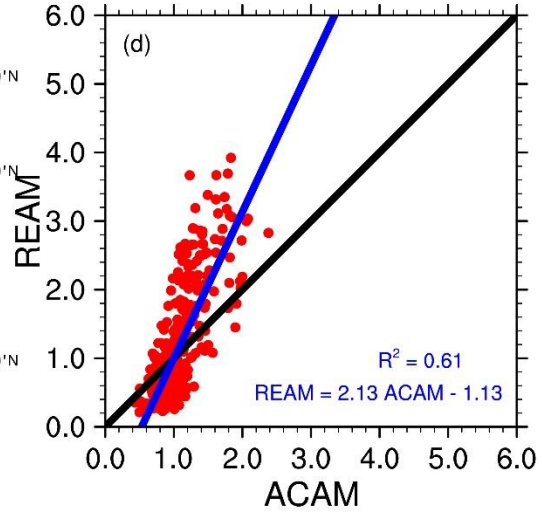
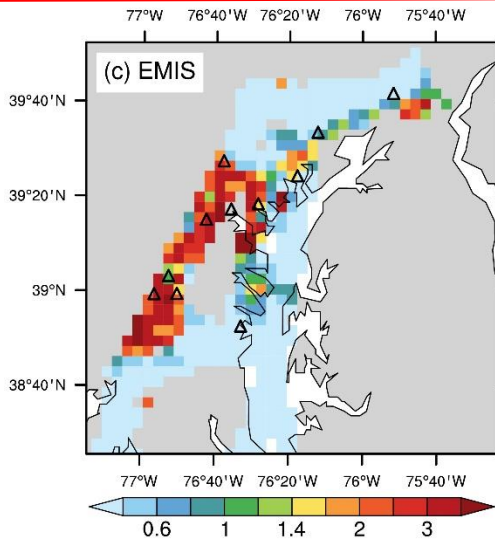
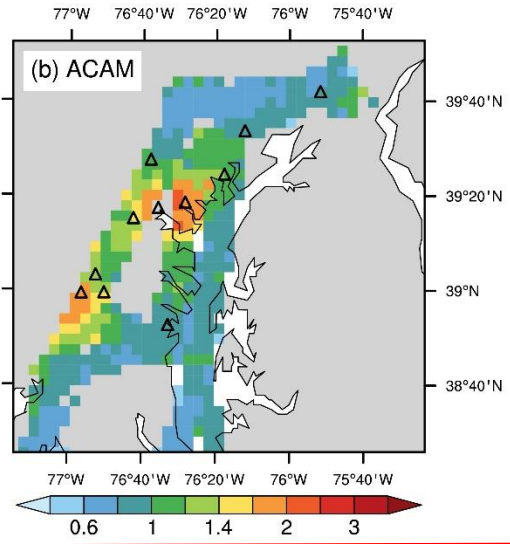
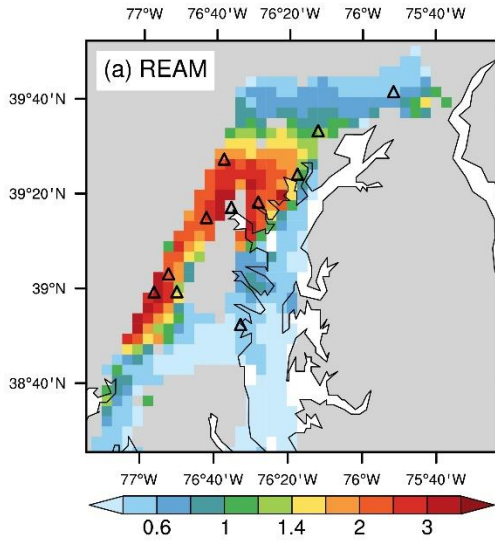
Figure S241. Same as Figure 140 but for weekends in July 2011. The domain averages of ACAM and coincident 4-km REAM NO₂ VCDs are 3.0 ± 1.7 and $3.3 \pm 2.78 \times 10^{15}$ molecules cm⁻², respectively.

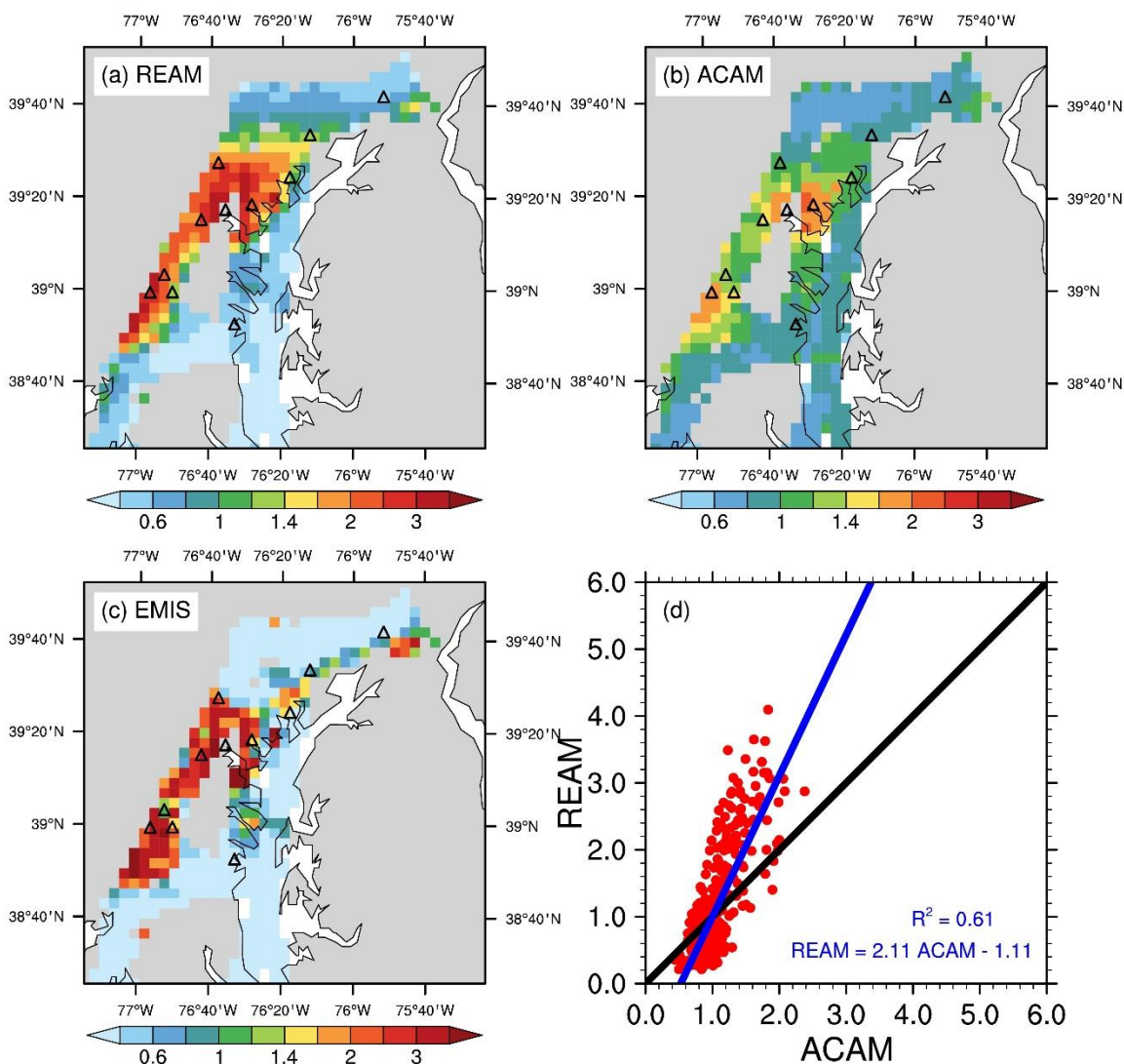




268

269 **Figure S252.** Same as Figure 10-14 but for weekday ACAM datasets obtained from [https://www-](https://www-air.larc.nasa.gov/cgi-bin/ArcView/discover-aq.dc-2011?UC12=1#LIU.XIONG/)
 270 [air.larc.nasa.gov/cgi-bin/ArcView/discover-aq.dc-2011?UC12=1#LIU.XIONG/](https://www-air.larc.nasa.gov/cgi-bin/ArcView/discover-aq.dc-2011?UC12=1#LIU.XIONG/) (last access:
 271 [December 31, 2019](https://www-air.larc.nasa.gov/cgi-bin/ArcView/discover-aq.dc-2011?UC12=1#LIU.XIONG/)). The domain averages of ACAM and coincident 4-km REAM NO₂ VCDs
 272 are 5.9 ± 1.8 and $4.65 \pm 3.1 \times 10^{15}$ molecules cm⁻², respectively.
 273





275

276

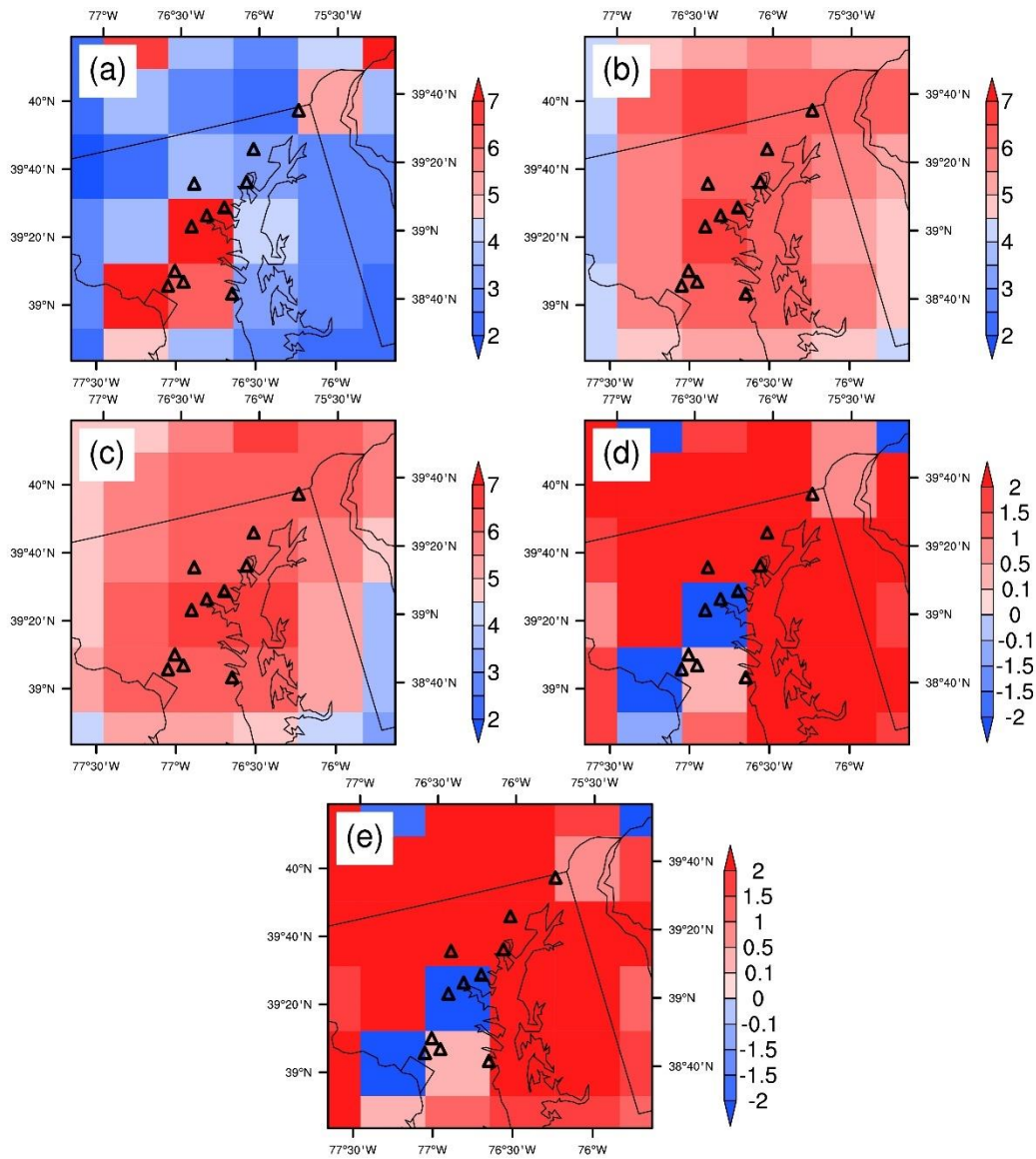
277

278

279

280

Figure S263. Same as Figure S252 but for weekend ACAM datasets obtained from <https://www-air.larc.nasa.gov/cgi-bin/ArcView/discover-aq.dc-2011?UC12=1#LIU.XIONG/> (last access: December 31, 2019). The domain averages of ACAM and coincident 4-km REAM NO₂ VCDs are 4.7 ± 1.4 and $3.4 \pm 2.7 \times 10^{15}$ molecules cm⁻², respectively.



281

282 **Figure S27.** Distributions of weekday NO₂ TVCDs around the DISCOVER-AQ 2011 region for
 283 9:30 LT in July 2011: (a) the 36-km REAM simulation results, (b) the KNMI GOME-2A product,
 284 (c) for the retrieved GOME-2A NO₂ TVCDs by using the KNMI DOMINO algorithm with
 285 corresponding 36-km REAM vertical profiles, (d) distribution of the NO₂ TVCD differences (b
 286 minus a) between KNMI GOME-2A and 36-km REAM, and (e) the difference (c minus a)
 287 between retrieved GOME-2A NO₂ TVCDs and the 36-km REAM results. The NO₂ TVCD unit is
 288 10^{15} molecules cm^{-2} .

289

1 Supporting tables for

2 **Comprehensive evaluations of diurnal NO₂ measurements during**
3 **DISCOVER-AQ 2011: Effects of resolution dependent representation of NO_x**
4 **emissions**

5 Jianfeng Li^{1, a}, Yuhang Wang^{1*}, Ruixiong Zhang¹, Charles Smeltzer¹, Andrew Weinheimer², Jay
6 Herman³, K. Folkert Boersma^{4, 5}, Edward A. Celarier^{6, 7, b}, Russell W. Long⁸, James J. Szykman⁸,
7 Ruben Delgado³, Anne M. Thompson⁶, Travis N. Knepp^{9, 10}, Lok N Lamsal⁶, Scott J Janz⁶,
8 Matthew G Kowalewski⁶, Xiong Liu¹¹, Caroline R. Nowlan¹¹

9 ¹School of Earth and Atmospheric Sciences, Georgia Institute of Technology, Atlanta, Georgia,
10 USA

11 ²National Center for Atmospheric Research, Boulder, Colorado, USA

12 ³University of Maryland Baltimore County JCET, Baltimore, Maryland, USA

13 ⁴Royal Netherlands Meteorological Institute, De Bilt, the Netherlands

14 ⁵Wageningen University, Meteorology and Air Quality Group, Wageningen, the Netherlands

15 ⁶NASA Goddard Space Flight Center, Greenbelt, Maryland, USA

16 ⁷Universities Space Research Association, Columbia, Maryland, USA

17 ⁸National Exposure Research Laboratory, Office of Research and Development, U.S.

18 Environmental Protection Agency, Research Triangle Park, NC, USA

19 ⁹NASA Langley Research Center, Virginia, USA

20 ¹⁰Science Systems and Applications, Inc., Hampton, Virginia, USA

21 ¹¹Harvard-Smithsonian Center for Astrophysics, Cambridge, Massachusetts, USA

22
23 ^anow at: Atmospheric Sciences and Global Change Division, Pacific Northwest National
24 Laboratory, Richland, Washington, USA

25 ^bnow at: Digital Spec, Tyson's Corner, VA, USA

26 * *Correspondence to* Yuhang Wang (yuhang.wang@eas.gatech.edu)

27

28 **Table S1.** Summary of information for the 11 inland Pandora sites in the DISCOVER-AQ campaign

Site #	Site name	Latitude / ° N	Longitude / ° W	Land type	NO _x emission in 36-km REAM ¹ / 10 ²¹ molecules km ⁻² s ⁻¹	NO _x emission in 4-km REAM / 10 ²¹ molecules km ⁻² s ⁻¹	Availability of P-3B aircraft observations ²	Availability of surface NO _y	Availability of surface NO ₂
1	UMCP	38.991	76.943	urban	10.9	19.5			
2	UMBC	39.255	76.709	urban	12.9	14.8			
3	SERC	38.880	76.550	rural/coastal	5.0	0.8			
4	Padonia	39.461	76.631	suburban	2.9	12.8	Y	Y	Y
5	Oldtown	39.291	76.596	urban	12.9	33.0			Y
6	GSFC	38.993	76.840	urban/suburban	5.0	6.2			
7	Fairhill	39.701	75.860	rural	6.6	0.6	Y		
8	Essex	39.311	76.474	coastal/urban	12.9	6.4	Y		Y
9	Edgewood	39.410	76.297	coastal/urban	1.7	1.3	Y	Y	Y
10	Beltsville	39.055	76.878	suburban	5.0	4.4	Y	Y	Y
11	Aldino	39.563	76.204	rural/suburban	1.7	4.2	Y	Y	Y

29 ¹ Here, NO_x emissions refer to the mean values in one week (Monday – Sunday). Since we scale weekend emissions based on weekday emissions in this study,
 30 the relative differences among different sites and between the 36-km REAM and the 4-km REAM are the same for weekdays and weekends.

31 ² “Y” denotes that P-3B aircraft observations were available at the corresponding site during the DISCOVER-AQ campaign. And blank indicates that no aircraft
 32 observations were available. Similar to the “availability of surface NO_y” and the “availability of surface NO₂.”

34 **Table S2.** Setup of the 36-km and nested 4-km WRF simulations

	36-km WRF	Nested 4-km WRF
Horizontal resolution	36 km	Nested (36 km, 12 km, 4 km)
Domain center	40° N, 97° W	38.94° N, 75.76° W
Microphysics	WRF Single-Moment 63 -class simple ice scheme (<u>WSM6</u>)	Same as 36-km WRF
Surface layer	Revised MM5 Monin-Obukhov scheme	Same as 36-km WRF
Land surface	Unified Noah land-surface model	Same as 36-km WRF
Longwave radiation	RRTM scheme	Same as 36-km WRF
Shortwave radiation	Dudhia scheme	Same as 36-km WRF
Planetary boundary layer	Yonsei University (YSU) scheme	Same as 36-km WRF
Cumulus parameterization	Kain-Fritsch (new Eta) scheme	Kain-Fritsch scheme for outer domains (36-km and 12-km); no cumulus parameterization for the 4-km domain
Urban surface	3-category urban canopy model	Same as 36-km WRF

35

36 **Table S3.** Comparison of NO₂ TVCDs among different simulations and datasets during the DISCOVER-AQ campaign for 9:30 and 13:30 LT on
 37 weekdays and weekends

	<u>Weekday</u>		<u>Weekend</u>	
	<u>9:30 LT¹</u>	<u>13:30 LT</u>	<u>9:30 LT</u>	<u>13:30 LT</u>
<u>REAM-36km²</u>	<u>6.5 ± 1.1³</u>	<u>4.9 ± 0.6</u>	<u>4.7 ± 0.7</u>	<u>3.6 ± 0.6</u>
<u>REAM-4km</u>	<u>7.0 ± 1.9</u>	<u>6.3 ± 2.0</u>	<u>5.3 ± 1.6</u>	<u>4.3 ± 1.5</u>
<u>Pandora</u>	<u>6.5±1.8</u>	<u>5.3±1.0</u>	<u>4.9±0.9</u>	<u>3.7±0.5</u>
<u>Flight</u>	<u>5.3</u>	<u>5.0</u>	<u>4.5</u>	<u>3.2</u>
<u>KNMI-GOME2</u>	<u>6.3 ± 3.4</u>		<u>5.3 ± 1.4</u>	
<u>GOME2-retrieval</u>	<u>6.3 ± 2.5</u>		<u>4.1 ± 1.9</u>	
<u>NASA-OMI</u>		<u>3.3 ± 0.8</u>		<u>2.9 ± 0.6</u>
<u>KNMI-OMI</u>		<u>4.6 ± 1.3</u>		<u>3.2 ± 0.7</u>
<u>OMI-retrieval</u>		<u>4.7 ± 1.4</u>		<u>3.2 ± 0.7</u>

38 ¹ For REAM simulations, we use the average of NO₂ TVCDs at 9:00 and 10:00 LT to represent the value at 9:30 LT, similar to those at 13:30 LT.

39 ² The dataset names have the same meaning as Figure 10, and the NO₂ TVCD values are the same as those shown in Figure 10.

40 ³ The unit is 10¹⁵ molecules cm⁻².